Comas, M.C., Zahn, R., Klaus, A., et al., 1996
Proceedings of the Ocean Drilling Program, Initial Reports, Vol. 161

4. SITE 974[1]

Shipboard Scientific Party[2]

HOLE 974A

Date occupied: 0345, 7 May 1995

Date departed: 1700, 7 May 1995

Time on hole: 13 hr, 15 min

Position: 40°21.364′N, 12°8.506′E

Drill pipe measurement from rig floor to seafloor (m): 3469.7

Distance between rig floor and sea level (m): 10.86

Water depth (drill pipe measurement from sea level, m): 3458.8

Total depth (from rig floor, m): 3479.2

Penetration (m): 9.5

Number of cores (including cores having no recovery): 1

Total length of cored section (m): 9.5

Total core recovered (m): 9.81

Core recovery (%): 103.0

Oldest sediment cored:
Depth (mbsf): 9.5
Nature: Silty clay
Age: Pleistocene

Comments: Overshot the mudline. Believed that 0–5 mbsf not recovered.

HOLE 974B

Date occupied: 1700, 7 May 1995

Date departed: 2345, 8 May 1995

Time on hole: 1 day, 6 hr, 45 min

Position: 40°21.362′N, 12°8.516′E

Drill pipe measurement from rig floor to seafloor (m): 3464.7

Distance between rig floor and sea level (m): 10.86

Water depth (drill pipe measurement from sea level, m): 3453.9

Total depth (from rig floor, m): 3668.4

Penetration (m): 203.7

Number of cores (including cores having no recovery): 22

Total length of cored section (m): 203.7

Total core recovered (m): 208.23

Core recovery (%): 102.2

Oldest sediment cored:
Depth (mbsf): 203.7
Nature: Sand
Age: Miocene

[1]Comas, M.C., Zahn, R., Klaus, A., et al., 1996. *Proc. ODP, Init. Repts.,* 161: College Station, TX (Ocean Drilling Program).
[2]Shipboard Scientific Party is given in the list preceding the Table of Contents.

HOLE 974C

Date occupied: 2345, 8 May 1995

Date departed: 2100, 10 May 1995

Time on hole: 1 day, 21 hr, 15 min

Position: 40°21.348′N, 12°8.534′E

Drill pipe measurement from rig floor to seafloor (m): 3464.1

Distance between rig floor and sea level (m): 10.86

Water depth (drill pipe measurement from sea level, m): 3453.3

Total depth (from rig floor, m): 3668.6

Penetration (m): 204.5

Number of cores (including cores having no recovery): 22

Total length of cored section (m): 204.5

Total core recovered (m): 199.85

Core recovery (%): 97.7

Oldest sediment cored:
Depth (mbsf): 204.5
Nature: Sand
Age: Miocene

HOLE 974D

Date occupied: 2100, 10 May 1995

Date departed: 1730, 11 May 1995

Time on hole: 20 hr, 30 min

Position: 40°21.357′N, 12°8.520′E

Bottom felt (drill pipe measurement from rig floor, m): 3464.9

Distance between rig floor and sea level (m): 10.89

Water depth (drill pipe measurement from sea level, m): 3454.0

Total depth (from rig floor, m): 3627.9

Penetration (m): 163.0

Number of cores (including cores having no recovery): 18

Total length of cored section (m): 163.0

Total core recovered (m): 170.49

Core recovery (%): 104.6

Oldest sediment cored:
Depth (mbsf): 163.0
Nature: Clay
Age: early Pliocene

Principal results: Site 974 (proposed site MedSap-5) is located in the central Tyrrhenian Sea, on the lowermost eastern continental margin of Sardinia. The site lies in a north-south–trending small deep basin, between the Tyrrhenian Central Fault and the De Marchi Seamount. The objectives of Site 974 were (1) to obtain a complete Pleistocene to Pliocene sedimentary sequence that would contain a continuous record of organic-rich depositional events (sapropel intervals) in the Tyrrhenian Sea, and (2) to retrieve a comprehensive record of the coeval volcaniclastic deposits within this sequence. Site 974 recovered 203.7 m (Hole 974B), 199.9 m (Hole 974C), and 170.5 m (Hole D) of Pleistocene–Pliocene sediments. At the base of the sedimentary sequence in Hole 974B (203.7 mbsf) and Hole 974C (204.5 mbsf) latest Miocene sediments were reached. A complete recovery of the sedimentary sequence was achieved at Site 974 by triple APC coring down to 165 mbsf, followed by double XCB coring to total depth.

Pleistocene to Pliocene sediments at Site 974 contain a continuous record of organic-rich depositional events (sapropel intervals) and volcaniclastic deposits. Sedimentation rates range from 27.2 m/m.y. (late Pliocene) to 55.1 m/m.y. (Pleistocene–Holocene) as calculated from biostratigraphic data. High-resolution profiles of GRAPE density, magnetic susceptibility, and color reflectance were used to construct a continuous composite depth section from Holes 974B, 974C, and 974D by aligning distinctive features in each of the cores.

The sediment column is subdivided into four lithostratigraphic units based primarily on nannofossil (carbonate) content.

Unit I (Hole 974B, 0–88.9 mbsf; Hole 974C, 0–90.1 mbsf; Hole 974D, 0–89.8 mbsf) consists of Pliocene to Pleistocene nannofossil-rich clay to nannofossil-rich silty clay. Carbonate content within this unit averages 29% by weight. A total of 36 sapropels between 2 and 20 cm thick have been identified within Unit I. Total organic carbon (TOC) content of the sapropels reaches up to 6.4%. Organic matter in the sapropels mostly consists of partially degraded marine algal and microbial material as indicated by atomic C/N ratios and Rock-Eval analyses. Numerous ash and volcaniclastic layers exist in Unit I ranging from a few millimeters to about 12 cm in thickness.

Unit II (Hole 974B, 88.9–199.32 mbsf; Hole 974C, 90.1–200.14 mbsf; Hole 974D, 89.8–163 mbsf) consists of Pliocene nannofossil clay and nannofossil ooze with minor amounts (1%–5%) of foraminifers. The carbonate content averages 50%. Few ash beds are present, and a few sapropels are present in the lower part of Unit II.

The sediments of Units I and II correspond to deposits that accumulated in an open marine environment with a periodic influx of pyroclastic material. The shift from more pelagic deposits in Unit II to more hemipelagic sediments in Unit I may reflect greater terrigenous input during the Pleistocene. Lithostratigraphic Units I and II are also identified in the downhole logs (quad combo, Formation MicroScanner, geochemical tool). The heterogeneous log response in Unit I is likely caused by the more frequent occurrence of sapropels, ash beds, and the inferred greater terrigenous input.

Unit III (Hole 974B, 199.32–200.47 mbsf; Hole 974C, 200.14–200.97 mbsf) is a very thin, variegated unit that separates Pliocene marine sediments from the Messinian sequence with horizontally laminated to apparently cross-laminated interbeds.

Unit IV (Hole 974B, 200.47–203.86 mbsf; Hole 974C, 200.97–202.48 mbsf) consists of a single graded siliciclastic interval comprising a basal coarse-to-medium sand that grades upward into cross-laminated very fine sand, to cross- or parallel-laminated silt.

Bedding dips of up to approximately 15° in coherent sections are interpreted to reflect tectonic tilting of the sedimentary sequence. Microfaults with normal-sense displacements of 1 cm or less are abundant from about 30 mbsf downward, with dips mainly in the range of 45°–60°. Between 90 and 110 mbsf are intervals of slump folding on scales from 5 cm to 2 m, and disrupted and contorted bedding is observed. Slumping and tectonic deformation at this site suggest that the area was tectonically active during the Pliocene and Pleistocene.

Natural remanent magnetization (NRM) was strong in all cores. Inclinations throughout are close to present-day values at the site (+60°). The consistently positive inclinations appear to be caused by drill-string overprinting, which makes magnetostratigraphy difficult at this site.

Physical property measurements, thermal conductivity, index properties, and natural gamma radiation all showed good hole-to-hole correlation, with due allowance for variation on short vertical scales and variances in sampling locations.

Downhole temperature data were reduced to in situ values and combined with the thermal conductivity measurements to determine a heat flow of 157 mW/m^2, which fits well to a young age for the crust underlying the Tyrrhenian Sea.

Interstitial water profiles at Site 974 show steady increases with depth of salinity, chlorinity, calcium, strontium, ammonium, and lithium. Evaporites, especially halite, anhydrite, and gypsum, known to occur below the sediments cored at Site 974, can provide the source for these variables. The downhole increase in calcium and strontium is most likely the result of an interaction of Messinian brines with background carbonates. High lithium concentrations suggest the presence of late-stage evaporitic brines. Ammonium concentrations are generally low, reflecting limited decomposition of organic matter.

BACKGROUND AND OBJECTIVES

Site 974 is located in the central Tyrrhenian Sea, about 215 km east of Sardinia, on the lower slope of the Sardinian continental margin, in a small basin more than 3400 m deep, bounded by north-northeast–trending normal faults. It lies on the western side of the De Marchi Seamount, approximately 20 km east of the major north-northeast–trending, east-southeast–dipping Tyrrhenian Central Fault (Fig. 1). The basin is underlain by thinned continental crust, which surrounds areas of Pliocene and Pleistocene oceanic crust (Vavilov and Marsili Basins) to the south and southeast. The site lies about 300 m west-northwest of Site 652, drilled during Leg 107 in 1986. The *Initial Reports* and *Scientific Results* volumes of that leg provide extensive information on the regional stratigraphy and tectonic setting (Kastens, Mascle, Auroux, et al., 1987; Kastens and Mascle, 1990). At a total depth of 721 mbsf, Site 652 reached calcareous sandstones and siltstones of possible Messinian age. Drilling at Site 974 penetrated and sampled sediments down to 203.7 mbsf (Fig. 2).

The Tyrrhenian basin opened during late Miocene–Pleistocene times as a backarc basin behind the Apenninic-Calabrian-Maghrebide subduction zone (Scandone, 1980; Rehault et al., 1984, 1987; Malinverno and Ryan, 1986; Royden et al., 1987; Channell and Mareschal, 1989; Doglioni, 1991). Extension in the Tyrrhenian basin overprinted an earlier orogenic belt, the remains of which are exposed in the Calabro-Peloritani Arc of southernmost Italy and northeastern Sicily. It consists of crystalline rocks that were deformed and metamorphosed under a wide variety of conditions during both the Hercynian and Alpine orogenies, plus Jurassic ophiolitic rocks and

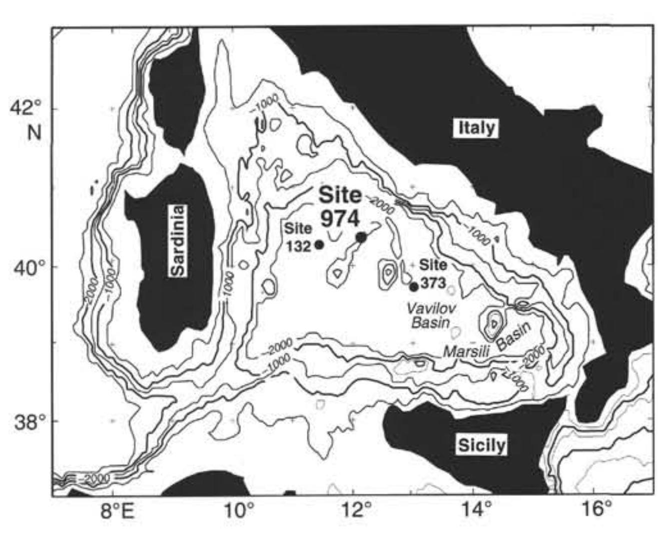

Figure 1. Bathymetric map of the Tyrrhenian Sea, showing the location of ODP Site 974 and DSDP sites in this region.

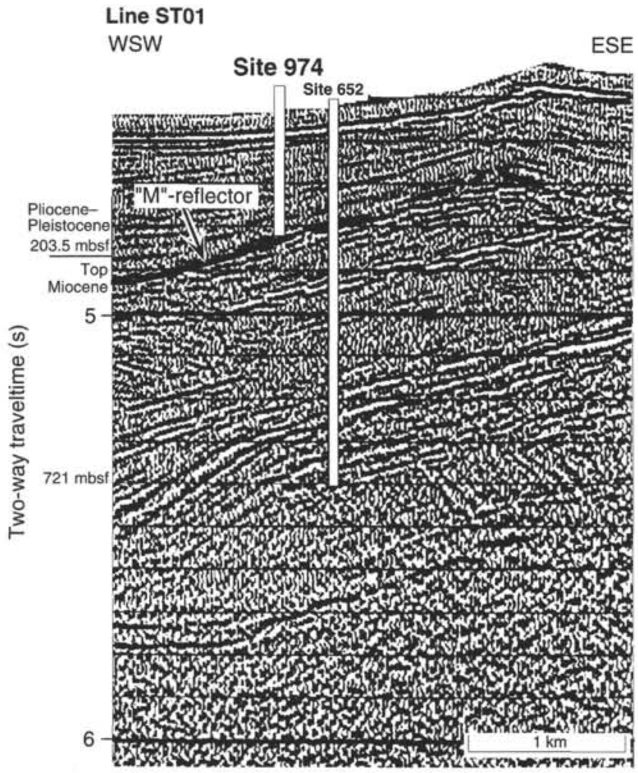

Figure 2. Detail of seismic line ST01 (shown in Fig. 3) showing the relative positions of Sites 652 and 974 and their total penetration.

Mesozoic to Tertiary sediments. Crystalline rocks belonging to this orogen have been dredged from the seafloor in the central-eastern Tyrrhenian Sea, suggesting that the crust was thickened during Alpine orogeny and stretched and rifted by backarc extension. Rifting was rapid across the Sardinian margin and continued from the Tortonian (upper margin) to the Pliocene (lower margin). The rough topography of the Tyrrhenian floor indicates the very recent tectonic activity of the area.

Site 974 is located near the top of a westward-tilted block, which is clearly depicted in seismic reflection profiles (Fig. 3; Rehault et al., 1987). This tilted block is on extremely thinned continental crust, near the inferred ocean-continent transition. The seismic reflectors indicate the presence of overlapping prerift, synrift, and postrift deposits above the tilted basement block (Kastens, Mascle, Auroux, et al., 1987; Kastens and Mascle, 1990). Biostratigraphic data from previously drilled Site 652 document that these deposits are of late Miocene (Messinian) to Pleistocene age.

At Site 652, eight organic-rich layers with organic carbon content ranging from 0.5% to >2.0% were retrieved from the Pliocene–Pleistocene sections. The discovery of these layers was significant in that it was the first time that sapropels or sapropel-like deposits had been retrieved in the western Mediterranean (Emeis et al., 1991). A second important outcome of Leg 107 drilling in the Tyrrhenian Sea was the discovery of large volcaniclastic deposits in the basin, with the occurrence of numerous volcaniclastic turbidites and volcaniclastic sands that appear to be related to major terrestrial volcanic eruptions (McCoy and Cornell, 1990). However, the rotary coring used at Site 652 resulted in discontinuous core recovery, and the recovered stratigraphic sequence was incomplete. The data acquired at Site 652 thus cannot be correlated to the chronologic framework of organic-rich sedimentation and volcaniclastic deposition obtained from other Mediterranean sites (Hilgen, 1991; Paterne and Guichard, 1993).

The primary objective of Site 974 was to obtain a complete Pliocene–Pleistocene sedimentary sequence that would contain a continuous record of organic-rich sedimentary events (sapropel intervals) in the Tyrrhenian Sea. In addition, Site 974 drilling was designed to retrieve a comprehensive record of Pliocene–Pleistocene volcaniclastic sedimentation to aid in developing a detailed tephrachronology that can be linked to the timing of volcanic eruptions on land.

We used the advanced hydraulic piston corer (APC) to ensure continuous recovery at three holes at Site 974. For two of these three holes the extended core barrel (XCB) was used to obtain the deeper sections that were too consolidated to recover using the APC. This drilling strategy has proven successful in ensuring that voids and intervals with drilling-induced disturbances in a single APC hole are recovered in an offset hole (see "Composite Depth" section, "Explanatory Notes" chapter, this volume).

OPERATIONS

Transit, Napoli to Site 974 (MedSap-5)

The ship departed Napoli at 1815 hr on 6 May. (All times in this report refer to ship time unless otherwise noted. Ship time was GMT + 2 hr, which is the same as European daylight savings time.) The 105-nmi sea voyage to MedSap-5 required 9.75 hr at an average speed of 10.8 nmi/hr. During the transit we collected navigation, 3.5 and 12 kHz reflection, and magnetic data.

Site 974

We deployed a Datasonics 354M beacon at 40°21.3′N, 12°08.59′E on 0345 hr, 7 May. This is the location of Site 652, which was drilled during ODP Leg 107. We deployed a second beacon about 175 m northwest of the first beacon. The first beacon was turned off and used as a back-up. The ship was positioned over the second beacon because the scientific party wanted to avoid Site 652 tailings.

Unless otherwise noted, depths in the operations section within individual site reports refer to meters below rig floor (mbrf). This depth is calculated using drill pipe measurements (DPM) from the top of the dual elevator stool (DES) on the rig floor. The DES is approximately 10.9 m (10.86 m for Holes 974A, 974B, and 974C; 10.89 m for Hole 974D) above sea level and varies over time depending on the ship's draft. The seafloor depth, and therefore the depth below seafloor (mbsf) from which cores are recovered, is calculated using the recovery of the mudline core at each hole, the DPM, and the elevation of the DES above sea level.

Hole 974A (MedSap-5)

Two APC/XCB holes to 200 mbsf and a third APC hole to refusal were planned for Site 974. An APC/XCB bottom hole assembly (BHA) was put together and used the entire leg for the APC/XCB holes. It consisted of the following: (1) one 11-7/16-in security roller cone bit (S/N 478458); (2) a bit sub (BS); (3) a seal bore drill collar (SBDC); (4) a landing saver sub (LSS); (5) a long top sub (LTS); (6) a head sub (HS); (7) a nonmagnetic drill collar (NMDC); (8) five 8-¼-in drill collars (DC); (9) one crossover sub (XO); (10) one 7-¼-in DC; (11) an XO sub; (12) five joints of 5-½-in drill pipe (DP); and (13) an XO sub.

A "rabbit" was sent through all of the drill pipe to ensure that the core barrels would pass through smoothly. Five stands of 5-in drill pipe were not used because the "rabbit" would not pass. As it was added to the drill string, the drill pipe was measured with a steel tape measure. Once assembled, a wiper "pig" was pumped through the

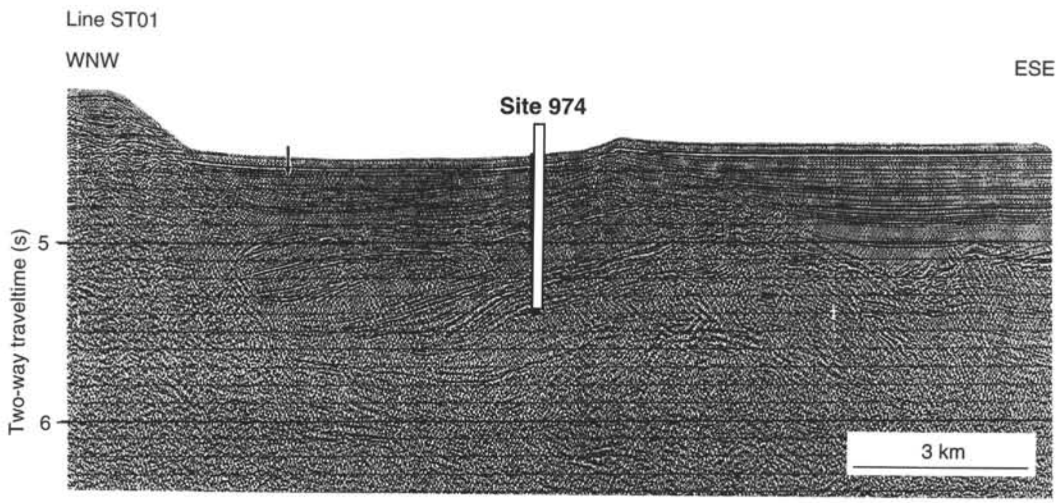

Figure 3. Seismic line ST01 across the lower Sardinian margin, showing the position of Site 974 on a small fault-bounded block. Note the dip toward west-northwest of the reflectors in the hanging wall of an east-dipping synsedimentary normal fault of Pliocene–Pleistocene age.

pipe and onto the seafloor to clean the inside of the DP of rust and lubricant used on the pipe connections.

Hole 974A was spudded at 1630 hr, 7 May, at 40°21.364′N, 12°08.506′E. The corrected precision depth recorder (PDR) indicated a water depth of 3474 mbrf. Core 974A-1H was taken with the bit at 3470.0 mbrf. Core 974A-1H, however, was full (9.81 m recovered; 103% recovery; Table 1; see also detailed coring summary on CD-ROM, back pocket, this volume) indicating that we missed the mudline and an exact seafloor measurement can only be assumed. Notes from the driller indicated that we may have lowered the bit into the seafloor by as much as 5 m before we shot Core 1H. Because we missed the mudline, Hole 974A was terminated and the bit cleared the seafloor at 1700 hr, 7 May.

Hole 974B

We raised the drill string from 3469.7 to 3462.0 m and spudded Hole 974B at 1730 hr, 7 May. Core 974B-1H recovered 6.78 m of sediment; therefore, the seafloor was determined to be at 3454 mbsl. Cores 1H through 18H were taken from 0 to 165 mbsf (3630 m) and recovered 172.73 m (105% recovery). We oriented Cores 3H through 18H using the Tensor tool.

Coring was interrupted for about 3.5 hr when one of three strands of the sandline parted at the oilsaver while retrieving Core 11H. Approximately 1050 m of sandline was removed from the aft sandline drum and the forward sandline was used for the remainder of Site 974.

Overpull (up to 40,000 lb) started at Core 16H and partial bleed-off indicated that there may have been a partial stroke. A partial stroke of about 6.5 m was inferred for Core 18H, both because the pressure had to bleed off and because the driller raised the drillstring 3 to 4 m before observing any resistance. Once it was retrieved on deck, we observed that the liner of Core 18H was shattered for nearly its entire length, most likely the result of a hard impact with the bottom of the borehole.

We started coring with the XCB at 3630 m (165 mbsf) after drilling out the 6.5-m rat hole created by Core 18H. Cores 19X through 22X were taken from 165 to 203.7 mbsf, with 38.7 m cored and 35.5 m recovered (92% recovery). The combined APC/XCB recovery for Hole 974B was 102%.

The depth objectives reached, we terminated Hole 974B and the bit cleared the seafloor at 2345 hr, 8 May. Hole 974B was completed in 30.75 hr.

Hole 974C

We offset the ship 50 m southeast and spudded Hole 974C at 0115 hr, 9 May, with the bit at 3459.0 m. Core 974C-1H recovered 4.36 m, and the seafloor was therefore defined to be 3453 mbsl. Cores 1H through 16H were taken to 146.8 mbsf (3611 m) and recovered 153.91 m (105% recovery). We stopped APC coring one core earlier than in Hole 974B in an attempt to prevent the liner from shattering and disturbing the core. ADARA temperature measurements were taken during Cores 3H, 6H, 9H, 12H, and 15H. All ADARA measurements were successful. There was no indication of any significant frictional heating due to tool movement.

Cores 17X through 22X were taken from 156.4 to 204.5 mbsf (3611–3668.7 m) with 57.7 m cored and 45.94 m recovered (80% recovery). Flow ports in the XCB shoe continued to become clogged in the clay; however, except for Core 17X, recovery was good.

The hole was conditioned for logging with a short wiper trip. No drag and only 6 m of sediment fill in the bottom of the hole indicated that conditions were good for logging. The hole was displaced with seawater. No potassium chloride or bentonite mud was used. The bit was positioned at 63.36 mbsf (3527.56 m) to log. The bit was raised approximately 20 m (to ~43 mbsf) before the logging tools reentered the drill pipe to allow more of the upper borehole to be logged. The quad combo tool was run first, then the FMS tool, and finally the geochemical tool. The logs were run to 3662, 3625, and 3656 mbrf, respectively. No significant operational or hole stability problems were reported. The logs indicated that hole angle was about 1.5°, and the hole diameter ranged from 12 to at least 15 in. We finished logging at 2045 hr, 10 May, and the bit cleared the seafloor at 2100 hr 10 May.

Hole 974D

We offset the ship 25 m to the northwest and spudded Hole 974D at 2245 hr, 10 May. The scientific party requested that the interval from 4 to 8 mbsf be recovered within a single core to fill in gaps from the previous holes. The bit was positioned at 3457.0 m and Core 974D-1H recovered 1.64 m; therefore, the seafloor was defined to be at 3454.0 mbsl. Cores 1H through 18H were taken to 163 mbsf (3628 m) and recovered 170.49 m (105% recovery). The beacons were released at 1300 and 1510 hr, 11 May, respectively, and were recovered at 1420 and 1600 hr, 11 May, respectively. The BHA cleared the rig floor and was secured for transit at 1930 hr, 11 May, and the transit to MedSap-6A began at 1930 hr, 11 May.

LITHOSTRATIGRAPHY

Unit Descriptions

Site 974 is located about 300 m west-northwest of Site 652, which was drilled during Leg 107. A comparison of core photographs from these sites indicates that both penetrated the same sedimentary se-

Table 1. Site 974 coring summary.

Core	Date (May 1995)	Time (UTC)	Depth (mbsf)	Length cored (m)	Length recovered (m)	Recovery (%)
161-974A-						
1H	7	1500	5.0–14.5	9.5	9.81	103.0
Coring totals:				9.5*	9.81	103.0
161-974B-						
1H	7	1530	0.0–6.5	6.5	6.78	104.0
2H	7	1715	6.5–16.0	9.5	9.94	104.0
3H	7	1830	16.0–25.5	9.5	9.86	104.0
4H	7	1945	25.5–35.0	9.5	9.94	104.0
5H	7	2045	35.0–44.5	9.5	9.88	104.0
6H	7	2145	44.5–54.0	9.5	9.90	104.0
7H	7	2245	54.0–63.5	9.5	9.96	105.0
8H	7	2330	63.5–73.0	9.5	9.95	105.0
9H	8	0015	73.0–82.5	9.5	10.05	105.8
10H	8	0100	82.5–92.0	9.5	10.16	106.9
11H	8	0605	92.0–101.5	9.5	9.90	104.0
12H	8	0715	101.5–111.0	9.5	10.05	105.8
13H	8	0825	111.0–120.5	9.5	9.93	104.0
14H	8	0915	120.5–130.0	9.5	10.19	107.2
15H	8	1020	130.0–139.5	9.5	9.58	101.0
16H	8	1130	139.5–149.0	9.5	10.04	105.7
17H	8	1250	149.0–158.5	9.5	9.74	102.0
18H	8	1420	158.5–165.0	6.5	6.87	105.0
19X	8	1630	165.0–174.9	9.9	6.93	70.0
20X	8	1800	174.9–184.5	9.6	9.80	102.0
21X	8	1910	184.5–194.1	9.6	9.86	103.0
22X	8	2030	194.1–203.7	9.6	8.91	92.8
Coring totals:				203.7	208.22	102.2
161-974C-						
1H	8	2330	0.0–4.3	4.3	4.36	101.0
2H	9	0030	4.3–13.8	9.5	9.84	103.0
3H	9	0200	13.8–23.3	9.5	10.13	106.6
4H	9	0245	23.3–32.8	9.5	9.70	102.0
5H	9	0330	32.8–42.3	9.5	10.08	106.1
6H	9	0445	42.3–51.8	9.5	10.07	106.0
7H	9	0530	51.8–61.3	9.5	9.82	103.0
8H	9	0620	61.3–70.8	9.5	10.04	105.7
9H	9	0725	70.8–80.3	9.5	9.94	104.0
10H	9	0810	80.3–89.8	9.5	10.04	105.7
11H	9	0900	89.8–99.3	9.5	9.99	105.0
12H	9	1000	99.3–108.8	9.5	9.93	104.0
13H	9	1100	108.8–118.3	9.5	9.88	104.0
14H	9	1210	118.3–127.8	9.5	9.84	103.0
15H	9	1325	127.8–137.3	9.5	10.17	107.0
16H	9	1430	137.3–146.8	9.5	10.08	106.1
17X	9	1600	146.8–156.4	9.6	0.18	1.9
18X	9	1700	156.4–166.1	9.7	9.19	94.7
19X	9	1800	166.1–175.7	9.6	9.60	100.0
20X	9	1930	175.7–185.3	9.6	9.67	101.0
21X	9	2050	185.3–194.9	9.6	9.69	101.0
22X	9	2215	194.9–204.5	9.6	7.61	79.3
Coring totals:				204.5	199.85	97.7
161-974D-						
1H	10	2115	0.0–1.5	1.5	1.64	109.0
2H	10	2200	1.5–11.0	9.5	9.70	102.0
3H	10	2245	11.0–20.5	9.5	9.79	103.0
4H	10	2320	20.5–30.0	9.5	9.69	102.0
5H	11	0000	30.0–39.5	9.5	9.81	103.0
6H	11	0045	39.5–49.0	9.5	9.95	105.0
7H	11	0130	49.0–58.5	9.5	9.84	103.0
8H	11	0215	58.5–68.0	9.5	10.13	106.6
9H	11	0300	68.0–77.5	9.5	9.86	104.0
10H	11	0340	77.5–87.0	9.5	10.13	106.6
11H	11	0420	87.0–96.5	9.5	9.85	103.0
12H	11	0505	96.5–106.0	9.5	10.05	105.8
13H	11	0550	106.0–115.5	9.5	9.88	104.0
14H	11	0645	115.5–125.0	9.5	10.03	105.6
15H	11	0730	125.0–134.5	9.5	9.81	103.0
16H	11	0810	134.5–144.0	9.5	10.19	107.2
17H	11	0900	144.0–153.5	9.5	10.02	105.5
18H	11	0955	153.5–163.0	9.5	10.12	106.5
Coring totals:				163.0	170.49	104.6

Notes: * = 0–5 mbsf believed not recovered. A detailed coring summary is contained on the CD-ROM, back pocket, this volume.

quence with similar downhole changes in lithology. Sediments at Site 974 are subdivided into three lithostratigraphic units (Table 2) based primarily on nannofossil (carbonate) content; unit boundaries were easily correlated among holes. Unit I was recovered at Holes 974A, 974B, 974C, and 974D; Unit II was recovered at Holes 974B, 974C, and 974D; and Unit III was recovered at Holes 974B and 974C. The stratigraphic column for Hole 974B is representative of those for all holes at Site 974 (Fig. 4).

Unit I

Hole 974A, 5.0–14.5 mbsf, Core 974A-1H;

Hole 974B, 0.0–88.9 mbsf, Core 974B-1H to Section 10H-5, 70 cm;

Hole 974C, 0–90.1 mbsf, Core 974C-1H to Section 10H-7, 97 cm;

Hole 974D, 0–89.8 mbsf, Core 974D-1H to Section 11H-2, 130 cm.

Unit I consists of Pliocene to Pleistocene hemipelagic deposits. The major lithologies are nannofossil-rich clay to nannofossil-rich silty clay with minor nannofossil clay. Geochemical analyses of the nannofossil-rich clay to silty clay and nannofossil clay intervals indicate an average carbonate content of 30% (see "Organic Geochemistry" section, this chapter). These sediments are locally bioturbated and exhibit thin to medium color banding, with colors ranging from light olive gray to pale yellowish brown to pale olive (Table 3).

Numerous vitric ash beds are present, some of which have been disseminated by bioturbation (Table 4; this table for 974B is representative for the site). Ash beds range from a few millimeters to more than 35 cm thick (Fig. 5). Sedimentary structures within these ash layers are limited to normal grading and faint lamination. Rounded pumice lapilli (10 mm) are present in a few ash layers (Fig. 6). Ash beds within this unit are locally altered to zeolites (phillipsite and analcime?) and clay minerals. Cemented, ash-rich zeolitic concretions(?) are found at the top of some ash layers (Fig. 7). Ash bed colors vary from olive and grayish black to gray (Table 3). Crystal-rich ashes tend to be darker than vitric ashes. Smear slides of the unaltered and less altered ash layers show a predominance of colorless glass with less tan and green glass, and crystals (e.g., feldspar, pyroxene, and biotite).

Unit I is characterized by the presence of many dark, organic-rich layers (ORLs; Table 5). The intervals containing ORLs show a characteristic series of colors: the interval with highest organic content is commonly olive black (5Y 2/1) to greenish black (5GY 2/1) to brownish black (5YR 2/1). The interval directly above the ORL is, in places, green (i.e., greenish gray [5GY 6/1], grayish green [10GY 5/2], grayish olive [10Y 4/2], or dusky yellow green [5GY 5/2]); the green interval may contain a thin, purple- to dark-greenish gray (5GY 4/1) lamina of authigenic opaque minerals (93.5 cm; Fig. 8). This is a simplified description; often the color banding associated with the ORLs is more complex (Figs. 9, 10). Smear slides of the black organic-rich intervals indicate that they are organic- and nannofossil-rich clays, with a few percent foraminifers, and a moderate percentage (5%–10%) of opaque minerals. Amorphous organic matter is present along with plant fragments and spores. Organic geochemical analyses confirm that some of the ORLs are sapropels in that they contain >1% TOC (total organic carbon) with a maximum of 6.43% TOC (Table 5; see discussion in "Organic Geochemistry" section, this chapter). Low TOC values for some thin ORLs (<1 cm) could be attributed to the incorporation of interbedded, organic-poor sediment within the interval sampled for shipboard geochemical analysis. We

Table 2. Lithostratigraphic units for Site 974.

Unit	Age	Lithology	Sedimentary structures	Occurrence	Interval (mbsf)
I	Pliocene to Pleistocene	Major:		Core 974A-1H	5.0–15.5
		Nannofossil-rich clay to nannofossil-rich silty clay	Bioturbation, thin to medium color banding	Core 974B-1H to Core 974B-10H-5, 70 cm	0.0–88.9
				Core 974C-1H to Core 974C-10H-7, 97 cm	0.0–90.1
				Core 974D-1H to Core 974D -11H-2, 130 cm	0.0–89.8
		Minor:			
		Vitric to crystal ash	Normal grading, faint lamination		
		Organic-rich layers	Color banding		
		Nannofossil clay	Bioturbation		
Unit I/Unit II boundary marked by slumping			Hole 974B: 90.5 to 109.5 mbsf; Hole 974C: 90–109 mbsf; Hole 974D: 88–106 mbsf.		
II	Pliocene	Major:		Core 974B-10H-5, 70 cm, to Core 974B-22X-4, 95 cm	88.9–199.55
		Nannofossil clay and nannofossil ooze	Bioturbation, medium color banding, soft-sediment deformation	Core 974C-10H-7, 97 cm, to Core 974C-22X-4, 92 cm	90.1–200.32
				Core 974D-11H-2, 130 cm, to Core 974D-18H-CC	89.8–163
		Minor:			
		Altered ash			
		Organic-rich layers			
III	Miocene	Clay, calcareous silty clay, silt, and sand	Parallel lamination, cross lamination, normal grading	Core 974B-22X-4, 95 cm, to CC	199.55–203.86
				Core 974C-22X-4, 92 cm, to CC	200.32–202.48

have ranked the ORLs according to their percent TOC (Types I through V; Table 5) and subdivided them into several descriptive types to assist in the correlation between holes: homogeneous (Fig. 8), color-banded (Fig. 9), and composite (Fig. 10). A total of 36 ORLs have been identified within Unit I and most of these correlate among Holes 974B, 974C, and 974D (Key beds T1 through T36; Tables 5, 6; Fig. 11). Hole 974D contains the most complete record, with 34 ORLs, whereas Hole 974B contains 32, Hole 974C contains 33, and Hole 974A contains one. The lower part of Unit I has been faulted and deformed; reverse faulting has repeated ORLs in Holes 974C and 974D (Fig. 9), whereas normal faulting may have removed ORLs at Holes 974B and 974C.

The boundary between Units I and II (Table 2) is located in a zone of soft-sediment deformation (slumping) that extends from the top of Unit II into the base of Unit I (for a detailed description, see "Structural Geology" section, this chapter). The most intense deformation is limited to the top of Unit II, where folded intervals alternate with homogenized and coherent sections. Local brecciation is also present; in one case, a brecciated unit is underlain by dewatering structures (Fig. 12).

Unit II

Hole 974B, 88.9–199.55 mbsf, Section 10H-5, 70 cm to Section 22X-4, 95 cm;
Hole 974C, 90.1–200.32 mbsf, Section 10H-7, 97 cm to Section 22X-4, 92 cm;
Hole 974D, 89.8–163 mbsf, Section 11H-2, 130 cm to Section 18H-CC.

The main lithologies of Unit II are light olive gray to pale olive (Table 3) nannofossil clay and nannofossil ooze with a minor amount of foraminifers. Geochemical analyses of the nannofossil clay and nannofossil ooze intervals indicate an average carbonate content of 50%. Minor ash beds within the upper part of this unit are locally altered to clay minerals and zeolites (Fig. 13). Minor concentrations of dark, altered coarse and fine ash are also present near the base of the unit (Fig. 14). Unit II exhibits thin to medium color banding with colors ranging from pale yellowish brown (10YR 6/2) to moderate yellow brown (10YR 5/4) to dusky yellow brown (5Y 6/4) to light olive brown (5Y 5/6). A few darker intervals are present in the lower part of this unit that have tentatively been identified as ORLs during visual description (see core descriptions for Cores 974B-15H, 16H, 17H, and 974D-14H, and 16H). TOC values for these intervals are very low (<0.2%; Cores 974D-14H and 16H).

Bioturbation is variable throughout Unit II. A transitional color change from olive gray to reddish brown occurs at the base of this unit, beginning in Cores 974B-21X and 974C-21X. Burrows within the reddish brown (oxidized) intervals are lighter in color (reduced), producing a mottled effect.

Unit III

Hole 974B, 199.55–203.86 mbsf, Section 22X-4, 95 cm to CC;
Hole 974C, 200.32–202.48 mbsf, Section 22X-4, 92 cm to CC.

At Site 652 (Leg 107), the Unit II/Unit III boundary was placed at the Miocene/Pliocene boundary, based on the last occurrence of in situ planktonic foraminifers. This boundary was accompanied by a measurable decrease in carbonate content within the sediments. At Site 974, the Miocene/Pliocene boundary occurs within Cores 974B-22X and 974C-22X (see "Biostratigraphy" section, this chapter). The Unit II/III boundary at Sites 652 and 974 is characterized by similar changes in sediment lithology, color, and degree of bioturbation. In Cores 974B-22X and 974C-22X, the lowermost part of Unit II consists of dark yellowish brown (10YR 4/2) to light olive gray (5Y 6/1) to light olive brown (5Y 5/6), moderately to intensely bioturbated nannofossil clay (Fig. 15). This lithology passes downhole into a sparsely bioturbated to non-bioturbated sequence of variegated brownish gray (5YR 4/1) to blackish red (5YR 2/2), horizontally laminated silty clay to clay, with light to dark greenish gray (5GY 8/1 to 5GY 4/1) calcareous interbeds (Figs. 16, 17). The top of Unit III marks a significant decrease in degree of bioturbation, the presence of parallel lamination, and a change from more orange/brown to red/brown colors. Smear-slide analyses indicate the presence of discrete clay-rich and calcareous intervals. Note that in Hole 974B, bedding throughout this unit shows a significant dip (15°W, see "Structural Geology" section, this chapter). As defined here, Unit III at Site 974 roughly correlates with Unit III and the uppermost part of Unit IV at Site 652.

The clay-rich intervals are highly variegated, and show millimeter- to sub-millimeter-scale lamination (Figs. 16, 17). These sediments are composed of low to moderately birefringent clay minerals and finely disseminated iron oxides. For the most part, they are rela-

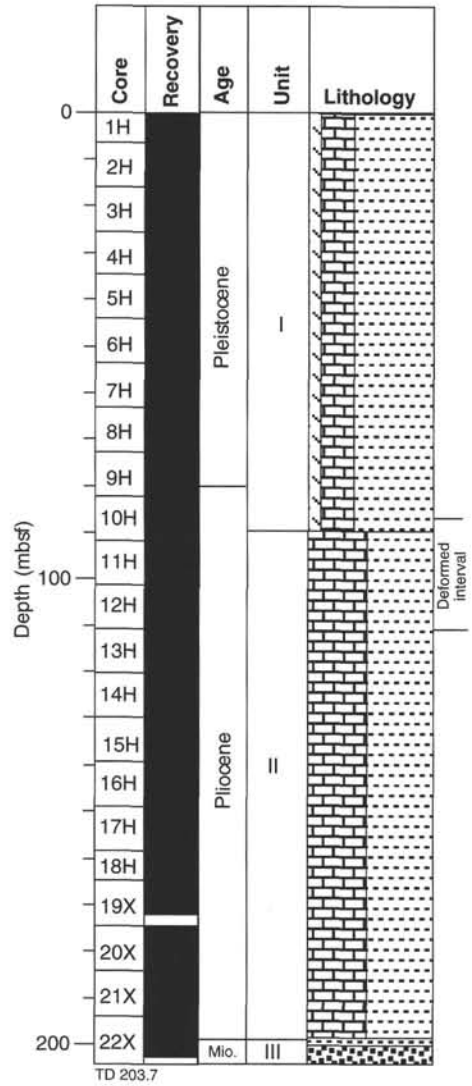

Figure 4. Generalized lithostratigraphic column and core recovery for Hole 974B. Stratigraphy is representative of that recovered at all Site 974 holes. The deformed interval, thought to be related to slumping, is located at the base of lithostratigraphic Unit I and the top of lithostratigraphic Unit II. The lithostratigraphic symbols are explained in Figure 1 of the "Explanatory Notes" chapter, this volume.

tively barren of microfossils, but, in some intervals, iron oxides form fine, clay- to silt-sized, micronodules that resemble "ghosts" of nannofossils. Other locally important components include pyrite, terrigenous organic matter, and a non-birefringent, prismatic mineral tentatively identified as a zeolite. The color of the clay-rich intervals changes within the unit from red/gold/black (oxidized) in Sections 974B-22X-4 and 974C-22X-4 to green/black (reduced) in Sections 974B-22X-5 and 974C-22X-5.

The calcareous, gray interbeds range from a few centimeters thick at the top of Unit III to >2 m thick at the base. The thinner intervals show fairly abrupt contacts with underlying and overlying clay laminae, but contact relationships are often obscured by drilling disturbance (Figs. 16, 17). These thin beds often consist of light/dark greenish gray couplets with apparent normally graded bases (silt to clay?). The lower, light micritic interval is overlain at a slightly gradational contact by dark greenish gray, calcareous silty clay. Smear

Table 3. Color variation of lithologies at Site 974.

Lithology	Colors
Nannofossil ooze	Yellowish gray (5Y 7/2) Greenish gray (5GY 6/1) Light greenish gray (5GY 8/1) Yellowish gray (5Y 8/1)
Nannofossil clay to nannofossil silty clay	Pale olive (10Y 6/2) Light olive gray (5Y 6/1) Light olive gray (5Y 5/2)
Nannofossil-rich clay to nannofossil-rich silty clay	Light olive gray (5Y 5/2) Olive gray (5Y 4/1) Olive gray (5Y 3/2) Dark yellowish brown (10YR 4/2) Pale yellowish brown (10YR 6/2)
Clay to silty clay with nannofossils	Greenish black (5GY 2/1)
Ash	Olive black (5Y 2/1) Grayish black (N2) Medium gray (N5) Dark gray (N3) Light olive gray (5Y 6/1) Olive gray (5Y 4/1) Grayish olive (10Y 4/2)
Organic-rich layer	Olive black (5Y 2/1) Greenish black (5GY 2/1) Brownish black (5YR 2/1)

slides of these couplets indicate that the basal, light greenish gray graded interval is predominantly composed of fine, clay-sized, uniformly granular micrite with some silt-sized recrystallized nannofossils, whereas the darker interval is composed of calcareous silty clay with a significant terrigenous silt component (e.g., quartz, feldspar, mica) and rare gypsum crystals. The micritic component of the darker intervals is distinctly different from the lighter intervals in that it consists of silt- to clay-sized carbonate with variable morphology, reflecting various origins (e.g., bioclastic debris, nannofossils, authigenic rhombs).

Downsection, the light-gray intervals within the couplets become thinner and less distinct, as the sequence becomes more sand rich. The sand-to-silt fraction in this lower interval is composed of detrital carbonate and other terrigenous debris with minor gypsum crystals. The base of Unit III contains two greenish gray, coarse clastic beds. The top, thinner interval is shown in Figure 18. The laminated clay directly below this interval is organic-rich and slightly bioturbated. At a contact probably modified by drilling disturbance, the clay abruptly passes into a ripple-cross-laminated fine sand that grades upward into calcareous silty clay (Tc, Td, and Te? divisions of Bouma [1962]). The lower, thicker bed consists of a basal coarse to medium sand (lower contact not recovered) that grades upward into cross-laminated very fine sand, followed by alternating homogeneous to horizontally laminated nannofossil-rich to calcareous silty clay (Ta, Tc, Td, and Te? divisions of Bouma [1962]).

Interpretation of Sediments Recovered at Hole 974A

Units I and II

The pelagic to hemipelagic sediments of Units I and II contain calcareous nannofossil and foraminifer assemblages that are consistent with open marine conditions and deposition in lower bathyal to abyssal depths above the CCD (carbonate compensation depth), with occasional reworking from shallower depths ("Biostratigraphy" section, this chapter). The shift from more pelagic sedimentation in Unit II to more hemipelagic sedimentation in Unit I probably reflects greater terrigenous input during the Pleistocene, as indicated by an upward increase in apparent sediment accumulation rates from 31.1 m/my in Unit II to 55.1 m/my in Unit I (see "Biostratigraphy" section, this chapter). A concomitant increase in rate of sediment accumulation on the slopes of the basin may have led to increased instability

Table 4. Ash-bearing layers* at Hole 974B.

Core, section, interval** (cm)	Thickness (cm)
161-974B-	
1H-1, 35.0	≤1
1H-1, 70.0	≤1
1H-1, 82.0	6
1H-1, 120.0	3
1H-1, 146.0	≤1
1H-2, 1.0	≤1
1H-2, 24.0	≤1
1H-2, 45.0	≤1
1H-2, 68.0	≤1
1H-2, 82.0	≤1
1H-2, 86.0	≤1
1H-2, 88.0	≤1
1H-2, 102.0	≤1
1H-2, 116.0	≤1
1H-3, 48.0	12
1H-3, 130.0	10
1H-4, 15.0	2
1H-4, 35.0	≤1
1H-5, 30.0	≤1
2H-1, 28.0	1
2H-1, 36.0	4
2H-1, 98.0	≤1
2H-1, 131.0	≤1
2H-1, 135.0	≤1
2H-2, 46.0	≤1
2H-2, 49.0	≤1
2H-2, 68.0	7
2H-2, 85.0	2
2H-2, 112.0	≤1
2H-3, 0.0	3
2H-3, 20.0	3
2H-3, 77.0	11
2H-3, 140.0	≤1
2H-4, 0.0	150
2H-5, 0.0	37
2H-5, 61.0	4
2H-5, 104.0	≤1
2H-5, 121.0	≤1
2H-6, 38.0	≤1
2H-6, 42.0	3
2H-7, 8.0	4
2H-7, 47.0	≤1
3H-1, 5.5	10
3H-1, 42.0	≤1
3H-1, 78.0	≤1
3H-2, 0.0	4
3H-2, 53.0	≤1
3H-2, 85.0	≤1
3H-2, 117.0	≤1
3H-2, 136.0	3
3H-3, 66.0	≤1
3H-3, 128.0	≤1
3H-3, 130.0	3
3H-4, 2.0	≤1
3H-4, 20.0	30
3H-4, 70.0	≤1
3H-4, 81.0	≤1
3H-4, 86.0	≤1
3H-4, 107.0	≤1
3H-4, 109.0	≤1
3H-5, 4.0	≤1
3H-5, 9.0	≤1
3H-5, 50.0	≤1
3H-5, 90.0	≤1
3H-5, 107.0	≤1
3H-5, 118.0	≤1
3H-6, 58.0	≤1
3H-6, 68.0	≤1
3H-6, 94.0	≤1
3H-6, 103.0	2
3H-6, 144.0	2
3H-7, 10.0	≤1
3H-7, 18.0	≤1
3H-CC, 15.0	3
4H-1, 10.0	≤1
4H-1, 30.0	≤1
4H-1, 76.0	≤1
4H-1, 85.0	≤1
4H-1, 106.0	2
4H-2, 48.0	≤1
4H-2, 69.0	≤1
4H-2, 76.0	2
4H-2, 119.0	≤1
4H-2, 129.0	5?
4H-4, 45.5	≤1
4H-4, 91.0	2
4H-4, 97.0	1
4H-4, 106.0	2
4H-4, 114.0	2
4H-5, 13.0	3
4H-6, 7.0	2
4H-6, 72.0	≤1
4H-6, 82.0	5
4H-6, 99.0	≤1
4H-6, 115.0	3
4H-6, 120.0	≤1
4H-6, 127.0	≤1
4H-6, 132.5	≤1
5H-1, 60.0	7
5H-1, 100.0	≤1
5H-2, 10.0	≤1
5H-2, 14.0	≤1
5H-2, 18.0	≤1
5H-2, 60.0	≤1
5H-2, 61.5	≤1
5H-2, 110.0	5
5H-3, 76.0	9
5H-4, 0.0	20
5H-4, 20.0	3
5H-4, 57.0	2
5H-4, 74.5	≤1
5H-4, 130.0	
5H-5, 36.0	20
5H-5, 69.0	≤1
5H-5, 76.0	2
5H-5, 98.0	4
5H-5, 103.5	8
5H-6, 10.0	25
5H-6, 60.0	≤1
5H-6, 110.0	≤1
5H-7, 18.0	2
5H-7, 37.0	≤1
5H-7, 49.0	≤1
5H-CC, 8.0	2
6H-1, 17.0	3
6H-1, 36.0	≤1
6H-1, 38.0	≤1
6H-1, 90.0	≤1
6H-2, 32.0	
6H-2, 60.0	≤1
6H-3, 43.0	≤1
6H-3, 110.0	≤1
6H-4, 52.0	1
6H-4, 86.0	5
6H-4, 122.0	≤1
6H-4, 130.0	2
6H-4, 137.0	≤1
6H-4, 139.0	1
6H-4, 149.0	2
6H-5, 68.0	4
6H-5, 72.0	2
6H-6, 7.0	≤1
6H-6, 89.0	1
7H-3, 80.0	5
7H-4, 76.0	7
7H-5, 66.0	≤1
7H-5, 140.0	≤1
7H-6, 10.0	60
7H-7, 22.0	≤1
8H-2, 103.0	4
8H-3, 22.0	≤1
8H-3, 38.0	3
8H-6, 13.0	≤1
8H-7, 31.0	≤1
9H-2, 34.0	12
9H-6, 33.0	112
10H-1, 25.5	1
10H-3, 31.0	2
10H-4, 134.0	≤1
10H-5, 53.0	2
10H-6, 2.0	≤1
10H-6, 6.0	≤1
10H-6, 16.0	≤1
10H-6, 18.0	≤1
10H-6, 20.0	≤1
10H-6, 21.0	≤1
10H-6, 73.0	44
11H-2, 101.0	29
11H-3, 10.0	5
11H-3, 19.0	≤1
11H-3, 77.0	73
11H-4, 0.0	30
11H-5, 117.0	23
11H-7, 6.0	≤1
11H-7, 8.0	≤1
11H-7, 33.0	33
11H-CC, 0.0	26
12H-1, 63.0	4
12H-1, 87.0	4
12H-3, 33.0	5
12H-4, 120.0	3
12H-5, 32.0	3
12H-5, 100.0	20
12H-7, 1.0	73
12H-CC, 18.0	6
13H-1, 20.0	30
13H-1, 50.0	2
13H-1, 108.0	42
13H-1, 133.0	2
13H-4, 58.0	92
13H-5, 24.0	5
13H-5, 44.0	2
13H-6, 13.0	≤1
13H-6, 34.0	≤1
13H-6, 87.0	≤1
13H-6, 138.0	≤1
14H-1, 45.0	≤1
14H-3, 27.0	2
14H-4, 1.0	8
14H-4, 85.0	≤1
14H-4, 86.0	34
14H-5, 96.0	≤1
14H-5, 104.0	1
14H-6, 7.0	≤1
14H-5, 8.0	31
14H-6, 39.0	≤1
14H-6, 126.0	≤1
15H-1, 21.0	≤ 1
15H-1, 145.0	≤1

Note: * = ash occurrence based on visual identification in core. Many of these intervals may not be classified as ashes based on the compositional scheme outlined in the "Explanatory Notes" chapter (this volume).
** = top of ash interval, including dispersed ash and laminated bedded ash.

and down-slope displacement of material, generating the slumped interval that marks the Unit I/Unit II boundary. Although a similar interval of deformed sediment is present in Site 652 cores, shipboard scientists did not recognize this deformation as primary, and attributed it to drilling disturbance associated with rotary drilling. Some drilling disturbance is obvious in the Site 652 core photographs (e.g., Cores 107-652A-10R and 11R), but soft-sediment deformation similar to that observed in Site 974 cores is also apparent. In addition, local seismic events could have triggered this and other minor slumped intervals found in Unit I.

The source of terrigenous mud within Units I and II could have been the continental shelf regions off Italy, Corsica, or Sardinia. Any cyclic variation in pelagic and hemipelagic input possibly present within Unit I is masked by the frequent occurrence of ash layers and ORLs, which impart strong textural and color overprints on the sequence. The sediments in Unit II are predominantly the product of pelagic accumulation, with visibly structureless thin intervals of more hemipelagic sediment.

The organic-rich layers within Units I and II could be associated with periods of anoxia or higher productivity. The appearance of these organic-rich layers, that is, homogeneous, color-banded, and composite, likely reflects variable conditions during formation or perhaps during burial diagenesis, but the origin of these variations remains equivocal. We observed no unique sedimentary structures or textures within the Site 974 ORLs that would reflect their mode of sedimentation. Our preliminary work suggests that the ORLs appear to be the product of hemipelagic sedimentation with a superimposed increase in the percentage of pelagic marine organic matter.

Site 974 is located at the northern margin of the Tyrrhenian Sea in a magmatically active backarc basin (Malinverno and Ryan, 1986; Savelli, 1988). As summarized by McCoy and Cornell (1990), there are several possible sources of volcaniclastic material at this site: (1) the Tuscan, Roman, and Campanian volcanic provinces active on mainland Italy along the eastern margin of the basin; (2) the Eolian magmatic arc at the southern end of the basin; and (3) intrabasinal volcanic seamounts (e.g., Mount Vavilov). Sedimentary structures observed in the ash layers at Site 974 are limited to graded bedding and lamination. These structures could have resulted from subaerial eruption of volcanoes and airfall into the basin, followed by settling to the seafloor, or from marine redistribution through gravity flow

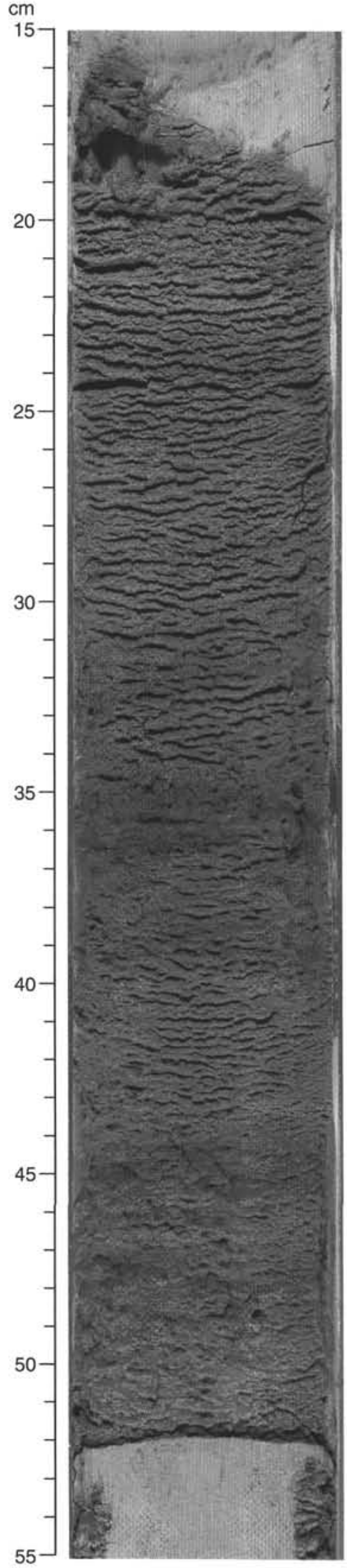

Figure 5. Vitric ash layer from Section 974B-3H-4 (20.65–21.05 mbsf). Smear-slide analysis from the interval 40–41 cm yielded a composition of 60% glass, 5% zeolite, 5% feldspar, and 30% clay.

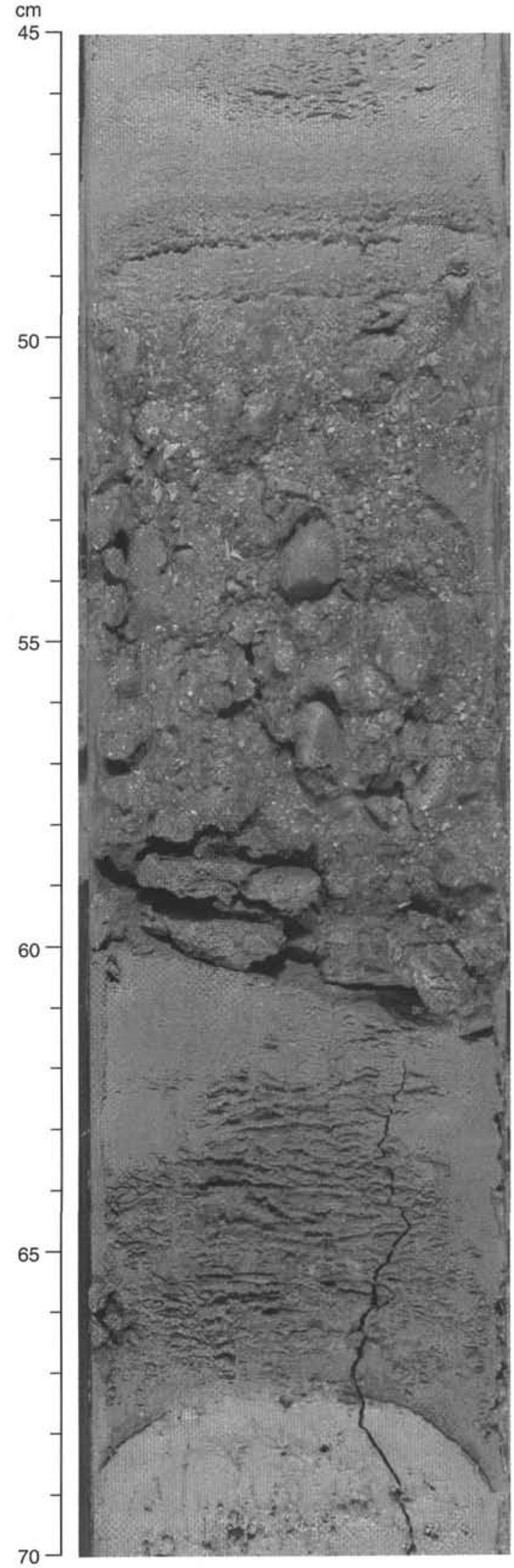

Figure 6. Medium gray ash-rich interval from Section 974B-1H-3 (3.45–3.68 mbsf) consisting of: (a) fine ash above an abrupt basal contact (60–68 cm), (b) poorly sorted, pteropod-rich (millimeter-scale white specks) coarse ash with rounded pumice lapilli (50–60 cm), topped by (c) laminated to massive fine ash (45–50 cm).

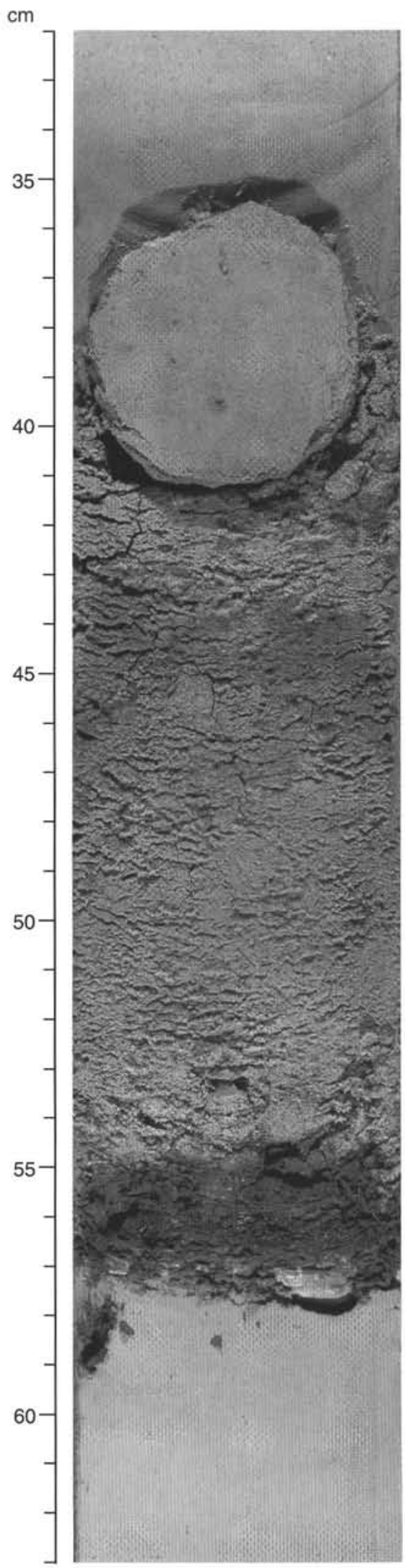

Figure 7. A zeolite-cemented layer developed over an altered (phillipsite-rich) ash bed in Sample 974B-5H-5, 32–63 cm (41.33–41.64 mbsf). The coarse base of the ash bed is the darkest interval (55–57 cm). The circular shape of the cemented layer is a product of drilling. The layer was rotated 90° when core was split using wire.

processes (e.g., turbidity currents). Both of these depositional mechanisms were favored by McCoy and Cornell (1990) in their study of similar ash layers from Site 652. In addition, some disseminated to thin ash intervals may have been produced during submarine eruptions of intrabasinal volcanoes.

Unit III

Reddish hues in the sediments above and at the Unit II/III boundary were attributed by Leg 107 shipboard scientists (Kastens, Mascle, Auroux et al., 1987) to input of clay minerals and iron oxides from subaerially weathered soils along the basin margin. Cita et al. (1990) believe that hematitic soils developed on a karstified carbonate ridge between Sardinia and Sicily could have been eroded and deposited in the Tyrrhenian basin during incursion of Atlantic waters and the transition from lacustrine to marine sedimentation at the end of the Messinian. However, high heat flow and the likely complex history of sediment pore-water geochemistry at this site do not preclude a diagenetic origin for the color variation of this interval.

Regional seismic stratigraphy suggests that Units III and IV at Site 652 and, by correlation, Unit III at Site 974, represent synrift sediments deposited in a half graben (Borsetti et al., 1990; Kastens, Mascle, Auroux et al., 1987). Furthermore, Unit III at Site 974 likely records the transition from lacustrine to normal marine sedimentation in this region. Results from Site 652 indicate that, at Site 974, only the uppermost few meters of a thick (hundreds of meters) lacustrine sequence consisting of rhythmically bedded, sparsely fossiliferous calcareous gray claystone, mudstone, sandy siltstone, and sandstone with evaporitic intervals and fine laminated intervals (Kastens, Mascle, Auroux et al., 1987) were recovered. These sediments have been correlated (Borsetti et al., 1990) with the onshore "Lago Mare" facies (Sissingh, 1976; Cita et al., 1980) and interpreted to have accumulated in a closed freshwater lake that periodically became saline and may have experienced marine incursions (Robertson et al., 1990; Borsetti et al., 1990). Like the equivalent sections at Site 652, the sediments of Unit III contain sedimentary structures consistent with lacustrine sedimentation, and also sparse in situ fauna (See "Biostratigraphy" section, this chapter; Cita et al., 1990). Additional evidence for lacustrine sedimentation comes from carbon and oxygen isotopic analysis of sedimentary calcite at Site 652. Pierre and Rouchy (1990) found significant negative shifts in oxygen (5 per mil, $\delta^{18}O$) and carbon (2 per mil, $\delta^{13}C$) isotopic values across the transition zone (equivalent to the Unit II/III boundary at Site 974) indicating a shift from meteoric lacustrine (Unit III at Site 974) to normal marine (Unit II at Site 974) sedimentation. The nannofossil-bearing gray couplets and sandy clastic interbeds within Unit III at Site 974 could represent the products of episodic marine incursion accompanied by erosion of the marginal "sill" area, and density current transport and deposition within the basin.

BIOSTRATIGRAPHY

Calcareous Nannofossils: Abundance and Preservation

Cores recovered at Site 974 contain abundant, mostly well-preserved Pleistocene to latest Miocene calcareous nannofossils. In the oldest sediment, Sections 974B-21X-CC and 974C-22X-CC, nannofossils are less abundant and preservation is moderate. Sample 974C-22X-4, 150–151 cm, was barren of nannofossils. Sample 974C-22X-5, 18–19 cm, contains common nannofossils with a rich diversity.

Biostratigraphy

Hole 974A

Only one core was taken in Hole 974A. Section 974A-1H-CC lacks *Emiliania huxleyi* and *Pseudoemiliania lacunosa* and is assigned to Zone NN20.

Table 5. Correlation of organic-rich layers from Site 974.

Type	Key bed number	Core, section, interval (cm)	Top (mbsf)	Bottom (mbsf)	TOC (%)	Core, section, interval (cm)	Top (mbsf)	Bottom (mbsf)	TOC (%)	Core, section, interval (cm)	Top (mbsf)	Bottom (mbsf)	TOC (%)
		161-974B-				**161-974C-**				**161-974D-**			
II	T1	1H-CC, 7–17	06.640	6.740	1.71	—				2H-3, 82–90	5.020	5.082	
II	T2	3H-3, 13.5–18.5	19.135	19.185	1.51	3H-2, 63.–68.5	15.930	15.985	1.25	3H-5, 26–32	17.260	17.320	
I	T3	—				3H-7, 8.5–19	22.885	22.990	2.07	—			
II	T4	4H-5, 21–32	31.710	31.820	1.58	4H-4, 121–130	29.037	29.100		4H-6, 114.5–122	29.145	29.220	
II	T5	4H-5, 94–114	32.440	32.640	1.70	4H-5, 37.5–59	29.670	29.890	1.97	4H-7, 30.5–49.5	29.805	29.995	
I	T6	5H-1, 54–55	35.540	35.550		5H-1, 20–31.5	33.000	33.115		5H-3, 41.5–56	33.415	33.560	
		5H-1, 65–72	35.650	35.720	3.15				3.13				
I	T7	5H-2, 45.5–49.5	36.955	36.995	2.59	5H-2, 5.5–9.5	34.355	34.395	2.92	5H-4, 25.5–29	34.755	34.790	
		5H-2, 55–65.5	37.050	37.155	2.17	5H-2, 15.5–24	34.455	34.540	1.78	5H-4, 35.5–44.5	34.855	34.945	
III	T8	5H-2, 131–133	37.810	37.830		5H-2, 86–90	35.160	35.200	(0.64)	5H-4, 110–112.5	35.600	35.625	
V	T9	?5H-3, 133–135	39.330	39.350		5H-3, 72–73	36.520	36.530		5H-5, 107.5–111	37.075	37.110	
III	T10	5H-4, 23–27	39.730	39.770		—				5H-6, 0.5–6	37.505	37.560	(0.64)
I	T11	6H-5, 3–10.5	50.530	50.605	4.25	6H-5, 36.5–46.5	48.665	48.765	4.56	6H-7, 28–37	48.780	48.870	
II	T12	6H-5, 19.5–23.5	50.695	50.735	1.13	6H-5, 57.5–63.5	48.875	48.935	1.40	6H-7, 46.5–51.5	48.965	49.015	
I	T13	6H-5, 132.5–137.5	51.825	51.875	4.03	6H-6, 25.5–30	50.055	50.100	4.31	7H-1, 53.5–58	49.535	49.580	
III	T14	6H-5, 146–147.5	51.960	51.975	0.53	6H-6, 38–39	50.180	50.190	0.87	7H-1, 66–69	49.660	49.690	
I	T15	6H-6, 78.5–87	52.785	52.870	2.35	6H-6, 116–124	50.960	51.040	2.93	7H-1, 145.5–150	50.455	50.500	
										7H-2, 0–4	50.500	50.540	
I	T16	6H-7, 59.5–66	54.095	54.160	3.09	6H-CC, 31–37	52.200	52.260	3.48	7H-2, 124.5–130	51.745	51.800	
						7H-1, 8–14.5	51.880	51.945	3.46				
								overlap					
						Repetition by faulting							
I	T17	7H-1, 116–121	55.160	55.210	6.43	7H-2, 30.5–38.5	53.605	53.685	5.27	7H-3, 135.5–143	53.355	53.430	
		7H-2, 0–3	55.210	55.240									
IV	T18	7H-2, 66.5–67.5	55.875	55.885	(0.34)	7H-2, 101–102	54.310	54.320		7H-4, 46–46.5	53.960	53.965	
I	T19	7H-5, 24.5–26.5	59.955	59.975	1.94	7H-5, 122–125	59.020	59.050	2.54	7H-CC, Paleosample?	58.790	58.840	
I	T20	7H-5, 96–99.5	60.670	60.705	2.09	7H-6, 44–47	59.740	59.770	3.04	8H-1, 51.5–55	59.015	59.050	
										8H-4, 46–46.5	63.460	63.465	
										8H-4, 66–66.5	63.660	63.665	
III	T21	8H-1, 105–107	64.550	64.570	(0.60)	8H-2, 70–71	63.500	63.510		8H-4, 78–83.5	63.780	63.835	
I	T22	8H-4, 8–14	67.980	68.040	3.91	8H-5, 14–22	67.440	67.520		8H-6, 119–127	67.190	67.270	
V	T23	8H-4, 74–76	68.640	68.660		8H-5, 91–92	68.210	68.220		8H-7, 40–42	67.900	67.920	
I	T24	8H-5, 85–89	70.250	70.290	2.20	8H-6, 102–105	69.820	69.850		9H-1, 115–117	69.150	69.170	
I	T25	8H-6, 60–63	71.500	71.530	2.67	8H-CC, 11–15	71.160	71.200		9H-2, 100–101.5	70.500	70.015	
V						9H-1, 3.5–5	70.835	70.850		9H-2, 104.5–109.5	70.545	70.595	
						Repetition by faulting				Repetition by faulting			
II	T26	9H-1, 128–131	74.280	74.310	1.87	9H-3, 42.5–45	74.225	74.250		9H-4, 124.5–127.5	73.745	73.775	
II	T27	9H-3, 4.5–6	75.945	75.960	1.52	9H-4, 53–54	75.830	75.840		9H-5, 144–145.5	75.440	75.455	
V	T28	?9H-3, IW	77.350	77.400		9H-5, 27–28	77.070	77.080		9H-6, 126.5–128	76.765	76.780	
V	T29	—				9H-6, 105–107	79.350	79.370		—			
						Faulting area							
I	T30	9H-5, 140.5–146	80.305	80.360	2.72	10H-2, 53–62	82.330	82.420		10H-1, 147–150	78.970	79.000	
										10H-2, 0–6	79.000	79.060	
										10H-4, 40.5–49	82.405	82.490	
										Repetition by faulting			
II	T31	10H-1, 8–11.5	82.580	82.615	1.82	10H-3, 17–20	83.270	83.300		10H-2, 72.5–82.5	79.725	79.825	
										10H-4, 113–128.5	83.130	83.285	
										Repetition by faulting			
V	T32	—				—				10H-3, 6–6.5	80.560	80.565	
										10H-5, 43–44	83.930	83.940	
										Repetition by faulting			
V	T33	—				10H-5, 4.5–7	86.145	86.170		10H-6, 89–94	85.890	85.940	
I	T34	10H-3, 16–34.5	85.360	85.545	2.38	10H-5, 34–45	86.440	86.550		10H-6, 124–131	86.240	86.310	
I	T35	10H-4, 59–62.5	87.290	87.325	2.95	10H-6, 126–129	88.860	88.890		11H-1, 0–3	87.000	87.030	
V	T36	10H-5, 59–61	88.790	88.810		10H-7, 89–90.5	89.990	90.005		11H-2, 4–7	88.540	88.570	
										11H-2, 101–102.5	89.510	89.525	
										11H-2, 122.5–126	89.755	89.760	

Notes: At Hole 974A, key bed number T1 is found in Core 1H-1, 100–108 cm (6.000–6.080 mbsf). TOC in % as determined from the difference between total carbon and carbonate carbon (see "Organic Geochemistry" section, this chapter). — = missing from section. Type: I = >2% TOC; II =1%–2% TOC; III = 0.5%–1% TOC; IV = <0.5% TOC; V = TOC not determined; ( )= TOC values for ORLs with possible admixture of background sediment.

Holes 974B, 974C, and 974D

Figures 19–21 show the zonal assignments of each core in Holes 974B, 974C, and 974D, together with the occurrence of the species that define the zonal boundaries or are used as secondary markers. Some of the sequence of zones and subzones do not appear in Figures 19–21. These missing zones/subzones do not necessarily mean that hiatuses exist; most, if not all, the zones/subzones will probably be found when samples located higher in each core are examined post-cruise.

Hole 974B (Fig. 19)

The Pliocene/Pleistocene boundary coincides closely with the NN19A-NN19B Subzonal boundary. This boundary is therefore approximated by the FO of *Gephyrocapsa caribbeanica* or by *G. oceanica* (forms larger than 4.0 µm). It is located between Samples 974B-9H-4, 71–72 cm (NN19B), and 974B-9H-6, 25–26 cm (NN19A). The lower/upper Pliocene boundary is close to the NN15-NN16 zonal boundary. The lower/upper Pliocene boundary is indicated in Figure 19 at the LCO of *Reticulofenestra pseudoumbilicus*

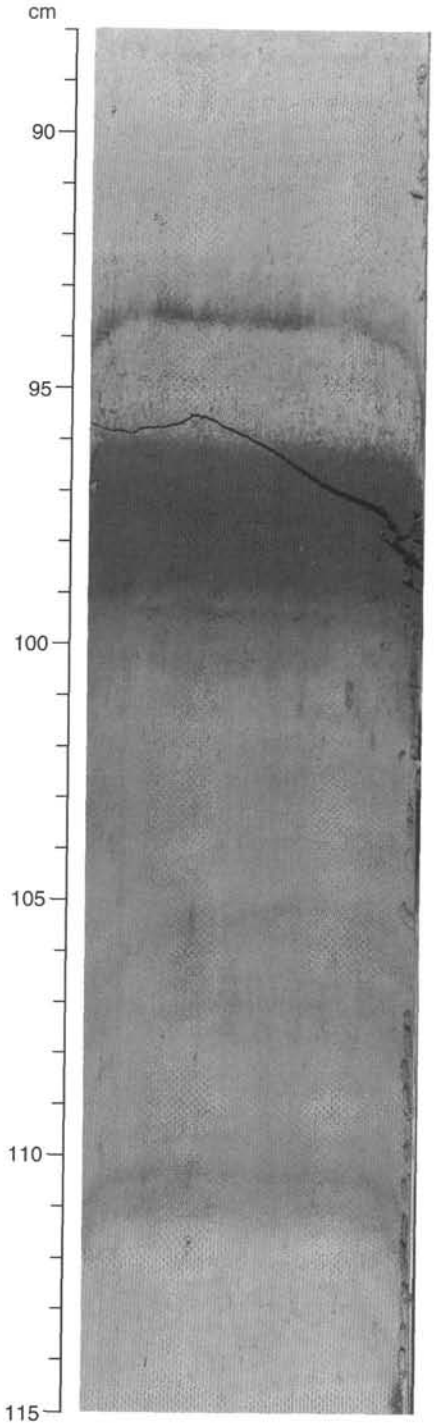

Figure 8. Example of a Pleistocene homogeneous ORL from Sample 974B-7H-5, 88–115 cm (60.59–60.86 mbsf). The total organic carbon content of the interval 97–98 cm is 2.09%.

(forms larger than 7.0 µm) in Sample 974B-16X-2, 30–31 cm. The lower Pliocene/upper Miocene boundary falls within Zone NN12. The FO of the Ceratolith group is used to mark the Miocene/Pliocene boundary (Zones NN12a/NN12b). Because of the rare occurrence of these forms, the extinction of *Helicosphaera intermedia,* occurring within Zone NN12 (top of Subzone NN12b), is used in these cores to

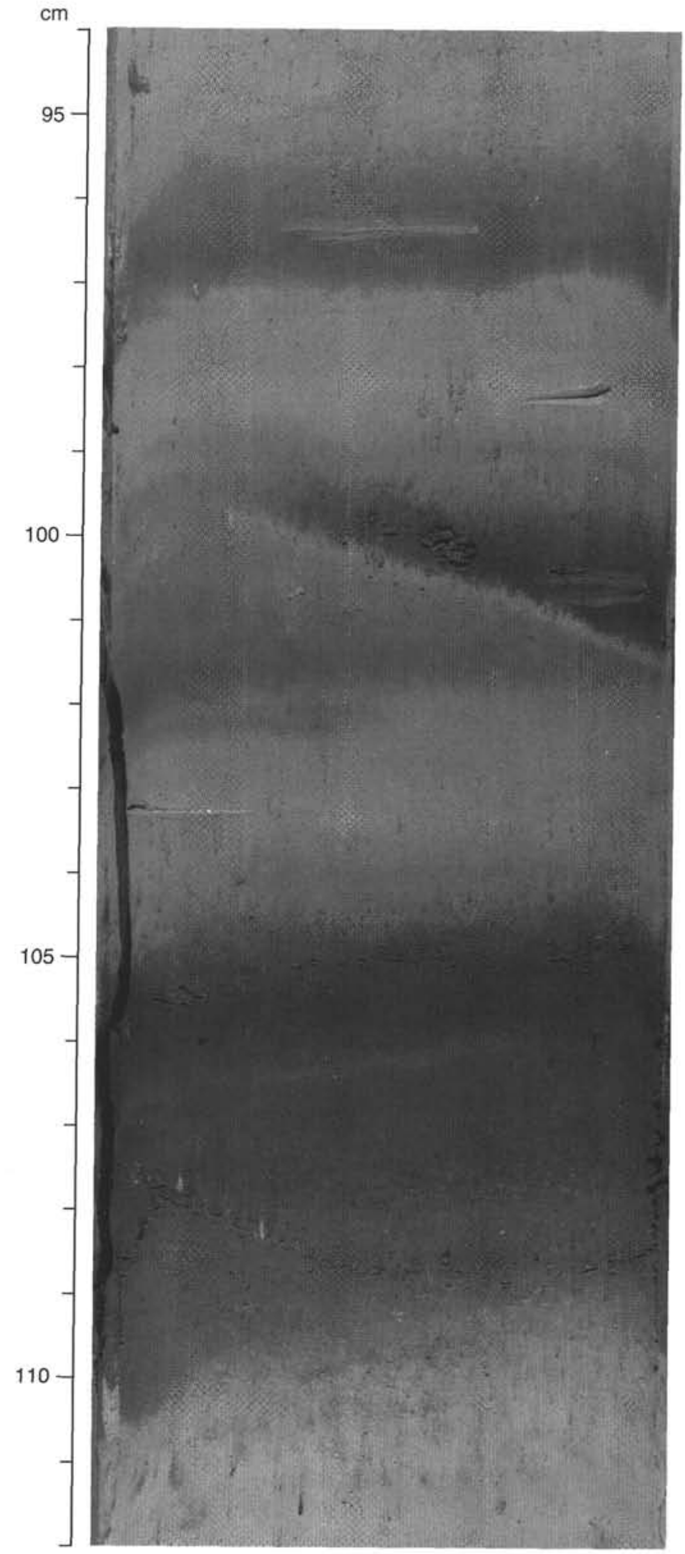

Figure 9. Example of a Pleistocene color-banded ORL from Section 974D-9H-2 (70.44–70.62 mbsf). The layer has been repeated by a reverse fault that cuts the core across interval 99–102 cm. The total organic carbon content for this ORL was not determined.

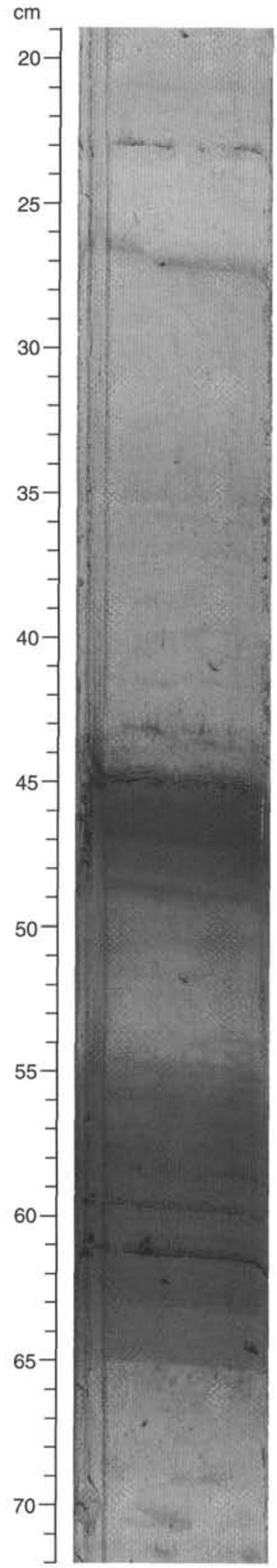

Figure 10. Example of a Pleistocene composite ORL from Section 974B-5H-2 (36.69–37.22 mbsf). The total organic carbon content of the interval 46–47 cm is 2.59%.

Table 6. Summary of organic-rich layers from Site 974.

Type	Pleistocene	Pliocene	Total
I	13	3	16
II	7	1	8
III	4	0	4
IV	1	0	1
V	4	3	7
Total	29	7	36

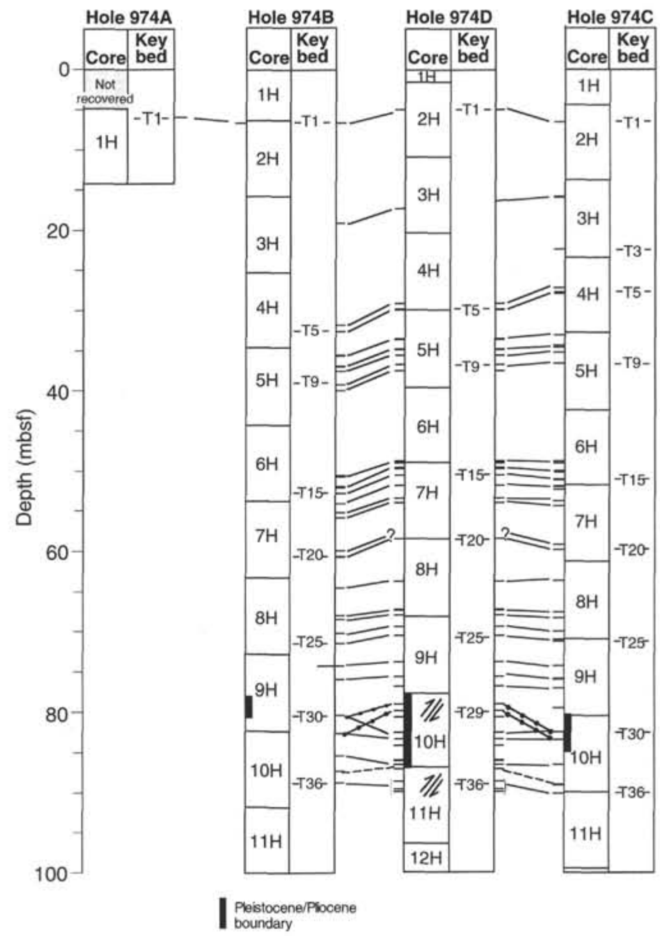

Figure 11. Correlation of ORLs in Site 974 holes. The Pleistocene/Pliocene boundary is most precisely constrained in Hole 974B (Core 974B-9H, between Sections 4 and 6), and less constrained in Holes 974C (between Sections 974C-9H-CC and 10H-4) and 974D (between Sections 974D-9H-CC and 12H-CC) (see "Biostratigraphy" section, this chapter).

approximate the boundary. The uppermost Miocene was identified in Sample 974B-22X-5, 18–19 cm (presence of *Discoaster quinqueramus* var. A; de Kaenel and Villa, 1996).

Hole 974C (Fig. 20)

Several core intervals were assigned to undifferentiated zonal intervals because of the low sampling resolution. All Pleistocene zones are identified. The Pliocene/Pleistocene boundary is located between Samples 974C-9H-CC (Zone NN19B) and 974C-10H-4, 33–35 cm (Zone NN19A). The lower/upper Pliocene boundary is approximated by the last common occurrence of *R. pseudoumbilicus,* which occurs in Sample 974C-15H-CC. The lower Pliocene/upper Miocene

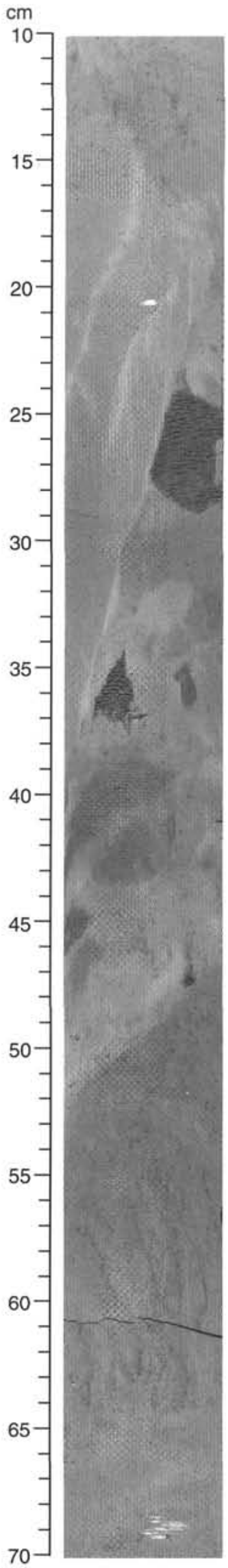

Figure 12. A breccia of gravel-sized clasts of mixed lithologies, including dark altered ash and light nannofossil clay (13–50 cm), overlies, at an angular contact (47–52 cm), clay with well-developed dewatering veins (50–64 cm). Sample 974C-13H-4, 10–70 cm (113.40–113.98 mbsf).

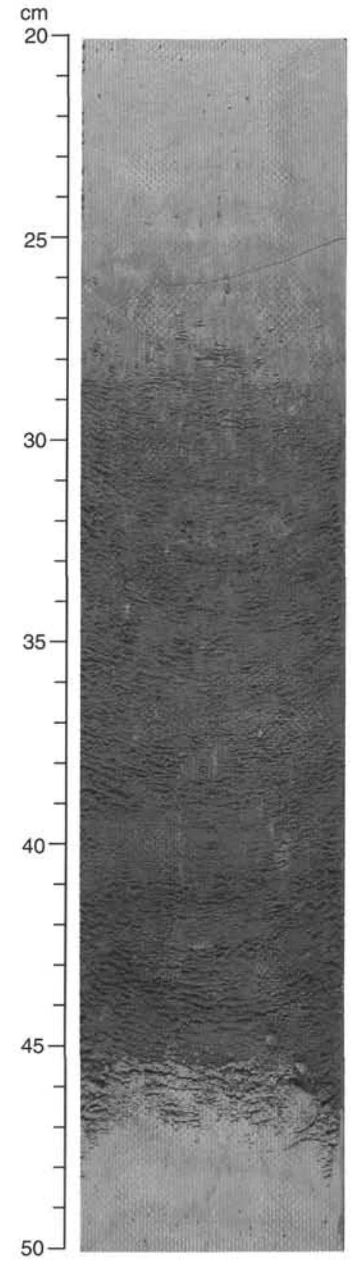

Figure 13. Altered ash layer from Sample 974B-13H-5, 20–50 cm (117.20–117.50 mbsf). Smear-slide analysis at 42–43 cm indicates virtually complete alteration of original vitric components to clay (75%) and zeolites (15%); the remaining 10% is nannofossils, probably mixed into the interval by bioturbation.

boundary falls within Core 974C-22X, but was not determined accurately. Sample 974C-2X-CC is located within Zone NN11.

Hole 974D (Fig. 21)

Zones NN13, NN14, NN15, NN16B, NN17, and NN18 were not identified in samples from this hole. Samples 974D-2H-CC through 6H-CC are assigned to Subzone NN19F, and Samples 974D-7H-CC to Subzone NN19E. Samples 974D-8H-CC through 9H-CC are assigned to the undifferentiated Subzone NN19D-NN19C. The Pliocene/Pleistocene boundary occurs between Samples 974D-9H-CC and 10H-CC. The NN14-NN15 boundary, which approximates the lower/upper Pliocene boundary based on the last common occur-

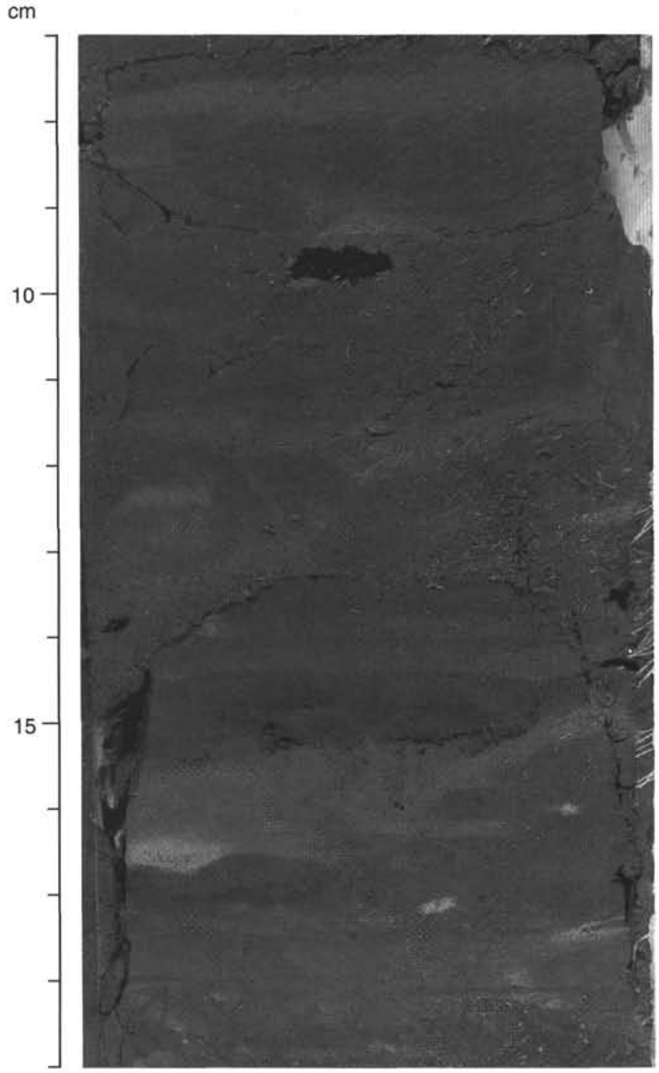

Figure 14. Dark coarse ash at 9.5–10 cm and fine ash concentration at 15.5 cm. Sample 974C-22X-4, 7–19 cm (199.47–199.59 mbsf).

rence of *R. pseudoumbilicus* (>7.0 µm), falls between Samples 974D-17H-CC and 18H-CC.

Planktonic Foraminifers: Abundance and Preservation

Cores recovered at Site 974 contain abundant, mostly well-preserved Pleistocene to earliest Pliocene foraminiferal assemblages. Sections 974B-13H-CC and 974C-13H-CC yield a very poor assemblage and abundant siliciclastic material (volcanic ash, according to the lithologic description). Sections 974D-4H-CC, 5H-CC, 6H-CC are barren or very poor in foraminiferal content. The abundance and preservation is rather poor in the basal part of Cores 974B-22X and 974C-22X, which was interpreted as indicating non-marine environment during the latest Miocene (Messinian). In all, 127 samples were examined.

Biostratigraphy

Biozones, the distribution of zonal markers, and sampling intervals are shown in Figures 22–24.

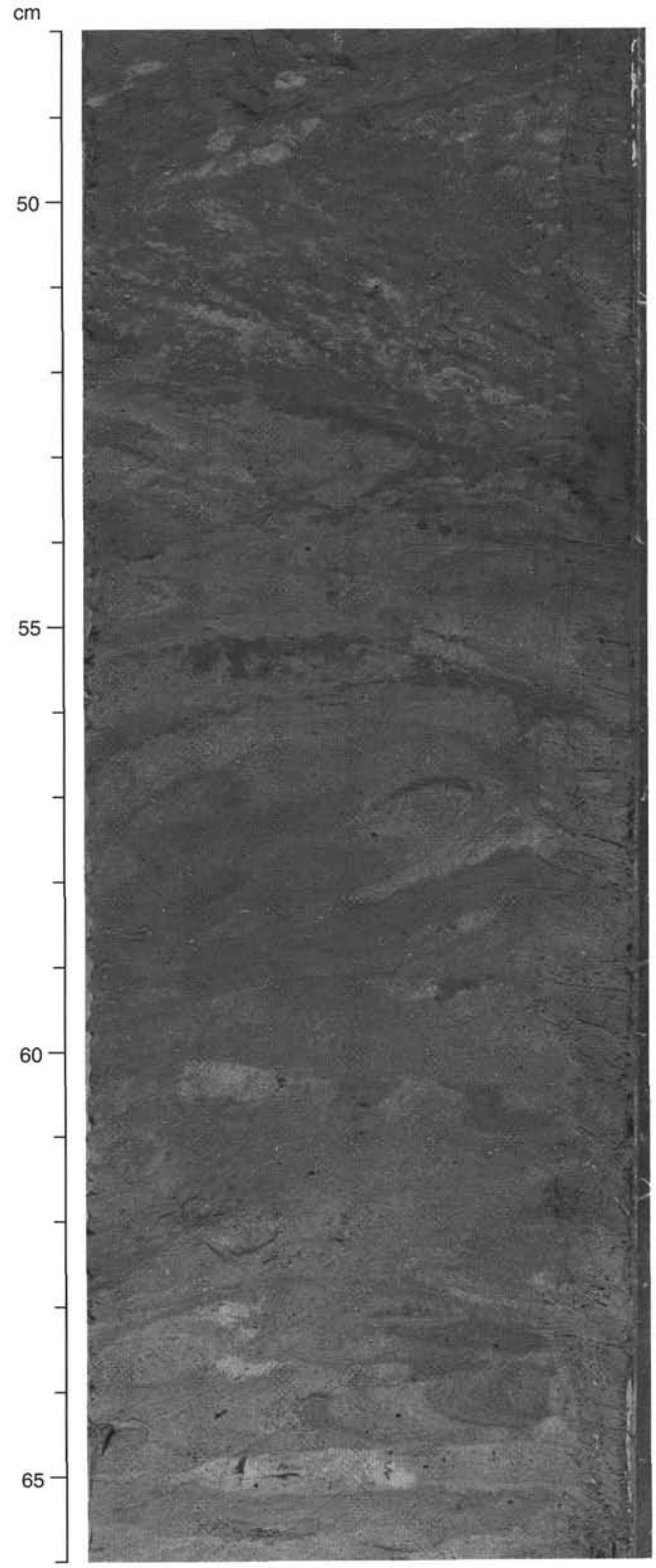

Figure 15. Intensely bioturbated zone near base of Unit II in Sample 974B-22X-4, 48–66 cm (199.08–199.26 mbsf).

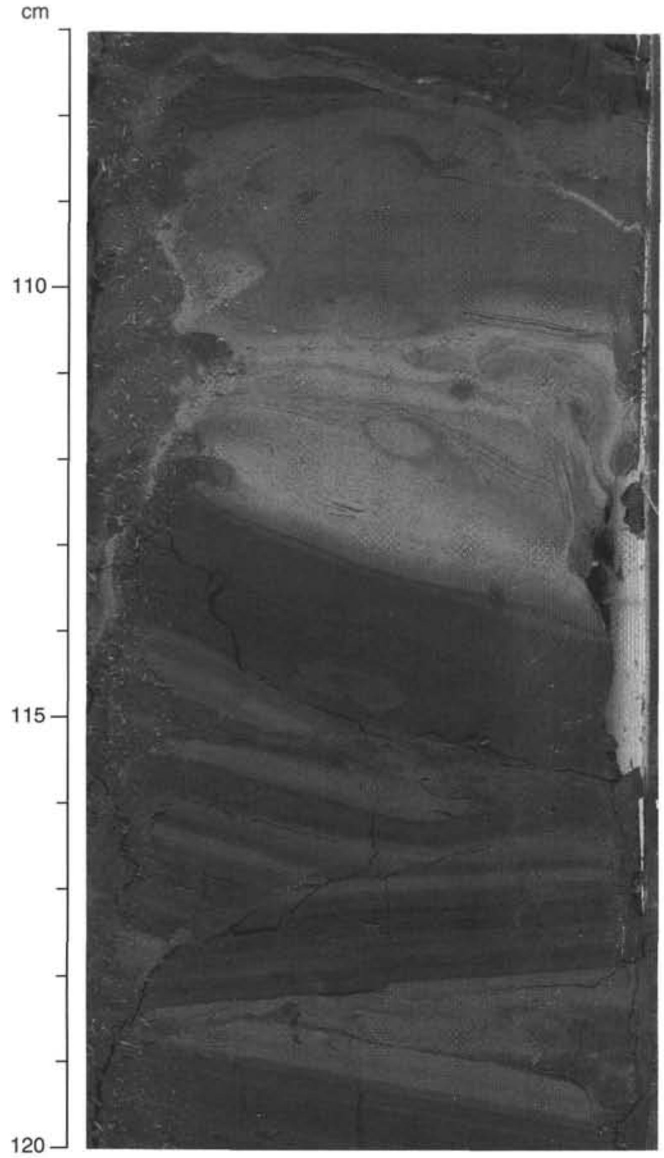

Figure 16. One couplet of dark gray calcareous silty clay (top) and light gray micrite (bottom) (108–112.5 cm), interbedded with dark gray to black finely laminated clay. Note isolated burrow in light gray micrite at 111.5 cm. Slightly dipping beds in this interval have been biscuited and rotated by XCB coring. Sample 974B-22X-4, 107–120 cm (199.66–199.82 mbsf).

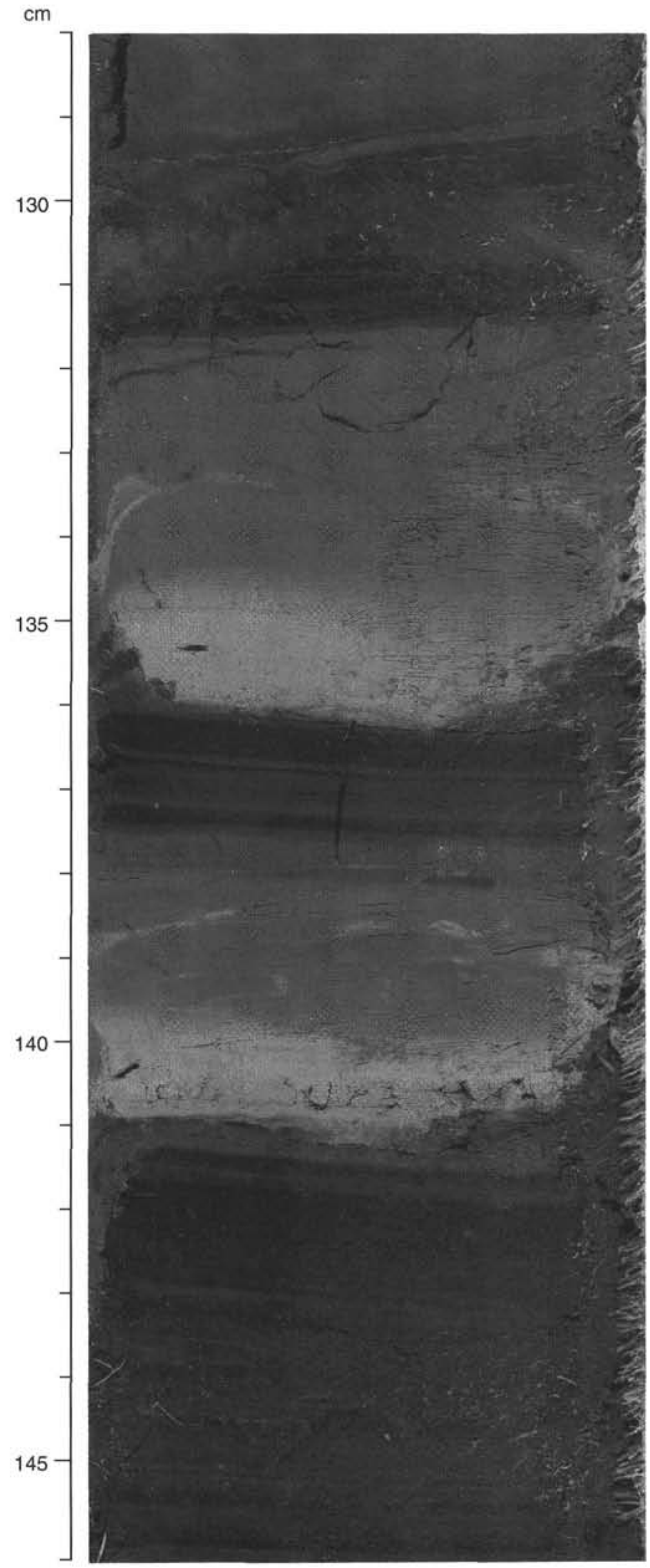

Figure 17. Two couplets (132.5–136 cm and 138.5–140.5 cm) of dark gray calcareous silty clay (top) and light gray micrite (bottom), interbedded with dark gray to black finely laminated clay. Sample 974C-22X-4, 128–146 cm (200.68–200.86 mbsf).

Hole 974A

Sample 974A-1H-CC yields a Pleistocene assemblage that cannot be assigned to a distinct biozone as no significant markers were detected. The most common and significant taxa are *Neogloboquadrina dutertrei, N. pachyderma, Globigerina bulloides, G. cariacoensis,* and the *G. scitula* group.

Hole 974B (Fig. 22)

A 198-m-thick Pliocene–Pleistocene sequence was recovered at Site 974B. Below this interval, the base of the sequence is composed of several meters of perhaps non-marine sediments and gypsum that are most probably Messinian in age (see "Lithostratigraphy" section, this chapter).

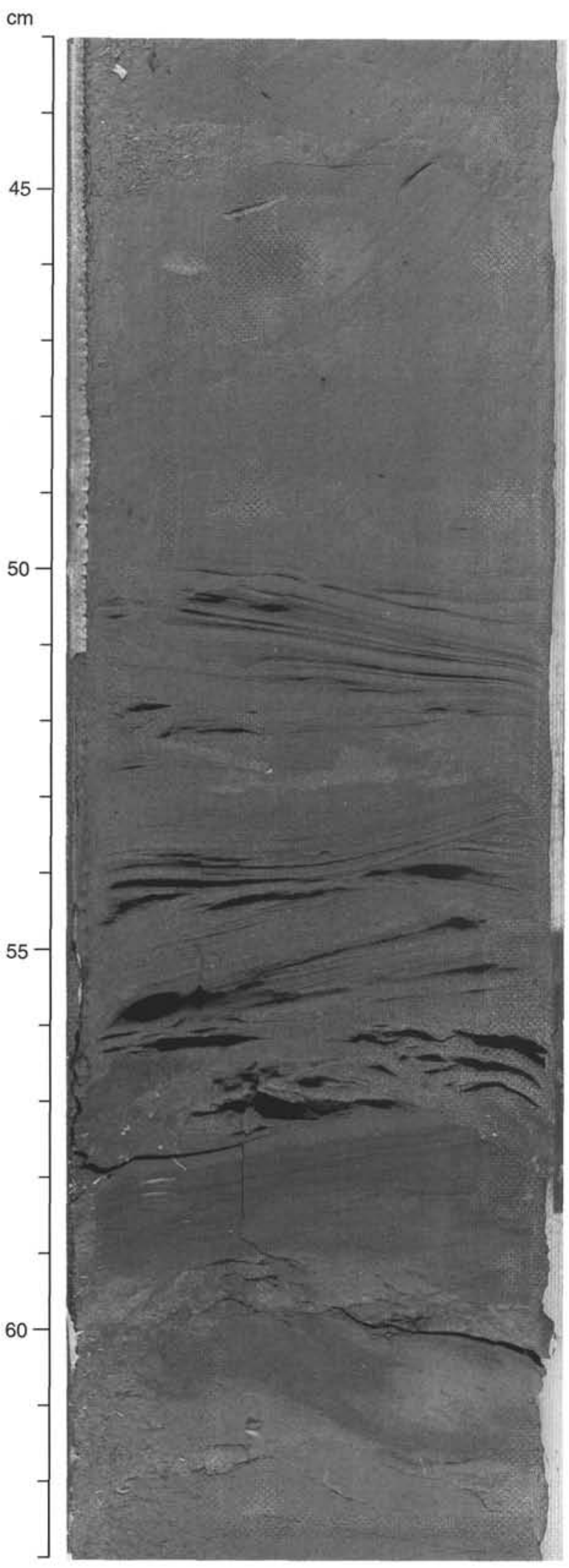

Figure 18. Thin sandy bed within Unit III in Sample 974B-22X-5, 43–63 cm (200.35–200.73 mbsf). Bioturbated to laminated, organic-rich clay (58–59 cm) abruptly overlain (contact probably modified by drilling disturbance) by ripple-cross-laminated fine sand (Tb; 50–58 cm), in turn overlain by finely laminated calcareous silty clay (Td). T is from Bouma (1962) index.

The base of the *G. cariacoensis* Zone, as defined by the increase of *N. pachyderma* (sinistral coiling), was placed at Sample 974B-9H-4, 71–73 cm (78.11 mbsf), where some specimens of *N. pachyderma* (sinistral coiling) were observed. As a result, the Pleistocene sequence is about 78 m thick.

All eight Pliocene foraminiferal biozones were recognized and occur between 82 and 198 mbsf. The interval from Sample 974B-20X-CC (184.5 mbsf) down to Sample 974B-22X-2, 123–125 cm (196.83 mbsf) was assigned to MPL1 because *Globorotalia margaritae* was not observed; *Sphaeroidinellopsis* spp., which is generally abundant in this interval is rare. At the base of this biozone *Sphaeroidinellopsis* spp. is absent, and the planktonic assemblage is dominated by *Globigerina* spp. and *Orbulina universa.* The Miocene/Pliocene boundary (Messinian/Zanclean boundary) occurs between Samples 974B-22X-4, 72–74 cm, and 974B-22X-4, 93–95 cm. In samples from 974B-22X-4, 144–145 cm (200.04 mbsf) down to the base of the drilled sequence (203.7 mbsf), planktonic foraminifers are absent (Sample 974B-22X-4, 144–145 cm), show indications of being fragmented by reworking, or are characterized by dwarfed assemblages. By correlation to Site 652 (Leg 107), this interval is assigned to the upper Miocene "Messinian Lago Mare" facies (Shipboard Scientific Party, 1987).

Hole 974C (Fig. 23)

A Pliocene–Pleistocene sequence 204.5 m thick was recovered in Hole 974C. As in Hole 974B, the base of the Pliocene is probably underlain by non-marine sediments assigned to the Messinian.

The Pleistocene interval is not clearly identified through planktonic foraminifers. In fact, the markers which characterize the biozones were not detected in the investigated samples. However, the interval from Sample 974C-1H-CC (5.27 mbsf) down to, at least, Sample 974C-8H-4, 60–62 cm (66.4 mbsf) is Pleistocene in age. The most common taxa are *Globorotalia inflata, O. universa, Globigerinoides ruber, N. pachyderma* (dextral coiling), and *G. cariacoensis. N. dutertrei, Beella digitata,* and *N. pachyderma* (sinistral coiling) are discontinuously present.

The Pliocene/Pleistocene boundary was not recognized in the samples studied. However, all Pliocene zones are present. Zone MPL3, defined by the co-occurrence of *G. margaritae* and *Globorotalia puncticulata,* occurs in Sample 974C-16H-6, 110–112 cm (145.90 mbsf), down to Sample 974C-17X-CC (146.80 mbsf). The thickness of this zone is very short and certainly does not correspond to the interval's actual thickness. Note that the depth (mbsf) for Sample 974C-17X-CC is shallower than the depth for Sample 974C-16H-CC above it because of the ODP convention of calculating mbsf-depths when cores have more than 100% recovery. We recognize that Sample 974C-17X-CC does in fact sequentially follow the Sample 974C-16H-CC. The lowermost Zanclean assemblage (Zone MPL1) occurs in Sample 974C-22X-3, 40–42 cm. From Sample 974C-22X-3, 144–146 cm (199.34 mbsf), to the bottom of the hole, sediments are barren or yield very few foraminifers. As in Hole 974B, the barren interval should also correlate to the "Messinian Lago Mare" facies (Shipboard Scientific Party, 1987).

Hole 974D (Fig. 24)

Hole 974D recovered a Pliocene–Pleistocene sequence similar to that of Holes 974B and 974C. The base of the sequence at 163.62 mbsf is lower Pliocene (Zone MPL2). Shipboard analyses for Hole 974D were carried out only on core catcher samples. Moreover, Samples 974D-4H-CC and 6H-CC yielded a very poor foraminiferal assemblage, and Samples 974D-2H-CC and 5H-CC were barren, all possibly due to turbidites observed in this part of the core (see "Lithostratigraphy" section, this chapter), reducing the biostratigraphic resolution in Hole 974D. The Pleistocene biozones were not recognized, whereas most of the Pliocene biozones occurring in the sequence were detected. Only Zone MPL3 was not recorded, but it

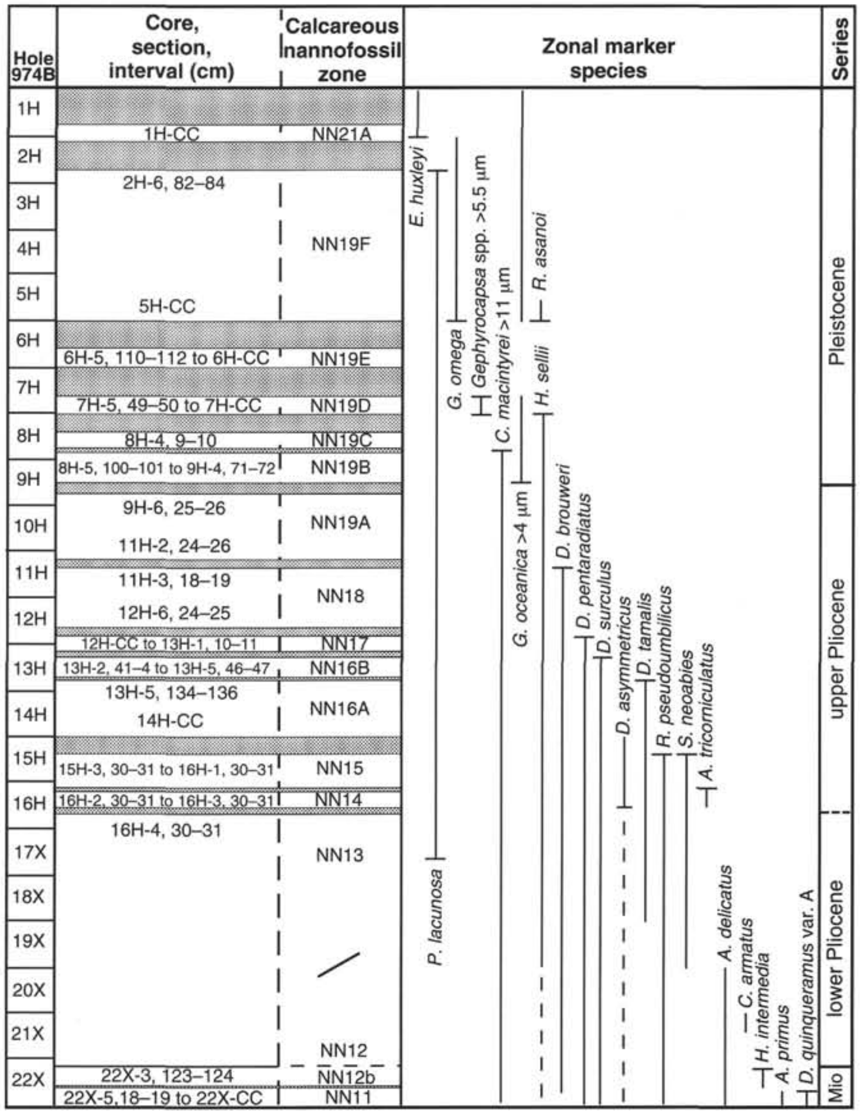

Figure 19. Calcareous nannofossil zonation of Hole 974B. Dashed horizontal lines indicate boundaries defined between core-catcher samples. Dashed vertical lines indicate the irregular occurrence of *H. sellii* and *D. asymmetricus* in the Miocene. Missing zones or subzones do not imply hiatuses. The zones/subzones may be in sections not yet examined.

may be present in the interval not investigated between Samples 974D-17H-CC and 18H-CC.

Benthic Foraminifers

Benthic foraminifers were very rare (<0.5%), very small (<150 µm), and dominated by deep-water forms in the Pleistocene. Textulariids were of the deep-water variety. The upper 20 mbsf at this site were either barren or specimens confined to the pan residue (<150 µm size fraction). Pteropods and sporadic phosphatic remains were also found in the upper 20 mbsf of sediment.

Deeper than 20 mbsf, in Sample 974B-3H-CC (25.6 mbsf), large *Pyrgo* spp. and *Bulimina aculeata* are common. Other deep-water milioliids were often present, notably *Articulina tubulosa* (e.g., Sample 974B-6H-CC, 54.16 mbsf). For the remainder of the Pleistocene, benthic foraminifers were rare and were composed of deep-water forms.

In Pliocene samples below Core 974B-10H, deep-water foraminifers were slightly more abundant and generally larger. Although their numbers remained extremely low (<0.5%), the species assemblage composition changed somewhat, with *Oridorsalis stellatus, Cibicidoides robertsonianus,* and *Gyroidina laevigata* species being more common than in the Pleistocene. No *Uvigerina* were observed at Site 974.

Biozonal Correlation

Correlation of the calcareous nannofossil and planktonic foraminiferal zonations is shown in Figure 25 (see also Table 7).

Paleoecology

Both the calcareous nannofossil and the planktonic foraminiferal assemblages are typical of open-ocean conditions. Benthic foraminifers indicate that, except for the assumed Messinian sequence at the bottom of the site, sediments at Site 974 were deposited in lower bathyal to abyssal depths. Occasional sedimentologic and faunal evidence exists for reworking from shallow-water environments. Supplemental samples for shipboard analyses generally avoided sampling in these intervals, but pervasive reworking of nannofossils was seen in the core-catcher samples.

The "Lago Mare" facies (Hsü, Montadert, et al., 1978) consists of sediments deposited in brackish environment, which are spread diffusely around the Mediterranean, probably from a Paratethys source.

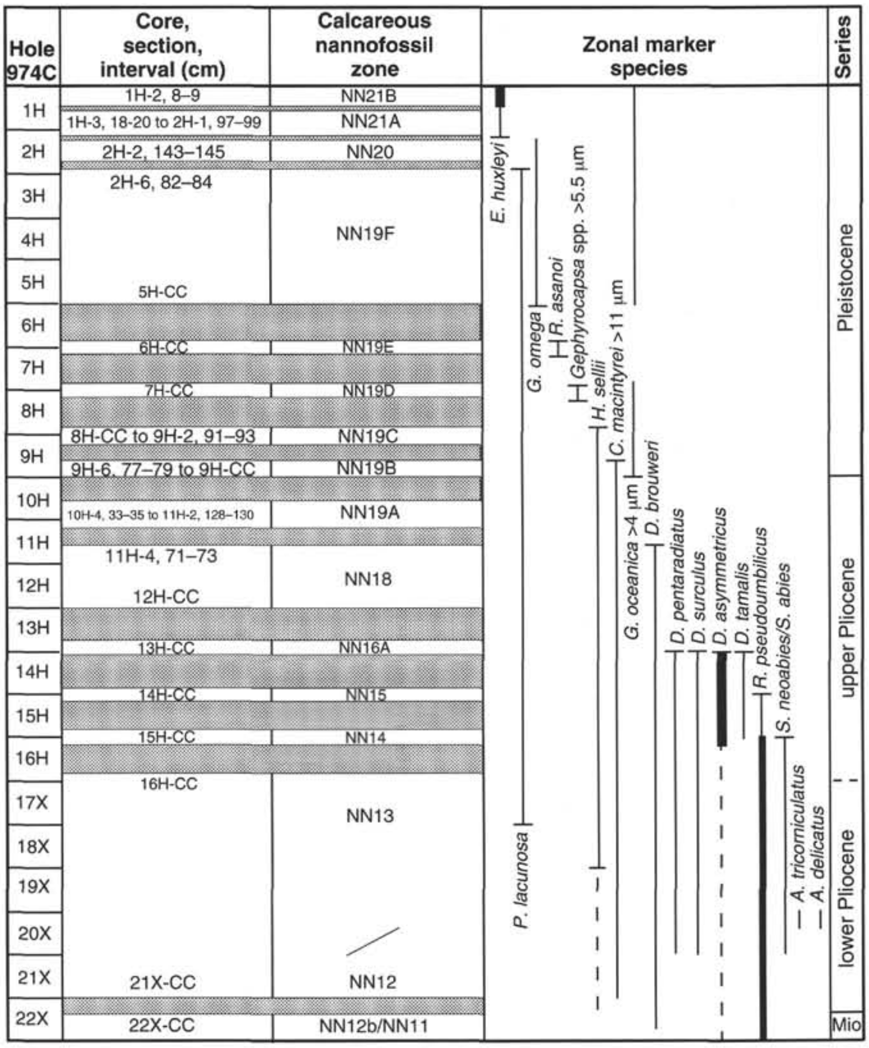

Figure 20. Calcareous nannofossil zonation of Hole 974C. Thick lines represent acme intervals. Dashed horizontal lines indicate boundaries defined between core-catcher samples. Dashed vertical lines indicate the irregular occurrence of *H. sellii* and *D. asymmetricus* in the Miocene. Missing zones or subzones do not imply hiatuses. The zones/subzones may be in sections not yet examined.

These deposits are well known to characterize the uppermost Messinian sequence of Mediterranean land sections. Usually they contain an *Ammonia-Cyprideis* fauna associated with lacustrine gastropods.

Sedimentation Rates

Figure 26 shows the sedimentation rates at Hole 974B. Age data (Table 7) used for construction of the plot are based on FO, LO, FCO, and LCO events of selected nannofossils and planktonic foraminifers (see Table 2 in the "Explanatory Notes" chapter, this volume). The average sedimentation rate at Site 974B was 55.1 m/m.y. for the Holocene–Pleistocene interval; 27.2 m/m.y. for the late Pliocene; and 52.2 m/m.y. for the early Pliocene. Sedimentation rates are uncorrected for compaction.

PALEOMAGNETISM

Sixty-two APC and XCB cores from Site 974 were measured with the cryogenic magnetometer, except for a few sections that were slightly deformed and could not pass through the magnetometer. Natural remanent magnetization (NRM) and alternating field (AF) demagnetized remanences were measured at 10-cm intervals. AF demagnetization was applied at 15 and/or 25 mT (peak field). We only measured demagnetized (25 mT) remanence of Cores 974B-12H through 22X and all cores from Hole 974C because of time constraints. Some discrete samples were measured with the spinner magnetometer for stepwise AF (up to 100 mT) or thermal demagnetizations (up to 120°C). Low-field susceptibility was also measured with a Kappabridge susceptometer to investigate magnetic fabric of some discrete samples. Cores 974B-3H to 17H were oriented using the Tensor tool (Table 8).

Remanent Magnetization

Intensities of NRM were strong (several tens mA/m) and well above the noise level of the cryogenic magnetometer throughout all cores. Remanent intensities decreased to about 10 mA/m after AF demagnetization at 25 mT (Fig. 27A).

Most of the inclinations show steep positive values before demagnetization. After AF demagnetization at 25 mT, negative inclinations were sporadically observed and the positive inclination values become shallow and are close to that of the present geomagnetic field at this site (+60°) (Fig. 27B). Declination, inclination, and intensity after AF demagnetization at 25 mT are shown for all holes in Figures 28–31. Even after the demagnetization at 25 mT, positive inclinations dominate throughout all holes of this site. In Hole 974C, between 60–150 mbsf, inclination shows quasi-periodic changes from

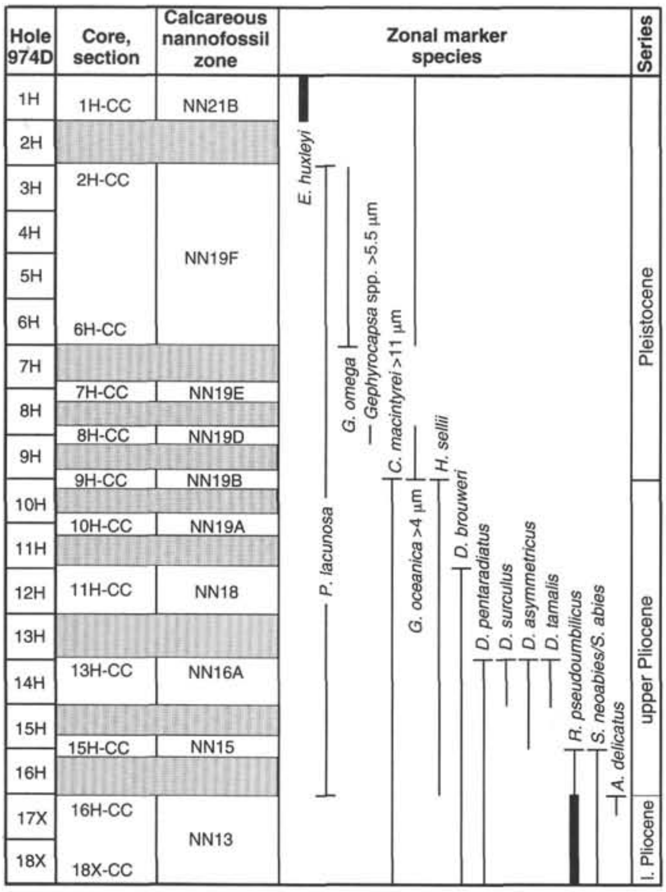

Figure 21. Calcareous nannofossil zonation of Hole 974D. Thick lines represent acme intervals. Missing zones or subzones do not imply hiatuses. The zones/subzones may be in sections not yet examined.

+80° to +30° (Fig. 30). These pervasive positive inclinations are caused by stable secondary overprinting throughout the site and make it difficult to establish a definitive magnetostratigraphy.

Steep positive inclinations can be attributed to drill-string overprinting as has been reported since Leg 152 (Shipboard Scientific Party, 1995a). Prior to Leg 152, steep negative overprinting was reported (Shipboard Scientific Party, 1992). We also found that the declination data are mostly concentrated around 0° (X-axis of core-coordinates; from the center of the core through the double line scribed on the working half of the core liner), particularly for the lower part of APC cores (below 50 mbsf; Figs. 29–31). In addition, we measured some of the working-half sections (974C-19X-4, 974D-2H-4, and 974D-4H-6) before they were sampled. The core-coordinate declinations are all clustered around 180°, that is, the direction of –X, as shown in Figure 32A. Zero or 180° declinations cannot be explained by mere chance. The declination is apparently symmetrical for archive and working halves; in other words, bulk magnetization of the archive and working halves are both perpendicular to the split core surface. Cores 974B-3H through 17H from Hole 974B were reoriented to geographic north using the Tensor tool. Reoriented declinations make tight clusters for data within each core, but they are variable between cores (Fig. 32B). We believe that the large scatter among the reoriented declinations also supports the presence of a spurious horizontal component of magnetization. Cores recovered by XCB (>160 mbsf) show clustered declinations around 20° for the archive half (Figs. 29, 30) or about 200° for the working half (Fig. 32A). Despite considerable XCB biscuiting and presumed variable rotation of biscuits, the data still has rather consistent declinations

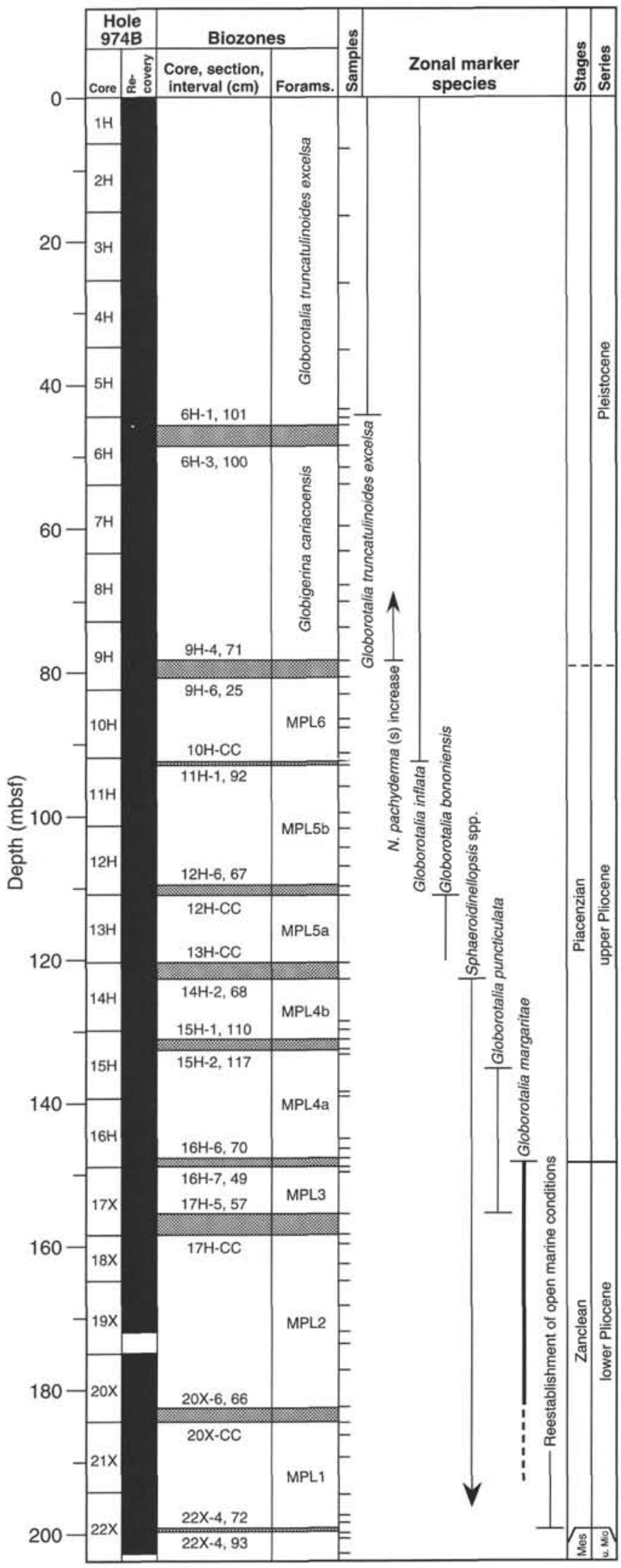

Figure 22. Planktonic foraminiferal zonation of Hole 974B. Dashed horizontal lines indicate boundaries defined between core-catcher samples. Gray zones represent intervals not sampled.

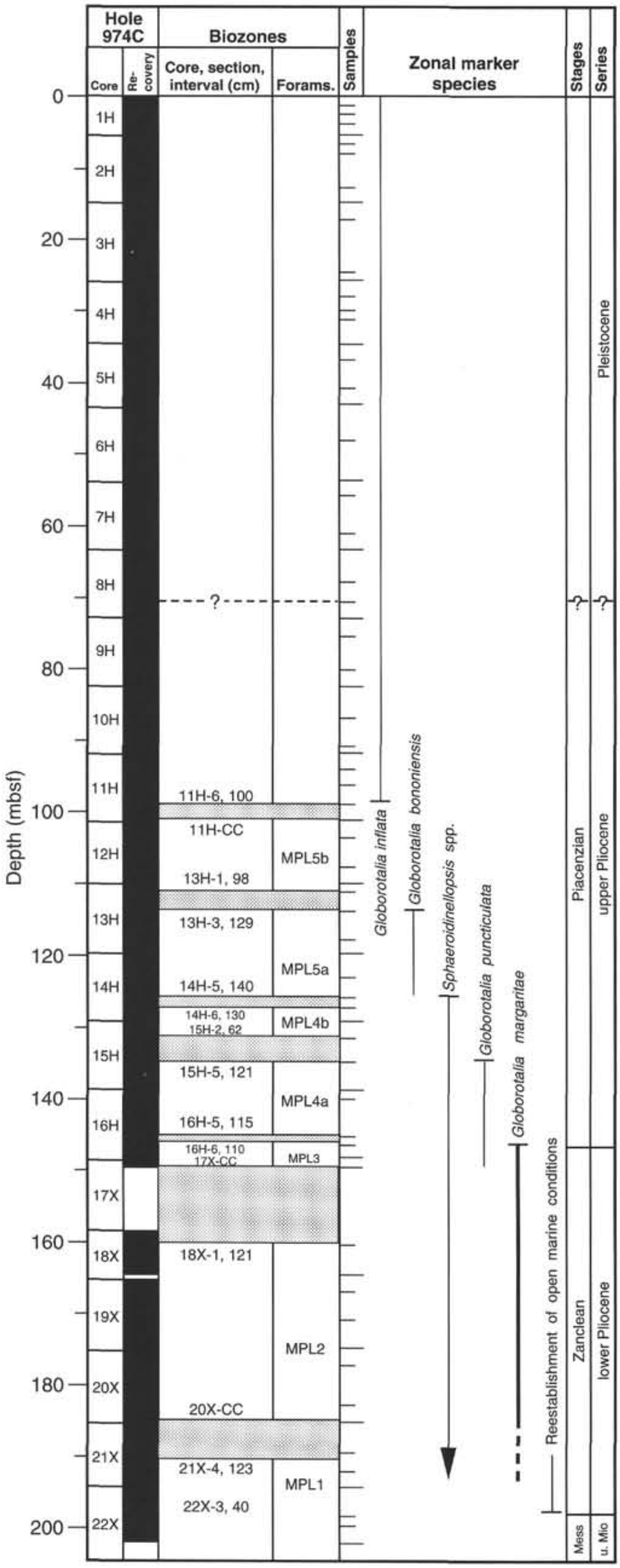

Figure 23. Planktonic foraminiferal zonation of Hole 974C. Dashed horizontal lines indicate boundaries defined between core-catcher samples. Gray zones represent intervals not sampled.

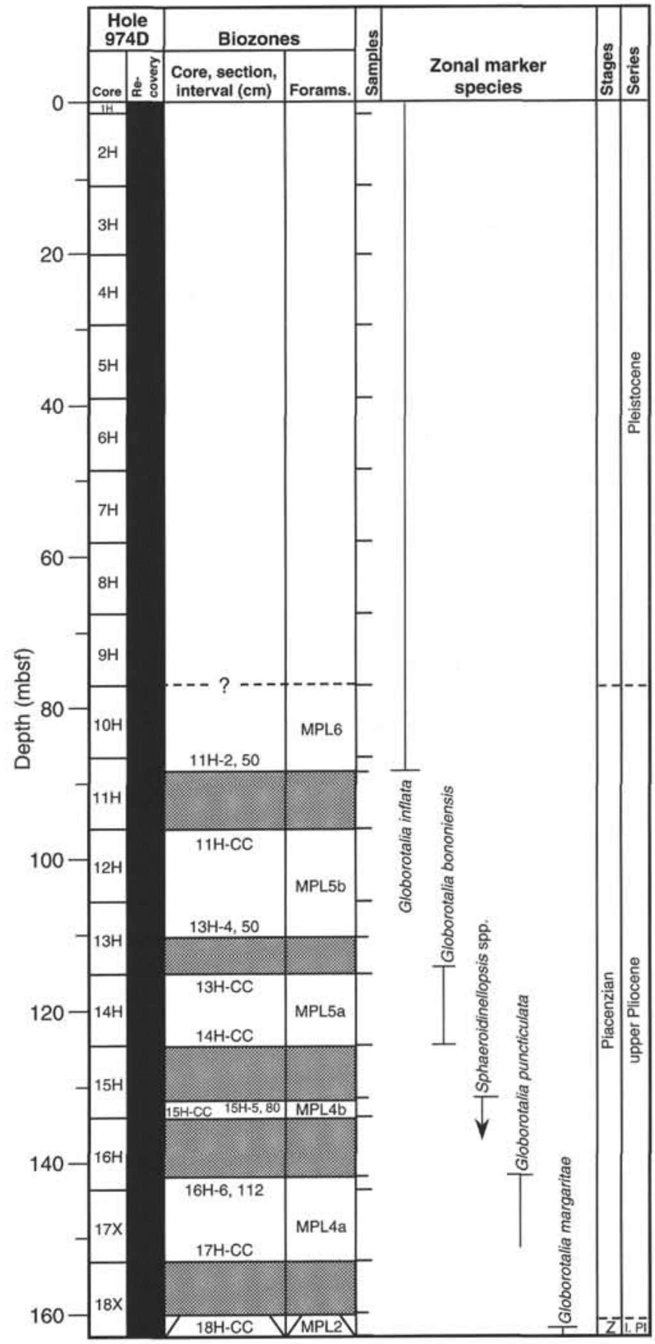

Figure 24. Planktonic foraminiferal zonation of Hole 974D.

that are rotated slightly clockwise (drilling direction) from 0° or from 180°.

The presence of spurious declinations prompted us to make additional measurements to understand this magnetization. In Figure 33A we show pass-through results of Section 974D-10H-1, which has declinations perfectly aligned with 0° before the demagnetization. An example of progressive AF demagnetization in this section is displayed as the Zijderveld diagram and indicates the spurious declination is not removed even after application of 25 mT alternating field (Fig. 33A). Discrete samples collected from the working halves were progressively demagnetized with AF and/or thermal methods (Fig. 33B). The large X component of NRM was not removed with AF de-

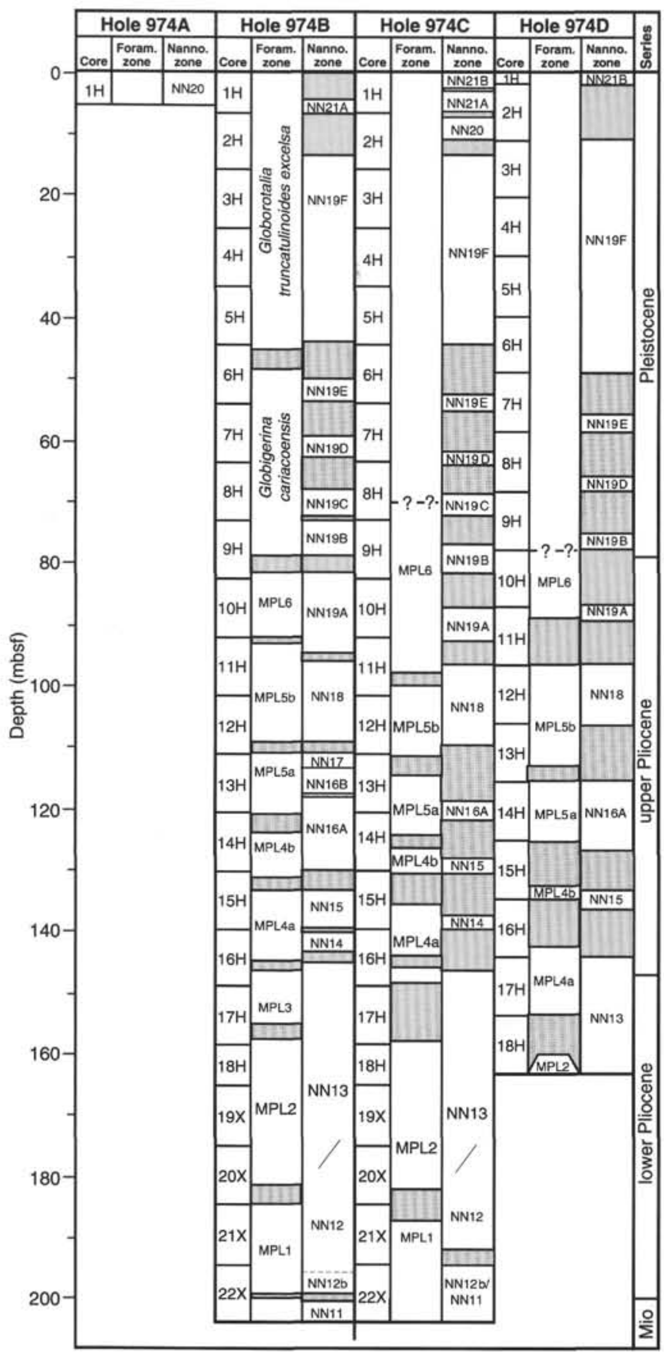

Figure 25. Summary of nannofossil and foraminiferal zonations of Holes 974A–974D.

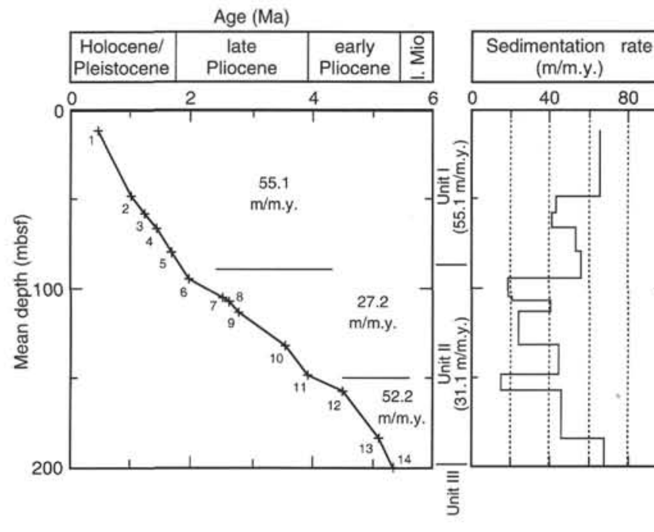

Figure 26. Age vs. depth plot and sedimentation rates for Hole 974B.

Table 7. Age of biostratigraphic events and depth of their occurrence at Site 974.

		Biostratigraphic events	Age (Ma)	Depth (mbsf) Top	Bottom	Mean
1	FO	*P. lacunosa*	0.46	6.78	16.44	11.61
2	FO	*G. omega* >4.0 µm	1.02	44.88	51.6	48.24
3	LO	*Gephyrocapsa* spp. >5.5 µm	1.24	54.4	60.99	57.69
4	FO	*Gephyrocapsa* spp. >5.5 µm	1.44	63.96	67.99	65.97
5	FO	*G. oceanica* >4.0 µm	1.75	78.11	80.65	79.38
6	FO	*G. inflata*	2.13	92.28	92.92	92.60
7	LO	*D. pentaradiatus*	2.52	103.74	105.80	104.77
8	LO	*D. surculus*	2.63	106.11	107.91	107.01
9	LO	*D. tamalis*	2.78	112.46	113.88	113.07
10	LO	*G. puncticulata*	3.57	131.10	132.67	131.88
11	LCO	*G. margaritae*	3.94	147.72	149.01	148.36
12	FO	*G. puncticulata*	4.52	155.57	158.74	157.15
13	FCO	*G. margaritae*	5.1	183.06	184.70	183.88
14		Reestablishment of open-marine conditions	5.33	199.32	199.53	199.42

Notes: FO = first occurrence, LO = last occurrence, LCO = last common occurrence, FCO = first common occurrence.

Table 8. Azimuthal orientation of APC cores from Hole 974B using the Tensor tool data.

Core	Magnetic toolface (MTF) (°)
161-974B-	
3H	246
4H	166
5H	118
6H	318
7H	249
8H	238
9H	327
10H	234
11H	54
12H	109
13H	247
14H	327
15H	183
16H	304
17H	164

Notes: Cores 974B-3H to 17H were oriented. The orientation parameter (MFT) is an angle between true north and X-axis of the core-coordinate.

magnetization up to 60 mT, and the magnetization became too weak to be measured confidently after demagnetization higher than 70 mT. We also thermally demagnetized two discrete samples from room temperature up to 120°C (Fig. 33B) without observing a significant change in the intensity or direction of NRM.

A similar type of magnetization was reported during Leg 154 (Shipboard Scientific Party, 1995b) and also during Leg 159 (Shipboard Scientific Party, 1996). Paleomagnetists of Leg 154 demonstrated that overprinting is a radially concentrated horizontal magnetization and called it "pervasive radial remagnetization" (PRR). They tested the laboratory equipment and drilling assemblies

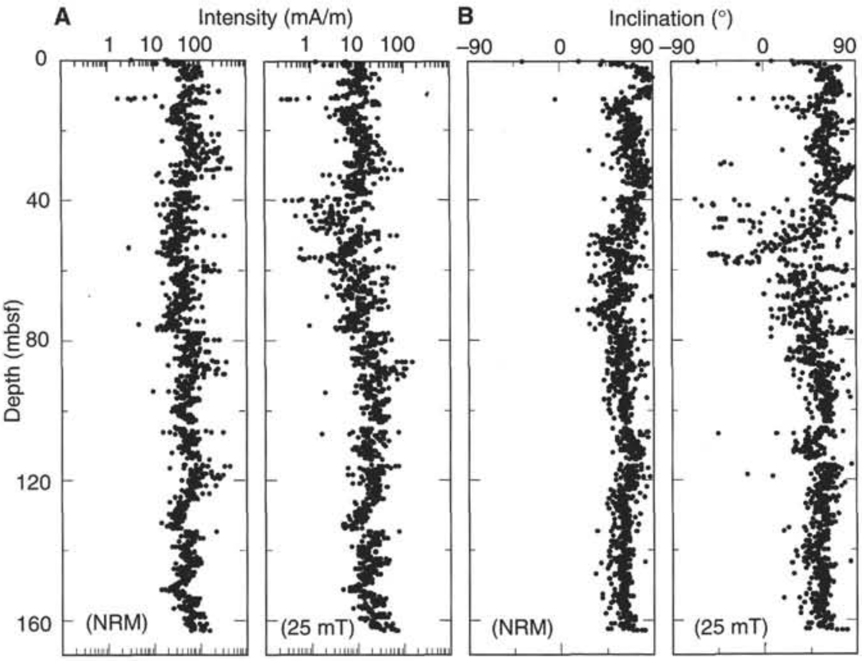

Figure 27. Comparison between NRM and AF demagnetized records from Hole 974D. **A** = intensity, **B** = inclination.

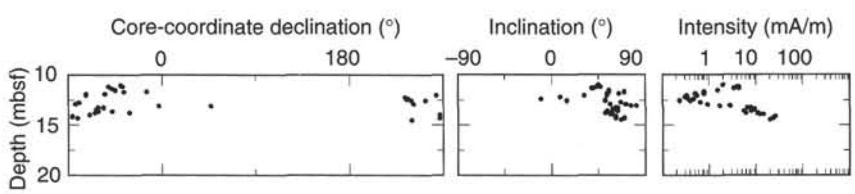

Figure 28. Pass-through remanent magnetization measurements of archive halves from Hole 974A after AF demagnetization at 25 mT. Declination (relative to core-coordinates), inclination, and intensity are plotted against depth (mbsf). Data points are at 10 cm intervals.

in various ways and finally concluded that the cutting shoe may have contributed to PRR, although a physical process to explain this has not yet been made clear. As shown at this site, the spurious magnetization has pronounced geometrical symmetry, perpendicular to the axis of the core. The physical process to achieve the radial overprinting cannot be readily understood, but it is one of the most plausible phenomenological explanations for the observed 0° declinations.

Magnetostratigraphy

Although the inclination record is poorly defined at this site, we observe three horizons where negative inclinations are found in all holes. Scattered but negative inclinations can be identified in the upper half of APC cores at 10–15, 20–30, and 40–80 mbsf (Fig. 34). We believe that negative inclination indicates partially successful removal of the secondary overprinting by the AF demagnetization; these may be reversed polarity intervals. According to the biostratigraphic age estimation (see "Biostratigraphy" section, this chapter), the Brunhes/Matuyama chron boundary (C1n/C1r = 0.78 Ma; Cande and Kent, 1995) is placed at about 25 mbsf. This depth coincides with the second negative inclination zone at Holes 974B, 974C, and 974D (Fig. 34). The horizon with dominant negative inclinations, 40–80 mbsf, is possibly Chron C1r.2r (1.07–1.77 Ma; Cande and Kent, 1995) based on the biostratigraphic age estimation.

Site 974 is located about 300 m from Site 652 (Leg 107, See "Background and Objectives" sections, this chapter). The magnetostratigraphy at Site 652 was not fully documented because of poor recovery of the sediments by RCB coring and hard overprinting (Channell et al., 1990). Remanence directions of the discrete samples were mainly determined after thermal demagnetization up to 300°C. At Site 652, the Olduvai subchron (C2n) was placed at 90–94 mbsf, which is close to the base of the third negative inclination zone at Site 974 (about 80 mbsf).

Negative inclinations were observed at 10–14 mbsf in all holes of Site 974 (Fig. 34). Biostratigraphically, the age of the horizon is estimated to be about 100 ka and it may be the Blake geomagnetic excursion (Champion et al., 1988). However, it is difficult to correlate the observed negative inclination horizon with the Blake excursion at this moment. Possible polarity excursions were also proposed at the high sedimentation rate Site 650 for oxygen isotope stages 2 and 5 (Channell and Torii, 1990).

Magnetic Fabric

We sampled 15 discrete samples from the least disturbed part (center) of the working halves of Cores 974B-2H (4 samples) and 974B-16H (11 samples). Core 974B-16H was oriented with the Tensor tool to give the true azimuth of the core (304°; Table 8).

The AMS data are summarized in Figure 35. Only the magnetic foliation plane (K_1/K_2) is well defined (F >1.01) and, therefore, so is the minimum axis K_3. The maximum axis of susceptibility K_1, that usually marks a sedimentary or tectonic lineation, is poorly defined for Core 974B-2H (L = 1.003 ± 0.002; Fig. 35A) and better defined for Core 974B-16H (L = 1.012 ± 0.008; Fig. 35B). The best method to process AMS data uses the tensorial mean (Jelinek, 1978), which is not available on the ship. We decided to plot K_1 with respect to the confidence angle E12 (i.e., the half confidence angle within the plane of K_1 and K_2; Fig. 35A, B). This shows a significant grouping of K_1 that is oriented northeast to southwest (Fig. 35B). This probably represents a sedimentary or tectonic lineation. However, further mea-

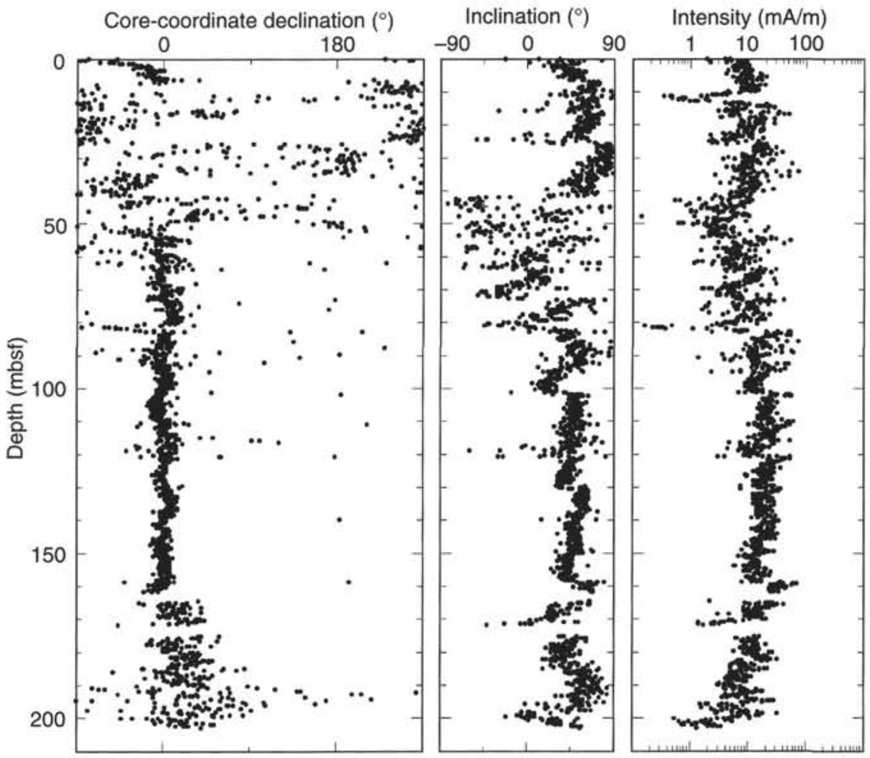

Figure 29. Pass-through measurements of archive halves from Hole 974B after AF demagnetization at 25 mT. See Figure 28 caption for further explanation.

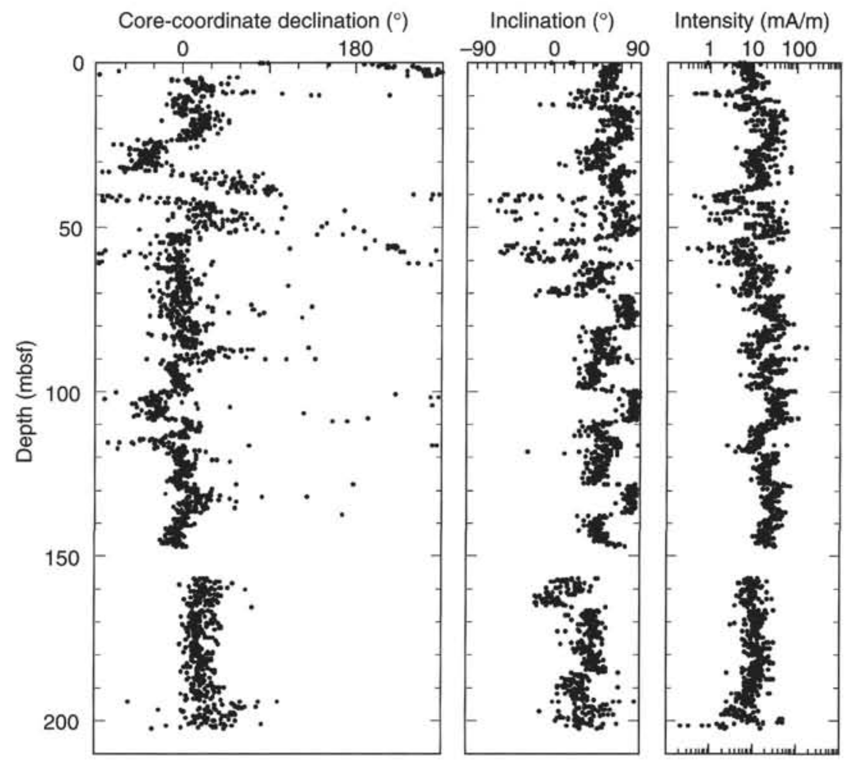

Figure 30. Pass-through measurements of archive halves from Hole 974C after AF demagnetization at 25 mT. See Figure 28 caption for further explanation.

surements are needed to see whether this magnetic lineation is significant. Effects of diagenesis and compaction cannot be determined from the AMS parameters (Fig. 35C). The foliation parameter (F) ranges within the same values in both cores, but the lineation parameter (L) is greater in Core 974B-16H. This enhancement could be attributable to either tectonic deformation or variation in magnetic carriers. From our preliminary measurements, magnetic foliation is well defined, indicating that the magnetic fabric is of sedimentary origin and has not been significantly disturbed.

COMPOSITE DEPTHS

High-resolution (2–10-cm-scale) data were collected on the multisensor track (MST) and with a hand-held spectrophotometer on cores recovered from all holes of Site 974. Three principal variables (GRAPE density, magnetic susceptibility, and 550-nm-wavelength color reflectance) were used to construct a composite depth section from Holes 974B, 974C, and 974D. Distinctive features were correlated between cores from each hole and depth-shifted to a common

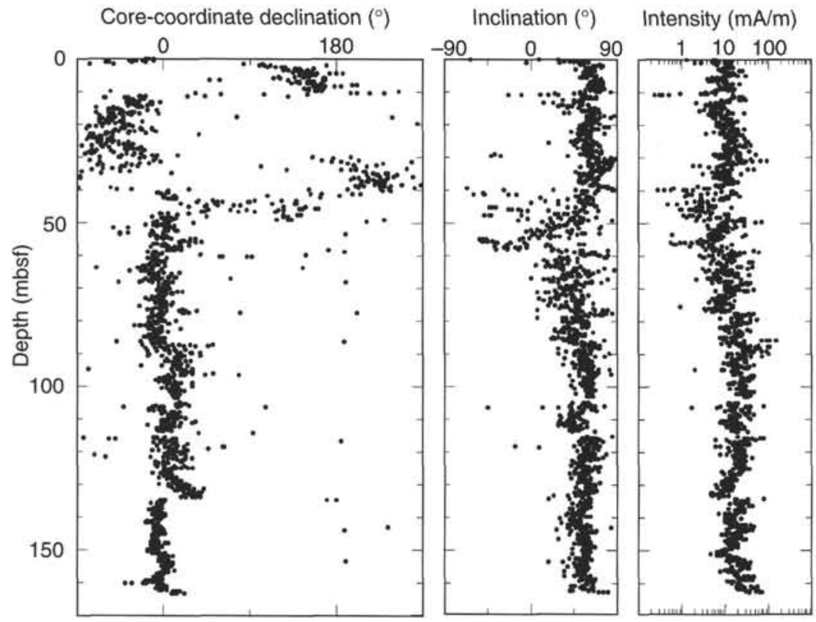

Figure 31. Pass-through measurements of archive halves from Hole 974D after AF demagnetization at 25 mT. See caption for Figure 28 for further explanation.

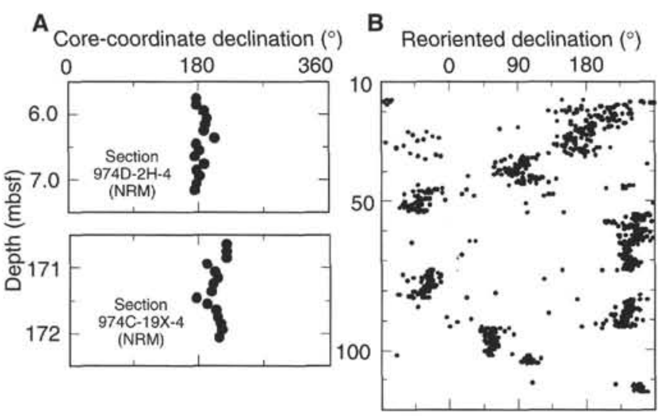

Figure 32. **A.** Declination of working half of APC (above) and XCB (below) sections before demagnetization. **B.** NRM declination reoriented using the Tensor tool data (Table 8) from Cores 974B-3H through 12H.

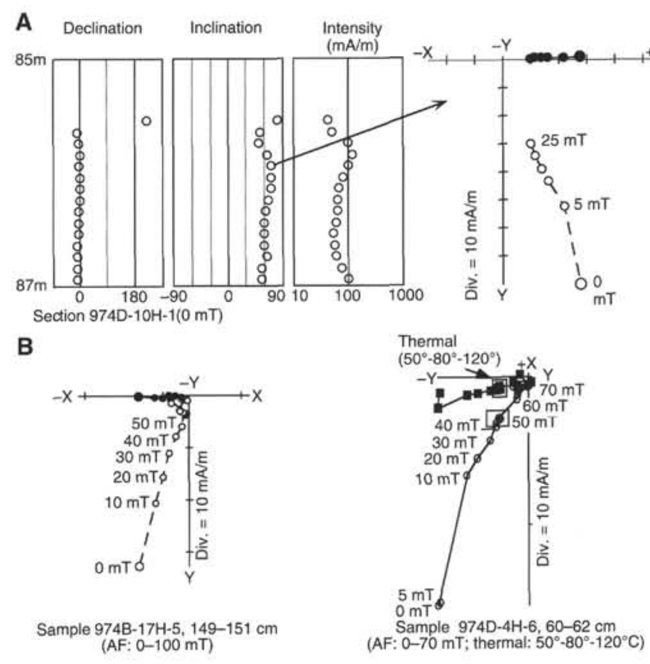

Figure 33. Typical examples of progressive AF demagnetization showing apparent stability of the remanent magnetization for Site 974. **A.** Declination, inclination, and intensity of Section 974D-10H-1 (archive) after AF demagnetization at 25 mT. The progressive change in magnetization is displayed by the Zijderveld diagram. Open and closed circles indicate vertical and horizontal remanent vector-end points, respectively. Remanent magnetization of 0° declination is highly stable over AF demagnetizations up to 25 mT. **B.** Typical examples of progressive AF and thermal demagnetization of discrete samples.

depth scale (meters composite depth = mcd) so that overlapped cores from different holes would produce a single composite section. The offsets for each core that were used for alignment are listed in Table 9, which gives standard ODP meters below seafloor depths (mbsf), offset in meters, and the composite depth for each core (mcd). Shifted and aligned core data are shown in Figure 36.

The composite (or "spliced") section seeks to provide a complete stratigraphic record utilizing overlapping intervals of cores from the different holes. The composite section is described in Table 10. Splices from Table 10 are indicated by arrows in Figure 36. The composite section is approximately 6.5 m longer than the cored sections because expanded parts of holes were chosen when pairs of correlated features from different holes were found to be separated by different lengths of core.

Correlation between cores was consistent between the seafloor and approximately 75 mbsf. When features were aligned for the composite depth section, structural complications between 75 mbsf and 95 mbsf (Figure 37) forced overlaps of Cores 974D-9H and 10H, Cores 974C-9H and 10H, and Cores 974B-9H and 10H (Table 11). Cores from Hole 974D showed a 3.4-m repeated section, verified by the multiple occurrence of identified organic-rich layers T30, T31, and T32 (Table 5; Fig. 37). In Hole 974C, it is believed that organic-rich layer T29 is a repeat of T28, implying a 2.2-m-thick repeated section. The 1.5-m-thick sand layer present near the base of Core 974B-9H (Fig. 37, 80.5–82.0 mbsf) is not seen in recovery from other holes, although the stratigraphic interval was overlapped by Cores 974C-10H and 974D-10H. It has been excluded from the composite depth section.

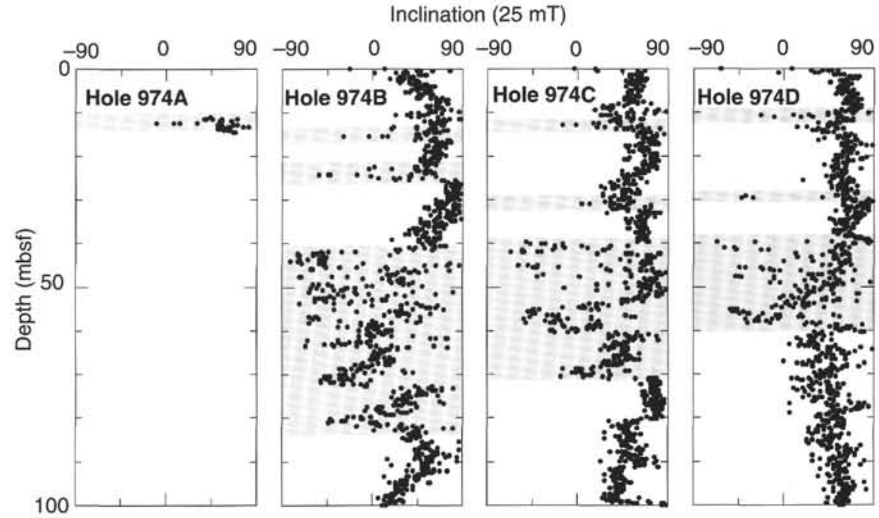

Figure 34. Correlation of inclination between Holes 974A to 974D after AF demagnetization at 25 mT. Negative inclinations are found at three shaded horizons throughout all holes, at 10–15, 20–30, and 40–80 mbsf.

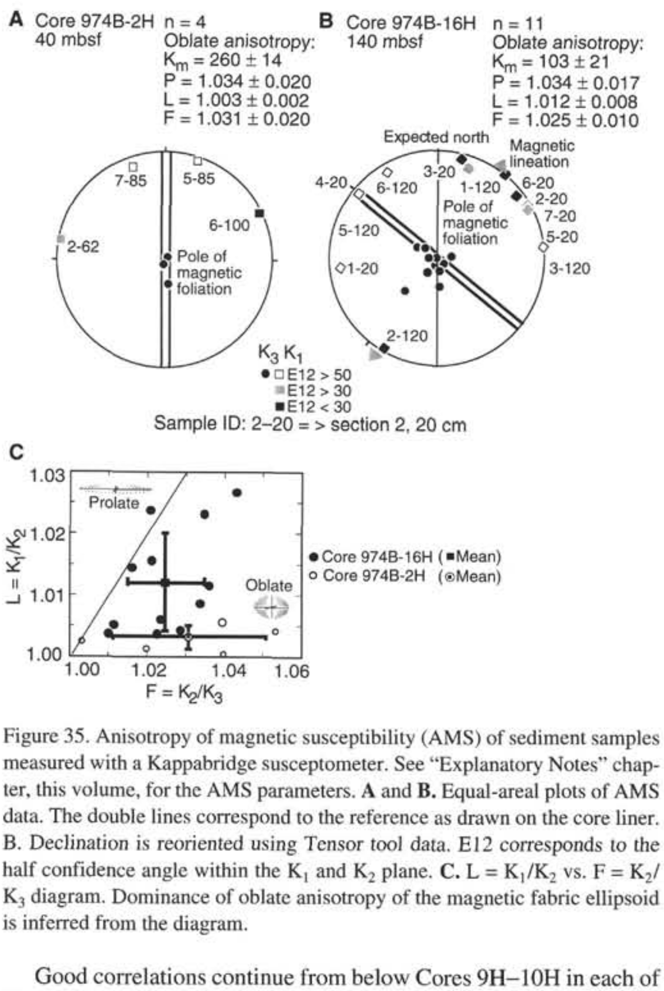

Figure 35. Anisotropy of magnetic susceptibility (AMS) of sediment samples measured with a Kappabridge susceptometer. See "Explanatory Notes" chapter, this volume, for the AMS parameters. **A** and **B.** Equal-areal plots of AMS data. The double lines correspond to the reference as drawn on the core liner. B. Declination is reoriented using Tensor tool data. E12 corresponds to the half confidence angle within the K_1 and K_2 plane. **C.** $L = K_1/K_2$ vs. $F = K_2/K_3$ diagram. Dominance of oblate anisotropy of the magnetic fabric ellipsoid is inferred from the diagram.

Good correlations continue from below Cores 9H–10H in each of Holes 974B, 974C, and 974D to the deepest penetration of APC coring, approximately 150–160 mbsf. The bottom of Core 974D-18H marks the deepest point of what can be considered a continuous composite section. Below this level there are only small overlaps between cores from Holes 974B and 974C. While there are still very good correlations between core data from this interval, there may be missing intervals between the tops and bottoms of those cores, particularly at the boundaries between Cores 974C-18X and 974B-19X, 974C-19X and 974B-20X, and 974C-20X and 974B-21X.

STRUCTURAL GEOLOGY

The Pleistocene and Pliocene sediments cored at Site 974 are unconsolidated or poorly consolidated muds and sands. As a result, much of the section shows drilling-induced deformation, including zones about 1 cm wide of downward drag on each side of the APC cores, and separation of the XCB cores into rotated sections 1–15 cm long ("biscuits").

Features of probable primary significance include dip changes, microfaults, and slump structures. Because the sediment was so soft, it was rarely possible to remove the core or cut it to determine the true inclination of structures: most measurements had to be taken as apparent dips on the cut face of the core.

Dips of up to about 15° in coherent sections of the sequence may reflect tectonic tilting. Seismic line ST01 shows a gradual increase in dip up to about 3°W in the lower part of the hole, due to a rollover anticline in the hanging wall of the listric normal fault (Fig. 3). The dip at the base of the cored interval (200 mbsf) is horizontal, however, and in view of the observed slumping, it may be that some or all of the local dips reflect sliding of the poorly consolidated sequence. Nevertheless, slumping could have been favored by westward tilting during sedimentation. The fault bounding the basin to the west is in fact a growth fault as indicated by the increase in thickness of the late Miocene-to-Pleistocene sequences towards the fault.

Microfaults with normal-sense displacements of 1 cm or less are abundant from about 30 mbsf downwards (Fig. 38). Both east- and west-dipping sets (in core coordinates) occur, commonly as conjugate sets, with dips mainly in the range 45°–60°. The microfaults are visible in the mud as zones with a slightly higher water content and (possibly) an internal fabric (Fig. 39). Numerous such fractures without determinable offsets are visible. They suggest that the section has undergone continuing slight extensional deformation during deposition, although we cannot eliminate the possibility that these fractures were induced at some point during the drilling process.

From 90.5 to 109.5 mbsf in Hole 974B the sediment is strongly disturbed by soft sediment deformation, including slump folds on scales from 5 cm to 2 m (Figs. 40, 41), zones of inclined but coherent bedding bounded above and below by discordances, disrupted and contorted bedding (Fig. 42), and layers of largely homogenized sediment. The latter are characterized by an absence of bedding lamina-

Table 9. Composite depth table for Holes 974A, 974B, 974C, and 974D.

Core	Depth (mbsf)	Offset (m)	Depth (mcd)
161-974A-			
1H	5.00	0.66	5.66
161-974B-			
1H	0.00	0.00	0.00
2H	6.50	1.10	7.60
3H	16.00	1.38	17.38
4H	25.50	1.58	27.08
5H	35.00	2.50	37.50
6H	44.50	3.34	47.84
7H	54.00	4.53	58.53
8H	63.50	5.28	68.78
9H	73.00	5.90	78.90
10H	82.50	4.44	86.94
11H	92.00	3.90	95.90
12H	101.50	3.90*	105.40
13H	111.00	3.95	114.95
14H	120.50	4.38	124.88
15H	130.00	4.38*	134.38
16H	139.50	3.80	143.30
17H	149.00	4.12	153.12
18H	158.50	5.07	163.57
19X	165.00	4.97	169.97
20X	174.90	4.17	179.07
21X	184.50	7.14	191.64
22X	194.10	6.50	200.60
161-974C-			
1H	0.00	1.90	1.90
2H	4.30	3.04	7.34
3H	13.80	4.60	18.40
4H	23.30	4.28	27.58
5H	32.80	5.10	37.90
6H	42.30	5.48	47.78
7H	51.80	5.44	57.24
8H	61.30	5.84	67.14
9H	70.80	6.00	76.80
10H	80.30	3.85	84.15
11H	89.80	4.19	93.99
12H	99.30	4.28	103.58
13H	108.80	3.64	112.44
14H	118.30	4.00	122.30
15H	127.80	4.48	132.28
16H	137.30	4.29	141.59
17X	146.80	No recovery	146.80
18X	156.40	5.35	161.75
19X	166.10	5.35*	171.45
20X	175.70	4.21	179.91
21X	185.30	4.21*	189.51
22X	194.90	4.21*	199.11
161-974D-			
1H	0.00	0.00	0.00
2H	1.50	1.65	3.15
3H	11.00	3.36	14.36
4H	20.50	4.05	24.55
5H	30.00	4.66	34.66
6H	39.50	5.12	44.62
7H	49.00	5.63	54.63
8H	58.50	6.07	64.57
9H	68.00	6.46	74.46
10H	77.50	3.81	81.31
11H	87.00	4.01	91.01
12H	96.50	2.95	99.45
13H	106.00	3.08	109.08
14H	115.50	3.57	119.07
15H	125.00	3.90	128.90
16H	134.50	4.22	138.72
17H	144.00	4.17	148.17
18H	153.50	4.99	158.49

Notes: * = offset carried from core above due to poor overlap. Adding offset to meters below seafloor (mbsf) within each core will produce meters composite depth (mcd).

tions and by dispersed grains of ash, which could be the result of bioturbation, slumping, or both. This zone of more or less continuous soft-sediment deformation is overlain and underlain by coherent horizontally bedded sediment, suggesting that it may constitute a 19-m-thick slump sheet. This raises the possibility that there may be some stratigraphic duplication or excision in the section, as a result of sediment sliding (see "Lithostratigraphy" section, this chapter). In Hole 974C this section of slump folding and disturbed bedding is also clearly identifiable and lies between 90 and 109 mbsf. In Hole 974D the disturbed zone appears to be thicker, but less well defined. At 70.5 to 82.5 mbsf there is a zone of reverse faults (Figs. 9, 37, 43), the largest of which repeats 3.42 m of section (representing a displacement of about 7 m). In view of the tectonic setting, and the evidence for normal faulting in all the cores, this reverse faulting is most likely to be related to slumping. From 88 to ~106 m the bedding is more or less continuous disturbed, with anomalously steep dips and visible slump folds.

The slumping and tectonic deformation at this site suggest that the area was tectonically active during the Pliocene and Pleistocene.

ORGANIC GEOCHEMISTRY

Calcium carbonate and organic carbon concentrations were measured on samples obtained regularly from Holes 974A, 974B, and 974C and from selected intervals in Hole 974D. Organic matter atomic C/N ratios and Rock-Eval analyses were employed to determine the type of organic matter contained in the sediments. Analyses of extractable methyl alkenones yielded estimates of sea-surface paleotemperatures, and GHM pyrolyses provided further information about organic matter character. Routine monitoring of headspace gas content was done for drilling safety.

Inorganic and Organic Carbon Concentrations

Concentrations of carbonate carbon vary from essentially zero to 8.3% at Site 974 (Table 12). These carbonate carbon concentrations are equivalent to 0% to 69% sedimentary $CaCO_3$, assuming that all of the carbonate is present as pure calcite. The range in carbonate content reflects a combination of generally low biological productivity, dilution by varying amounts of non-carbonate hemipelagic sedimentary components, and post-depositional carbonate dissolution driven by oxidation of organic carbon in sapropels.

Twenty-four sapropels, defined in this section as containing more than 1% TOC (Total Organic Carbon; note that this definition of a sapropel is different from that of an organic-rich layer in the "Lithostratigraphy" section, this chapter), occur in Hole 974B (Fig. 44). Many of the same layers could be recognized in Hole 974C (Table 12). Sample 974B-7H-1, 117–118 cm (55.18 mbsf), contains the maximum of 6.3% TOC. Partial post-depositional oxidation of the organic matter content of the sapropels is suggested by their $CaCO_3$ concentrations, which range between 2% and 43% and hence are generally lower than those of background sediments. This factor may have also been involved in lowering the $CaCO_3$ concentrations of lithostratigraphic Unit I relative to deeper units in which sapropels are absent (Fig. 44). Another possible factor is diminished biogenic carbonate production during times of sapropel deposition. Similarly, dilution of carbonate contents by clastic hemipelagic sediment components is possible, but this process would also dilute organic matter content and thereby diminish sapropel development.

Organic Matter Source Characterization

Organic C/N ratios were calculated for Site 974 samples using TOC and total nitrogen concentrations to help identify the origin of their organic matter. Algal organic matter generally has atomic C/N ratios between 5 and 10, whereas organic matter derived from land plants has values between 20 and 100 (e.g., Emerson and Hedges, 1988; Meyers, 1994). Site 974 C/N ratios are variable (Table 12). The C/N values of some samples low in TOC are very low (<5). These values are probably an artifact of the low carbon content combined with the tendency of clay minerals to absorb ammonium ions generated during degradation of organic matter (Müller, 1977). The C/N ratios in samples especially low in organic carbon consequently are not accurate indicators of organic matter source.

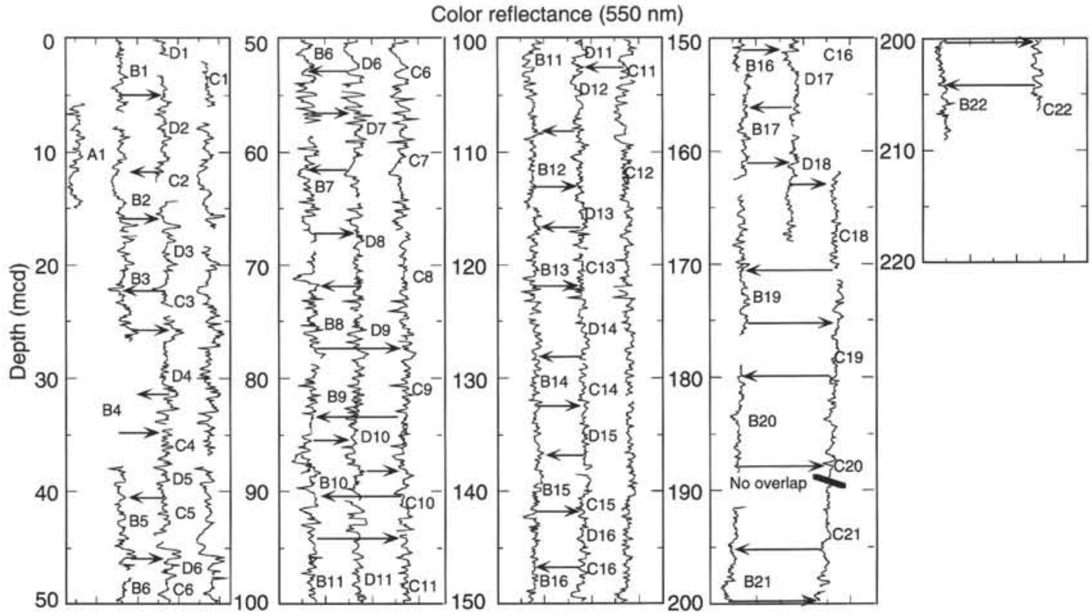

Figure 36. Color reflectance data (550 nm) for each hole plotted vs. mcd with tie lines used to construct composite depth section. Shifts in core depths from mbsf to mcd were accomplished using color as well as magnetic susceptibility and GRAPE data. Overlapping intervals between Cores 974B-9H and 10H, Cores 974C-9H and 10H, and Cores 974D-9H and 10H are the result of faulting, which repeated sections of each sediment column.

The C/N ratios of sapropels average 16.5, which is a value intermediate between unaltered algal organic matter and fresh land-plant material. Because diagenesis rarely depresses land-plant C/N ratios to values as low as those found in the sapropels, it is likely that these organic-carbon–rich sediments contain algal material that has partially been degraded during settling to the seafloor. Preferential loss of nitrogen-rich, proteinaceous matter can elevate the C/N ratios of algal organic matter by this process.

The results of Rock-Eval analyses of sapropels selected from Hole 974B show that their organic matter content is dominated by partially oxidized Type II algal material (Fig. 45). Well-preserved Type II organic matter has high HI values (Espitalié et al., 1977). In general, Hole 974B sediments that have higher TOC concentrations also have higher HI values (Fig. 46), which is a pattern also found in sapropels in the eastern Mediterranean (Emeis, Robertson, Richter, et al., in press). This relationship is consistent with preservation being important in elevating the organic matter content of Mediterranean sapropels (e.g., Cheddadi and Rossignol-Strick, 1995). T_{max} values are relatively low, showing that organic matter is thermally immature with respect to petroleum generation (Espitalié et al, 1977). A well-developed pattern of increasing T_{max} values with depth is nonetheless present (Table 13). Because neither burial depth nor sediment age increases substantially over this depth range, the increase in thermal maturity must be a consequence of the elevated geothermal heat flow at this location (see "In Situ Temperature" section, this chapter).

Alkenone Paleotemperature Estimates

Samples containing at least 1% TOC were selected from Hole 974B for extraction and analysis of C_{37} alkenone biomarkers and calculation of sea-surface paleotemperatures. The calculated paleotemperatures (Table 14) must be considered preliminary because of limitations of shipboard analytical capabilities. Moreover, $U^{k'}_{37}$ values are converted to sea-surface temperatures by comparison to *Emiliania huxleyi,* which has been extant for ~250,000 yr; paleotemperatures calculated for sediments older than this must be considered relative rather than absolute.

Sea-surface paleotemperatures have fluctuated over a 10°C range in the Tyrrhenian Sea since the late Pliocene (Fig. 47). Furthermore, a change to cooler temperatures occurred at approximately the Pliocene/Pleistocene boundary. A similar record of fluctuating temperatures and a shift to cooler conditions has been reported from the eastern Mediterranean (Emeis, Robertson, Richter, et al., 1996). However, the paleotemperatures calculated for the Tyrrhenian Sea are ~5°C cooler than those estimated at times of sapropel deposition in the eastern areas. Part of this temperature difference appears to be real.

Headspace Gases

Concentrations of headspace methane were low throughout Site 974. A single sample, 974B-1H-4, 0–5 cm (20.55 mbsf), exceeded the background concentration of ~4 ppm, yet it contained only 17 ppm. The strongly reducing conditions needed for methanogenesis evidently have never been achieved in the sediments at Site 974, and sulfate concentrations remain high throughout the recovered sediments (see "Inorganic Geochemistry" section, this chapter). As noted by Claypool and Kvenvolden (1983), the presence of interstitial sulfate inhibits methanogenesis in marine sediments.

INORGANIC GEOCHEMISTRY

Interstitial water samples were obtained at Site 974 from 4.50 mbsf to 179.40 mbsf using the standard ODP titanium/stainless steel squeezer (Manheim and Sayles, 1974) with teflon disks (see "Explanatory Notes" chapter, this volume). The interstitial waters were analyzed for salinity, alkalinity, chloride, sulfate, lithium, potassium, sodium, calcium, magnesium, strontium, ammonium, silica, and phosphate by methods described in the "Explanatory Notes" chapter, this volume.

The interstitial water profiles are dominated by two main patterns: a steady increase with depth or a steady decrease with depth (Table 15; Figs. 48–51). Salinity, chlorinity, calcium, strontium, ammoni-

Table 10. Splice table for Site 974.

Hole, core, section, interval (cm)	Depth (mbsf)	Depth (mcd)		Hole, core, section, interval (cm)	Depth (mbsf)	Depth (mcd)
161-974				161-974		
B-1H-4, 52	5.02	5.02	tie to	D-2H-2, 40	3.40	5.05
D-2H-6, 139	10.09	11.74	tie to	B-2H-3, 115	10.65	11.75
B-2H-6, 79	14.79	15.89	tie to	D-3H-2, 4	12.54	15.90
D-3H-6, 43	18.93	22.29	tie to	B-3H-4, 40	20.90	22.28
B-3H-6, 85	24.35	25.73	tie to	D-4H-1, 118	21.68	25.73
D-4H-5, 112	27.62	31.67	tie to	B-4H-4, 10	30.10	31.68
B-4H-6, 67	33.67	35.25	tie to	D-5H-1, 58	30.58	35.24
D-5H-5, 7	36.07	40.73	tie to	B-5H-3, 22	38.22	40.72
B-5H-6, 103	43.53	46.03	tie to	D-6H-1, 139	40.89	46.01
D-6H-6, 61	47.61	52.73	tie to	B-6H-4, 40	49.40	52.74
B-6H-6, 127	53.27	56.61	tie to	D-7H-2, 49	50.99	56.62
D-7H-5, 91	55.91	61.54	tie to	B-7H-3, 31	57.02	61.55
B-7H-7, 10	62.81	67.34	tie to	D-8H-2, 127	61.27	67.34
D-8H-5, 130	65.80	71.87	tie to	B-8H-3, 10	66.60	71.88
B-8H-6, 142	72.32	77.60	tie to	C-9H-1, 79	71.59	77.59
C-9H-5, 73	77.53	83.53	tie to	B-9H-4, 22	77.62	83.52
B-9H-5, 76	79.66	85.56	tie to	D-10H-3, 124	81.74	85.55
D-10H-5, 103	84.53	88.34	tie to	C-10H-3, 139	84.49	88.34
C-10H-5, 79	86.89	90.74	tie to	B-10H-3, 109	86.29	90.73
B-10H-6, 25	89.95	94.39	tie to	C-11H-1, 40	90.20	94.39
C-11H-6, 100	98.30	102.49	tie to	D-12H-3, 4	99.54	102.49
D-12H-7, 16	105.16	108.11	tie to	B-12H-2, 121	104.21	108.11
B-12H-6, 10	109.10	113.00	tie to	D-13H-3, 91	109.91	112.99
D-13H-6, 10	113.60	116.68	tie to	B-13H-2, 22	112.72	116.67
B-13H-5, 94	117.94	121.89	tie to	D-14H-2, 130	118.30	121.87
D-14H-7, 10	124.60	128.17	tie to	B-14H-3, 31	123.81	128.19
B-14H-6, 19	128.19	132.57	tie to	D-15H-3, 67	128.67	132.57
D-15H-6, 61	133.11	137.01	tie to	B-15H-2, 112	132.62	137.00
B-15H-6, 16	137.66	142.04	tie to	D-16H-3, 31	137.81	142.03
D-16H-6, 64	142.69	146.91	tie to	B-16H-3, 61	143.11	146.91
B-16H-6, 28	147.30	151.10	tie to	D-17H-2, 142	146.92	151.09
D-17H-6, 40	151.90	156.07	tie to	B-17H-2, 145	151.95	156.07
B-17H-6, 43	156.93	161.05	tie to	D-18H-2, 106	156.06	161.05
D-18H-3, 139	157.89	162.88	tie to	C-18X-1, 115	157.55	162.90
C-18X-6, 133	165.23	170.58	tie to	B-19X-1, 61	165.61	170.58
B-19X-4, 82	170.32	175.29	tie to	C-19X-3, 82	169.92	175.27
C-19X-6, 112	174.72	180.07	tie to	B-20X-1, 100	175.90	180.07
B-20X-6, 142	183.82	187.99	tie to	C-20X-6, 142	183.82	188.03
			No overlap			
C-21X-5, 97	192.27	196.48	tie to	B-21X-4, 34	189.34	196.48
B-21X-6, 88	192.88	200.02	tie to	C-22X-1, 91	195.81	200.02
C-22X-4, 43	199.83	204.04	tie to	B-22X-3, 43	197.53	204.03

Notes: Portions of cores from Holes 974B, 974C, and 974D were used to construct a complete section, avoiding gaps and overlaps through Core 974D-18X. Below this core, correlations are less certain due to increased core disturbance and reduced core recovery. Data from Core 974C-20X is continued into Core 974C-21X because there was no apparent overlap with cores from Hole 974B.

um, and lithium steadily increase with depth, whereas potassium and, to a certain extent, pH and alkalinity steadily decrease with depth. Magnesium concentrations were generally constant downcore with a depletion at the base of the core, phosphate concentrations were below the lower limit of detection (2.5 μM), and silica concentrations were generally constant, with a peak occurring at 58.20 mbsf. The interstitial manganese profile was the most variable and complex; decreasing in the upper part of the hole, followed by an increase between 67.90 and 86.70 mbsf, then decreasing before increasing to the base of the core.

Evaporite-Related Fluxes

The presence of evaporites, especially halite (NaCl), anhydrite ($CaSO_4$), and gypsum ($CaSO_4 \cdot 2H_2O$), below the depth penetrated by coring would provide one source for those variables that increase with depth. The presence of such evaporites was reported nearby at Site 652 at 188.60 mbsf during ODP Leg 107 (Shipboard Scientific Party, 1987). Calcium and strontium may also originate from the interactions of these underlying Messinian brines with carbonates as carbonate recrystallization releases strontium to the interstitial waters (Deer et al., 1966). It is therefore likely that the calcium and strontium gradients (Figs. 48, 49) reflect both the presence of the more soluble gypsum in the underlying evaporites and interactions of the evaporitic brines with carbonates. Dissolution of gypsum would also supply a flux of sulfate. Such a flux would explain why sulfate depletion does not occur at this site, even though sulfate reduction appears to be the main diagenetic process. The high lithium concentrations (Fig. 49) suggest the presence of late-stage evaporitic brines in the evaporites.

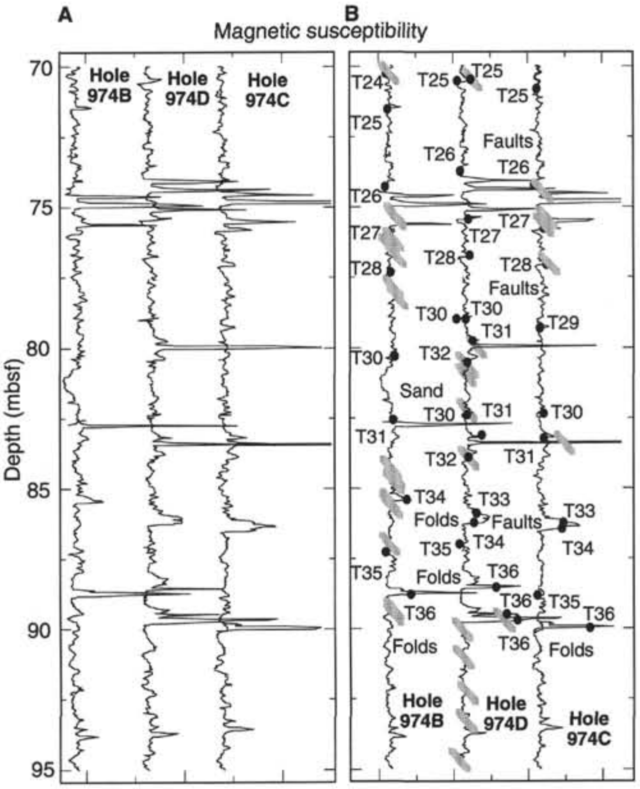

Figure 37. **A.** Detail of magnetic susceptibility data from Holes 974B, 974C, and 974D. **B.** Structural data and the location of organic-rich layers (Table 5). Note the repetition of organic-rich layers T30, T31, and T32 in Hole 974D between 79 and 84 mbsf, as well as the triplication of organic-rich layer T36 in Hole 974D between 88 and 90 mbsf. Organic-rich layer T29 is probably a repetition of T28 in Hole 974C between 77 and 80 mbsf. Double coring of organic-rich layer T25 (70.5 mbsf, Hole 974D) may be the result of a small fault, while T30 (78.8 mbsf, Hole 974D) appears to have been cored both at the bottom of Core 974D-9H and the top of Core 974D-10H (Table 5). The sand interval from 80.6 to 82.1 mbsf in Hole 974B is not seen in overlapping intervals of the other holes. Effects of folds and faults are difficult to quantify, but it can be seen that folds and faults between the susceptibility peaks associated with organic rich layer T36 and the peaks aligned at 93.8 mbsf in each hole likely have changed the thickness of that section from hole to hole. Faults indicated by gray bands indicate little offset.

Organic Matter Degradation

The ammonium interstitial water profile indicates progressive decomposition of organic matter; the reduction in the ammonium gradient toward the base of the hole (Fig. 51) indicates either a decrease in the rate of organic matter decomposition or a decrease in the organic matter content of the sediments. Ammonium concentrations are

Table 11. Significant overlaps as a result of core-to-core correlation.

Interval	Remarks
Hole 974B Core 9H, Section 6, 46 cm to Section 6, 145 cm	Sand layer not seen in other cores. Excluded from composite section.
Hole 974C Core 10H, Section 1, 0 cm to Section 2, 79 cm	Duplicated by bottom of Core 9H. Subtract 2.21 m for mcd.
Hole 974D Core 10H, Section 1, 0 cm to Core 10H, Section 2, 121 cm	Duplicated lower in core. Add additional 3.42 m for mcd.

Note: Overlapping section must be specially regarded in mcd calculations.

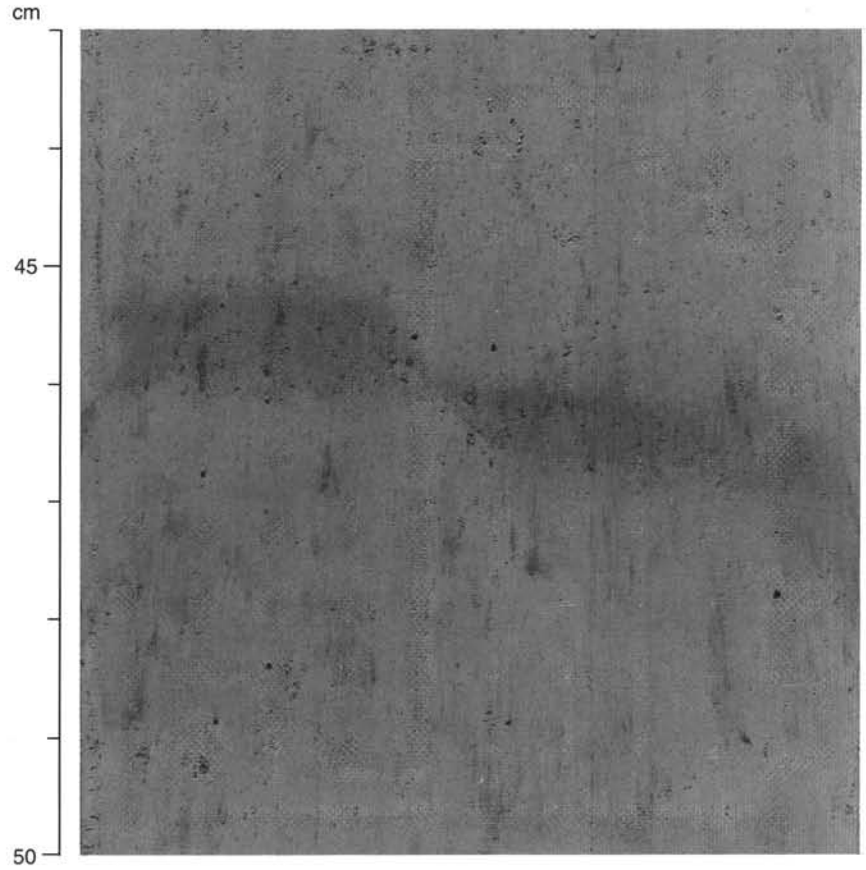

Figure 38. Core close-up photo of 974C-16H-5, 46 cm. Normal fault with displacement of 7 mm.

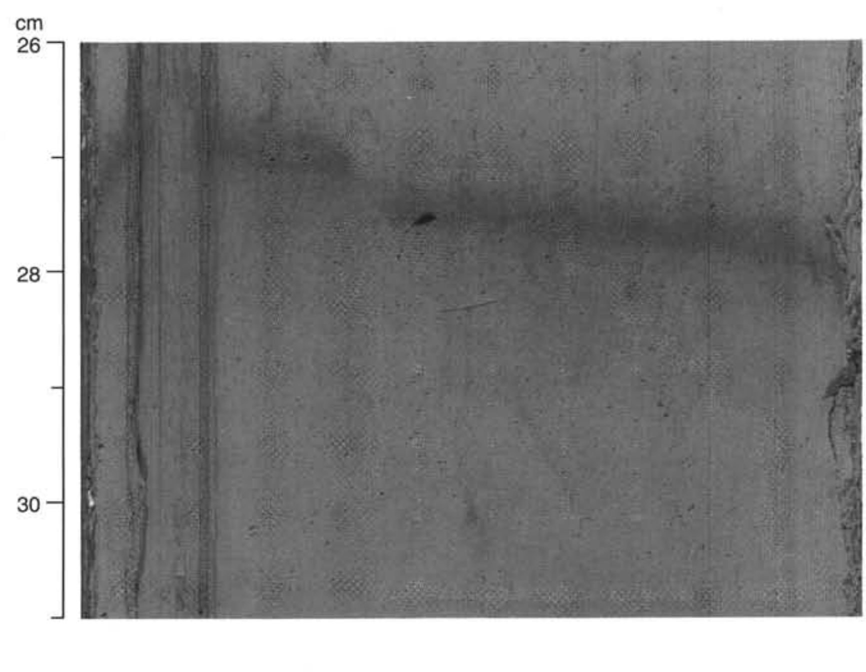

Figure 39. Core close-up photo of 974B-5H-2, 27 cm. Normal fault with displacement of 6 mm. Note that the fault is visible in the clay as a faint straight line.

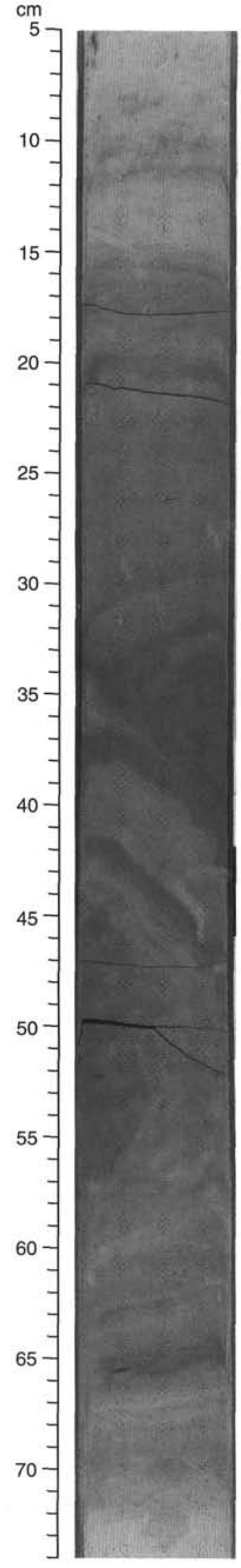

Figure 40. Core close-up photo of 974C-16H-6, 5–74 cm. 50-cm-scale slump fold, overturned towards the east (core coordinates).

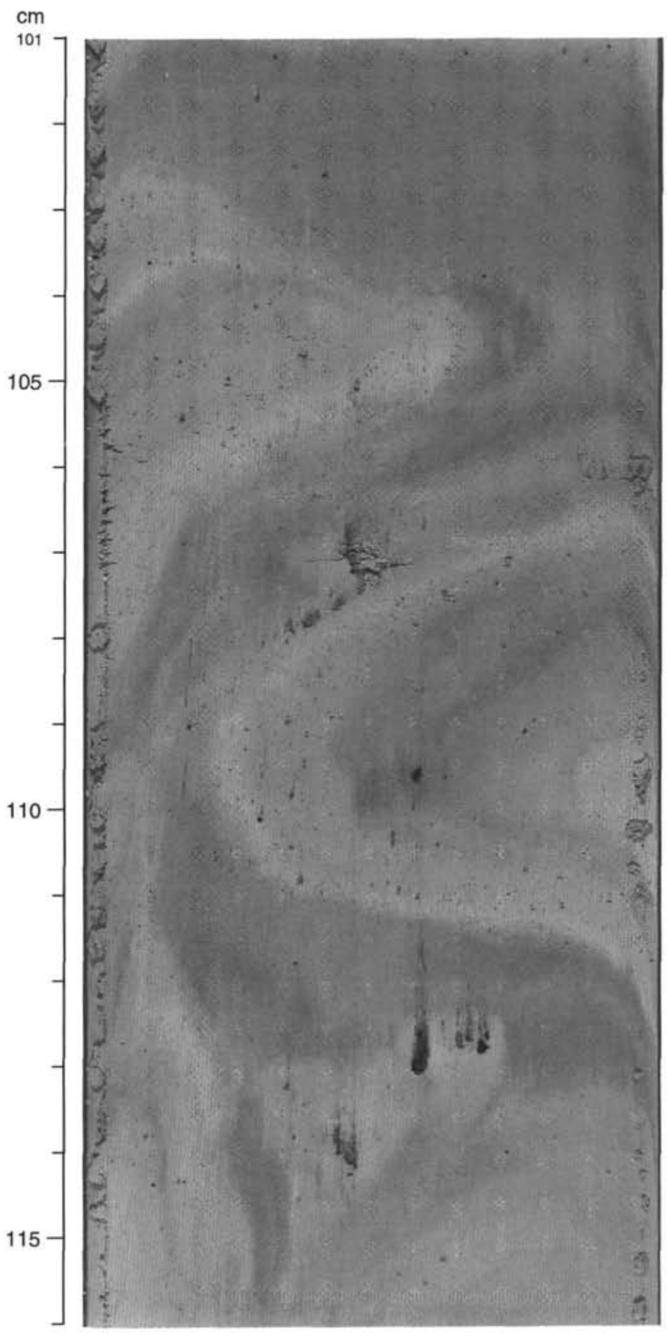

Figure 41. Core close-up photo of 974B-12H-5, 101–116 cm. Small-scale slump folds within a broad zone of slumping.

generally low, reflecting limited decomposition of organic matter. Ion exchange reactions during organic matter decomposition lead to a small amount of ammonium being fixed by clay minerals with concomitant lithium release, which should be reflected in the lithium profile. Any such release of lithium into the interstitial waters is masked by the lithium flux from below. In contrast to the ammonium profile, there is no evidence of methanogenesis (see "Organic Geochemistry" section, this chapter). The interstitial water sulfate concentration indicates that organic matter degradation at this site occurs mainly by sulfate reduction. The presence of such sulfate concentrations would effectively inhibit the development of methanogenesis (Claypool and Kvenvolden, 1983). Phosphate concentrations are below the lower limit of detection, reflecting the over-

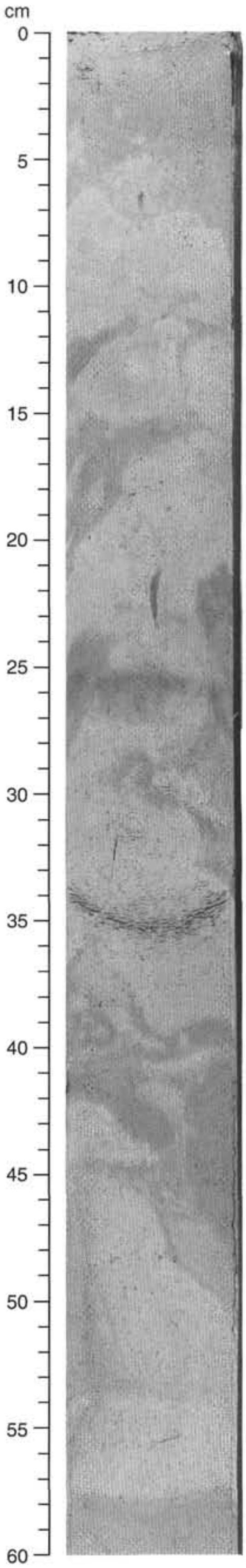

Figure 42. Core close-up photo of 974C-15H-4, 0–60 cm. Disrupted bedding, produced by slumping.

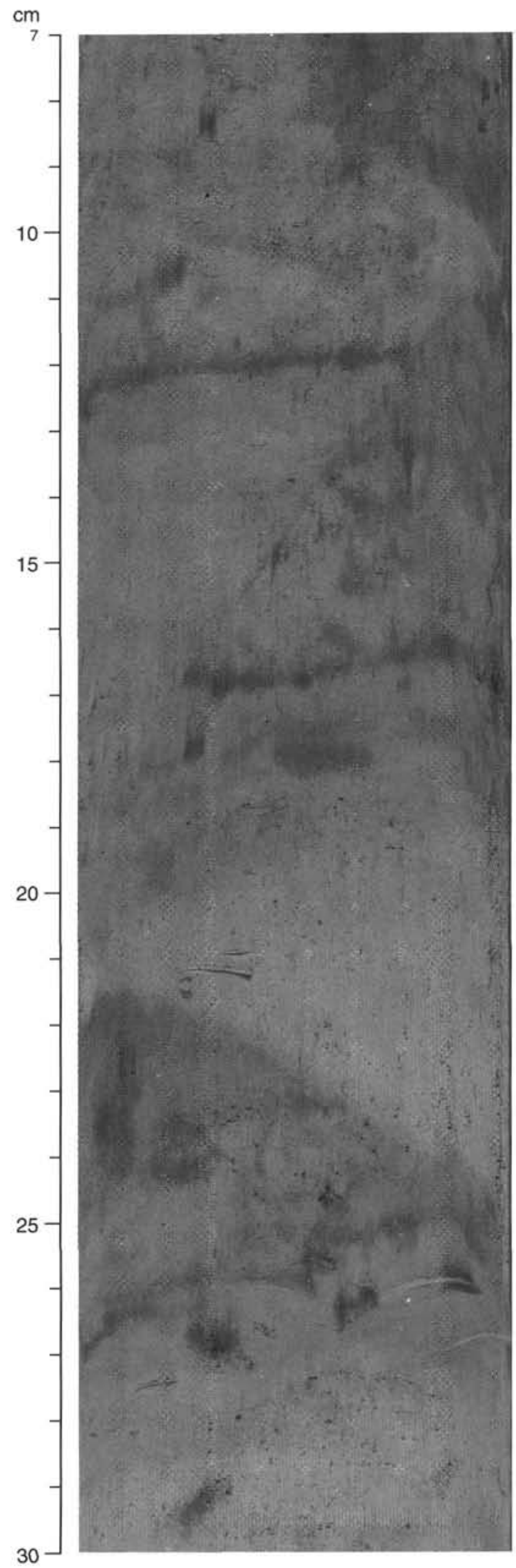

Figure 43. Core close-up photo of 161-974D-10H-3, 7–30 cm. Reverse faults. The boundary between light- and dark-colored clay at 28 cm is repeated at 20 cm by a west-dipping fault (core coordinates). The thin dark-grey lamina at 17 cm is repeated at 12 cm by a conjugate east-dipping reverse fault.

Table 12. Results of inorganic and total carbon (TC) analyses of sediment samples from lithostratigraphic Units I to IV at Site 974.

Core, section, interval (cm)	Depth (mbsf)	Inorg. C (wt%)	$CaCO_3$ (wt%)	TC (wt%)	TOC (wt%)	TN (wt%)	TS (wt%)	C/N
Unit 1: Pliocene–Pleistocene hemipelagic nannofossil-rich clays, with ash beds and sapropels								
161-974A-								
1H-1, 13–14	5.14	5.09	42.40	5.20	0.11	0.04	0.09	3.21
1H-1, 77–78	5.78	3.05	25.41	3.42	0.37	0.06	0.06	7.19
1H-1, 101–102	6.02	2.21	18.41	2.89	0.68	0.07	0.30	11.33
1H-1, 106–107	6.07	3.26	27.16	4.86	1.60	0.14	3.95	13.33
1H-3, 2–3	8.03	4.76	39.65	4.90	0.14	0.04	0.00	4.08
1H-5, 53–54	11.54	2.87	23.91	2.92	0.05	0.02	0.37	2.92
1H-6, 91–92	13.42	2.66	22.16	2.76	0.10	0.02	0.54	5.83
161-974B-								
1H-1, 30–31	0.31	3.15	26.24	3.27	0.12	0.04	0.08	3.50
1H-2, 62–63	2.13	3.24	26.99	3.39	0.15	0.03	0.00	5.83
1H-3, 113–114	4.14	2.36	19.66	2.53	0.17	0.03	0.01	6.61
1H-4, 80–81	5.31	3.27	27.24	3.55	0.28	0.03	0.08	10.89
1H-5, 31–32	6.32	3.40	28.32	3.59	0.19	0.05	0.15	4.43
1H-CC, 16–17	6.74	3.19	26.57	4.90	1.71	0.15	3.59	13.30
2H-3, 69–70	10.20	1.47	12.25	1.62	0.15	0.02	0.12	8.75
2H-4, 44–45	11.45	2.30	19.16	2.28	0.00	0.00	0.13	
2H-5, 12–13	12.63	2.25	18.74	2.12	0.00	0.00	0.10	
2H-5, 60–61	13.11	2.65	22.07	2.72	0.07	0.01	0.13	8.17
2H-6, 144–145	15.45	7.29	60.73	7.36	0.07	0.02	0.00	4.08
3H-1, 22–23	16.23	3.78	31.49	3.95	0.17	0.03	0.00	6.61
3H-1, 26–27	16.27	5.75	47.90	5.89	0.14	0.03	0.00	5.44
3H-3, 15–16	19.16	4.96	41.32	6.47	1.51	0.09	1.59	19.57
3H-4, 39–40	20.90	0.37	3.08	0.38	0.01	0.00	0.10	
3H-5, 143–144	23.44	2.25	18.74	2.53	0.28	0.00	0.08	
3H-6, 83–84	24.34	6.03	50.23	6.07	0.04	0.03	0.00	1.56
4H-3, 132–133	29.83	6.12	50.98	6.03	0.00	0.00	0.03	
4H-4, 25–26	30.26	6.92	57.64	7.11	0.19	0.02	0.07	11.08
4H-4, 38–39	30.39	1.79	14.91	1.81	0.02	0.02	12.91	1.17
4H-5, 27–28	31.78	3.70	30.82	5.28	1.58	0.12	2.41	15.36
4H-5, 111–112	32.62	4.28	35.65	5.98	1.70	0.14	6.25	14.17
4H-6, 86–87	33.87	0.78	6.50	0.72	0.00	0.00	0.19	
5H-1, 13–14	35.14	1.71	14.24	1.77	0.06	0.02	0.06	3.50
5H-1, 30–31	35.31	4.63	38.57	4.73	0.10	0.04	0.00	2.92
5H-1, 54–55	35.55	1.31	10.91	1.69	0.38	0.05	1.62	8.87
5H-1, 68–69	35.69	2.82	23.49	5.97	3.15	0.22	5.12	16.70
5H-2, 46–47	36.97	2.65	22.07	5.24	2.59	0.20	3.43	15.11
5H-2, 63–64	37.14	3.39	28.24	5.56	2.17	0.17	3.39	14.89
5H-3, 134–136	39.35	3.35	27.91	4.05	0.70	0.07	0.32	11.67
5H-4, 24–25	39.75	2.97	24.74	3.68	0.71	0.08	0.00	10.35
5H-6, 94–96	43.45	6.82	56.81	7.14	0.32	0.02	0.00	18.67
5H-6, 134–136	43.85	1.60	13.33	0.00	0.00	0.02	0.00	0.00
6H-1, 9–12	44.61	4.30	35.82	4.21	0.00	0.01	0.00	0.00
6H-2, 76–77	46.77	3.34	27.82	3.38	0.04	0.03	0.00	1.56
6H-2, 5–6	50.56	2.82	23.49	7.07	4.25	0.26	2.44	19.07
6H-5, 20–21	50.71	3.32	27.66	4.45	1.13	0.10	2.06	13.18
6H-5, 134–135	51.85	2.29	19.08	6.32	4.03	0.20	2.75	23.51
6H-5, 145–147	51.96	2.23	18.58	2.76	0.53	0.06	0.44	10.31
6H-6, 84–85	52.85	4.51	37.57	6.86	2.35	0.14	2.91	19.58
6H-6, 148–149	53.49	8.25	68.72	8.14	0.00	0.00	0.00	
6H-7, 62–63	54.13	4.41	36.74	7.50	3.09	0.22	1.23	16.39
7H-1, 5–6	54.06	2.30	19.16	2.35	0.05	0.02	0.07	2.92
7H-1, 63–64	54.64	3.43	28.57	3.47	0.04	0.02	0.00	2.33
7H-1, 117–118	55.18	0.38	3.17	6.65	6.27	0.41	14.14	17.84
7H-2, 66–67	55.87	4.04	33.65	4.38	0.34	0.05	0.00	7.93
7H-5, 25–26	59.96	3.37	28.07	5.31	1.94	0.15	1.99	15.09
7H-5, 74–75	60.45	4.29	35.74	5.06	0.77	0.01	0.03	89.83
7H-5, 97–98	60.68	5.00	41.65	7.09	2.09	0.17	1.05	14.34
8H-1, 76–77	64.27	4.70	39.15	4.73	0.03	0.03	0.00	1.17
8H-1, 105–106	64.56	4.50	37.49	5.10	0.60	0.06	0.00	11.67
8H-4, 11–12	68.02	2.39	19.91	6.30	3.91	0.27	12.00	16.90
8H-5, 36–37	69.77	4.39	36.57	4.34	0.00	0.02	0.00	0.00
8H-5, 85–86	70.26	3.81	31.74	6.01	2.20	0.18	0.11	14.26
8H-5, 142–143	70.83	1.85	15.41	1.88	0.03	0.04	0.00	0.87
8H-5, 148–149	70.89	2.00	16.66	2.11	0.11	0.05	1.20	2.57
8H-6, 61–62	71.52	4.35	36.24	7.02	2.67	0.17	2.00	18.32
8H-7, 49–50	72.90	7.49	62.39	7.41	0.00	0.01	0.00	0.00
9H-1, 130–131	74.32	5.41	45.07	7.28	1.87	0.12	0.00	18.18
9H-3, 4–5	75.95	4.30	35.82	5.82	1.52	0.12	0.00	14.78
9H-5, 141–142	80.32	3.77	31.40	6.49	2.72	0.19	0.22	16.70
10H-1, 9–10	82.60	2.34	19.50	4.16	1.82	0.14	1.43	15.17
10H-3, 26–27	85.47	2.42	20.16	4.80	2.38	0.18	0.00	15.43
10H-4, 60–61	87.31	3.14	26.16	6.09	2.95	0.19	1.15	18.11
161-974C-								
1H-1, 129–130	1.30	1.77	14.74	1.63	0.00	0.02	0.00	0.00
1H-2, 22–23	1.73	3.52	29.32	3.73	0.21	0.05	0.00	4.90
1H-2, 137–138	2.88	3.19	26.57	3.46	0.27	0.03	0.00	10.50
1H-3, 35–36	3.36	2.10	17.49	2.45	0.35	0.03	0.00	13.61
2H-2, 23–24	6.04	2.64	21.99	3.18	0.54	0.04	0.00	15.75
2H-2, 59–60	6.40	0.96	8.00	1.14	0.18	0.02	0.00	10.50
2H-3, 109–110	8.40	3.57	29.74	4.15	0.58	0.05	0.00	13.53
2H-6, 89–90	12.70	7.13	59.39	7.55	0.42	0.03	0.00	16.33
3H-1, 30–31	14.11	1.73	14.41	1.91	0.18	0.01	0.00	21.00

Table 12 (continued).

Core, section, interval (cm)	Depth (mbsf)	Inorg. C (wt%)	$CaCO_3$ (wt%)	TC (wt%)	TOC (wt%)	TN (wt%)	TS (wt%)	C/N
3H-2, 65–66	15.96	4.49	37.40	5.74	1.25	0.10	1.45	14.58
3H-2, 105–106	16.36	4.20	34.99	4.57	0.37	0.04	0.00	10.79
3H-5, 38–39	20.19	3.20	26.66	3.60	0.40	0.04	0.00	11.67
3H-6, 128–129	22.59	6.28	52.31	6.68	0.40	0.03	0.00	15.56
3H-7, 11–12	22.92	5.13	42.73	7.20	2.07	0.14	1.87	17.25
4H-1, 60–61	23.91	2.95	24.57	3.33	0.38	0.04	0.00	11.08
4H-3, 112–113	27.43	6.56	54.64	6.84	0.28	0.03	0.00	10.89
4H-4, 115–116	28.96	3.76	31.32	4.02	0.26	0.04	0.00	7.58
4H-4, 128–129	29.09	4.14	34.49	4.59	0.45	0.04	0.00	13.13
4H-5, 55–56	29.86	4.40	36.65	6.37	1.97	0.15	3.12	15.32
4H-5, 75–76	30.06	1.82	15.16	2.04	0.22	0.03	0.00	8.56
5H-1, 27–28	33.08	2.75	22.90	5.88	3.13	0.23	4.87	15.88
5H-1, 48–49	33.29	0.78	6.50	0.93	0.15	0.02	0.07	8.75
5H-2, 6–7	34.37	2.59	21.60	5.51	2.92	0.23	3.65	14.81
5H-2, 19–20	34.50	2.94	24.50	4.72	1.78	0.13	2.42	15.97
5H-2, 88–89	35.19	3.18	26.49	3.82	0.64	0.07	0.10	10.67
5H-3, 72–73	36.53	3.79	31.57	4.67	0.88	0.09	0.00	11.41
5H-4, 66–67	37.97	4.25	35.40	6.31	2.06	0.15	2.16	16.02
5H-5, 43–44	39.24	0.47	3.92	0.57	0.10	0.02	0.00	5.83
5H-5, 65–66	39.46	0.31	2.58	0.44	0.13	0.02	0.00	7.58
5H-CC, 8–9	42.64	4.63	38.57	4.94	0.31	0.04	0.00	9.04
6H-1, 67–68	42.98	3.38	28.16	3.80	0.42	0.04	0.00	12.25
6H-4, 68–69	47.49	1.07	8.91	1.24	0.17	0.02	0.00	9.92
6H-5, 40–41	48.71	2.46	20.49	7.02	4.56	0.28	4.29	19.00
6H-5, 58–59	48.89	3.32	27.66	4.72	1.40	0.20	1.02	8.17
6H-6, 27–28	50.08	2.23	18.58	6.54	4.31	0.28	3.67	17.96
6H-6, 39–40	50.20	2.33	19.41	3.20	0.87	0.08	0.63	12.69
6H-6, 121–122	51.02	4.42	36.82	7.35	2.93	0.20	2.04	17.09
6H-CC, 30–31	52.20	3.30	27.49	3.63	0.33	0.05	0.00	7.70
6H-CC, 33–34	52.23	4.07	33.90	7.55	3.48	0.25	0.61	16.24
7H-1, 9–10	51.90	4.40	36.65	7.86	3.46	0.25	0.18	16.15
7H-1, 76–77	52.57	2.70	22.49	2.85	0.15	0.04	0.00	4.38
7H-2, 31–32	53.62	0.21	1.75	5.48	5.27	0.35	0.00	17.57
7H-5, 123–124	59.04	3.18	26.49	5.72	2.54	0.18	3.72	16.46
7H-6, 45–46	59.76	4.26	35.49	7.30	3.04	0.19	0.59	18.67
9H-2, 70–71	73.01	4.73	39.40	4.92	0.19	0.04	0.00	5.54
161-974D-								
5H-6, 1–2	37.51	2.53	21.07	3.17	0.64	0.06	1.19	12.37
Unit 2: Pliocene pelagic to hemipelagic nannofossil clay and ooze								
161-974B-								
11H-1, 92–93	92.93	6.08	50.65	6.20	0.12	0.02	0.00	7.00
11H-3, 134–135	96.35	7.59	63.22	7.59	0.00	1.17	0.00	0.00
11H-5, 42–43	98.43	5.83	48.56	5.77	0.00	0.02	0.00	0.00
11H-7, 54–55	101.55	6.47	53.90	6.41	0.00	2.10	0.00	0.00
12H-2, 34–35	103.35	5.98	49.81	6.12	0.14	0.02	0.00	8.17
12H-3, 71–72	105.22	6.11	50.90	6.03	0.00	2.13	0.00	0.00
12H-5, 54–55	108.05	5.08	42.32	5.34	0.26	0.03	0.00	10.11
13H-1, 96–97	111.97	6.06	50.48	6.25	0.19	0.04	0.00	5.54
13H-2, 11–12	112.62	6.23	51.90	6.27	0.04	0.03	0.02	1.56
13H-3, 93–94	114.94	1.27	10.58	1.37	0.10	0.03	0.00	3.89
13H-5, 42–43	117.43	1.81	15.08	1.83	0.02	0.02	0.00	1.17
13H-6, 96–97	119.47	6.93	57.73	7.26	0.33	0.03	0.05	12.83
13H-7, 34–35	120.35	6.36	53.00	6.51	0.15	0.03	0.09	5.83
14H-1, 36–37	120.87	2.57	21.41	2.59	0.02	0.02	0.08	1.17
14H-2, 79–80	122.80	7.23	60.23	7.41	0.18	0.03	0.00	7.00
14H-5, 69–70	127.20	6.77	56.39	7.03	0.26	0.04	0.01	7.58
14H-6, 30–31	128.31	7.62	63.47	8.12	0.50	0.03	0.02	19.44
15H-1, 48–49	130.49	6.03	50.23	6.48	0.45	0.03	0.03	17.50
15H-2, 79–80	132.30	6.96	57.98	7.29	0.33	0.03	0.03	12.83
15H-3, 148–149	134.49	7.95	66.22	8.12	0.17	0.03	0.00	6.61
15H-4, 50–51	135.01	8.10	67.47	8.31	0.21	0.02	0.00	12.25
15H-6, 56–57	138.07	4.74	39.48	4.57	0.00	0.03	0.03	0.00
16H-2, 19–20	141.20	6.91	57.56	7.18	0.27	0.03	0.02	10.50
16H-3, 40–41	142.91	5.51	45.90	5.71	0.20	0.04	0.00	5.83
16H-4, 92–93	144.93	7.32	60.98	7.44	0.12	0.03	0.00	4.67
16H-4, 123–124	145.24	4.30	35.82		0.00			
16H-6, 132–133	148.35	5.45	45.40	4.91	0.00	0.05	0.14	0.00
17H-1, 72–73	149.73	6.60	54.98	6.67	0.07	0.03	0.00	2.72
17H-6, 20–21	156.71	7.87	65.56	8.43	0.56	0.03	0.01	21.78
18H-1, 93–94	159.44	6.37	53.06		0.00			
18H-3, 44–45	161.95	7.32	60.98	7.52	0.20	0.03	0.00	7.78
18H-5, 33–34	164.84	7.10	59.14	7.63	0.53	0.05	0.00	12.37
19X-3, 28–29	168.29	7.62	63.47	7.86	0.24	0.03	0.00	9.33
19X-5, 54–36	171.35	6.46	53.81	6.60	0.14	0.03	0.00	5.44
20X-1, 59–61	175.50	6.41	53.40	6.95	0.54	0.03	0.00	21.00
20X-6, 61–62	183.02	3.78	31.49	4.06	0.28	0.02	0.00	16.33
21X-1, 81–82	185.32	6.54	54.48	7.17	0.63	0.04	0.00	18.38
21X-2, 34–36	186.35	5.37	44.73	5.70	0.33	0.03	0.00	12.83
21X-2, 78–80	186.79	6.16	51.31	6.88	0.72	0.04	0.00	21.00
21X-3, 69–70	188.20	5.35	44.57	5.85	0.50	0.04	0.00	14.58
21X-4, 83–84	189.84	6.02	50.15	6.40	0.38	0.03	0.00	14.78
21X-7, 40–41	193.91	6.44	53.65	6.93	0.49	0.03	0.00	19.06
22X-1, 111–114	195.23	6.58	54.81	7.06	0.48	0.03	0.00	18.67
22X-2, 61–62	196.22	6.35	52.90			0.03	0.00	0.00
161-974C-								
12H-CC, 31–32	109.07	6.25	52.06	6.39	0.14	0.03	0.00	5.44
13H-3, 97–99	112.78	7.06	58.81	6.97	0.00	0.03	0.01	0.00

Table 12 (continued).

Core, section, interval (cm)	Depth (mbsf)	Inorg. C (wt%)	$CaCO_3$ (wt%)	TC (wt%)	TOC (wt%)	TN (wt%)	TS (wt%)	C/N
13H-5, 126–127	116.07	1.44	12.00	1.62	0.18	0.02	0.00	10.50
13H-6, 116–117	117.47	5.73	47.73	6.05	0.32	0.03	0.00	12.44
15H-1, 20–21	128.01	7.69	64.06	7.77	0.08	0.04	0.00	2.33
15H-3, 57–58	131.38	6.03	50.23	6.19	0.16	0.03	0.00	6.22
15H-6, 62–63	135.93	8.27	68.89	8.47	0.20	0.02	0.00	11.67
16H-3, 59–60	140.90	6.50	54.15	6.64	0.14	0.04	0.00	4.08
16H-5, 35–36	143.66	7.07	58.89	7.25	0.18	0.04	0.00	5.25
16H-5, 131–132	144.62	4.89	40.73	5.29	0.40	0.04	0.00	11.67
16H-6, 51–52	145.32	5.74	47.81	5.82	0.08	0.04	0.00	2.33
18X-2, 74–75	158.65	6.03	50.23	6.38	0.35	0.04	0.02	10.21
18X-2, 86–87	158.77	6.21	51.73	6.43	0.22	0.04	0.00	6.42
18X-4, 106–107	161.97	6.60	54.98	6.93	0.33	0.04	0.00	9.63
18X-5, 147–148	163.88	6.98	58.14	7.41	0.43	0.05	0.02	10.03
18X-6, 11–12	164.02	5.96	49.65	7.49	1.53	0.04	0.00	44.63
18X-6, 60–61	164.51	5.61	46.73	5.86	0.25	0.04	0.00	7.29
19X-1, 117–118	167.28	6.62	55.14	6.73	0.11	0.02	0.00	6.42
19X-2, 46–47	168.07	7.78	64.81	8.07	0.29	0.02	0.00	16.92
19X-4, 20–21	170.81	6.82	56.81	6.98	0.16	0.02	0.00	9.33
20X-2, 72–73	177.13	6.17	51.40	6.32	0.15	0.01	0.00	17.50
20X-4, 13–14	179.54	5.88	48.98	6.16	0.28	0.02	0.00	14.20
20X-6, 72–73	183.13	5.62	46.81	5.74	0.12	0.02	0.00	7.00
21X-3, 18–19	188.49	5.60	46.65	5.80	0.20	0.02	0.00	11.67
21X-5, 69–70	192.00	6.11	50.90	6.33	0.22	0.02	0.00	12.83
21X-CC, 18–19	194.84	6.01	50.06	6.20	0.19	0.00	0.00	
161-974D-								
14H-2, 92–93	117.92	2.95	24.57	3.02	0.07	0.02	0.00	4.08
16H-3, 75–76	138.25	4.62	38.48	4.80	0.18	0.02	0.00	10.68
Unit 3: Miocene–Pliocene laminated silt to silty clay								
161-974B-								
22X-4, 87–88	199.48	0.39	3.25	0.53	0.14	0.04	0.00	4.08
22X-4, 123–124	199.84	2.98	24.82	3.66	0.68	0.06	0.00	13.22
22X-5, 3–5	200.15	0.00	0.00	8.38	0.00	0.02	0.00	0.00
161-974C-								
22X-4, 135–136	200.76	7.18	59.81	7.42	0.24	0.02	0.00	14.00
Unit 4: Miocene gray clastic sands and silt								
161-974B-								
22X-5, 55–56	200.66	2.99	24.90	1.71	0.00	0.19	1.64	0.00
161-974C-								
22X-5, 69–70	201.60	2.78	23.20	3.22	0.44	0.03	0.26	17.13

Notes: Total organic carbon (TOC) concentrations are calculated from the difference between inorganic carbon and TC concentrations. TS = total sulfur concentration. C/N ratios are calculated from TOC and total nitrogen (TN) concentrations and are given as atom/atom ratios.

all low organic matter content of the sediments at this site. Based on a Redfield N:P ratio of 1:16, such low concentrations are to be expected. Phosphate concentrations suggest the accumulation rate and organic matter content of the sediments at this site are not high.

Carbonate Diagenesis

The upper part of the alkalinity profile exhibits a minor increase to concentrations slightly higher than average seawater. This indicates either a generally low decomposition rate or low abundance of organic matter. Below 125 mbsf, the alkalinity is lower than seawater values indicating the precipitation of a carbonate phase or formation of zeolite and clay. Zeolite and clay formation is more likely because evidence for carbonate precipitation is absent (See "Lithostratigraphy" section, this chapter).

Potassium, Manganese, and Silica

The potassium interstitial profile exhibits a downcore decrease (Fig. 50), which is typical for marine sediments and indicates potassium uptake in clays. This profile is unexpected at this site, because of the presence of evaporites at depth, and may indicate an absence of potassium salts at this locality or limited upward diffusion of brine components.

The complicated manganese profile indicates a zone of manganese reduction occurring at the top of the core, probably above the shallowest sample at 4.50 mbsf. Differences below 4.50 mbsf may reflect local lithological controls on fluid-sediment interactions. The decrease in Mn below this depth is simply diffusion along the concentration gradient.

The interstitial silica profile is low and consistent, punctuated by a peak at 58.20 mbsf (Fig. 51). This interval contains an ash layer with over 50% volcanic glass (see "Lithostratigraphy" section, this chapter). Dissolution of this ash layer may account for the higher interstitial water silica concentrations in this sample. These enhanced levels of silica would make the interstitial waters less corrosive toward siliceous biofossils, resulting in enhanced preservation of diatoms and radiolarians at this depth.

In conclusion, the interstitial water profiles at Site 974 are influenced by the presence of an evaporitic brine below the depth of maximum penetration. The interstitial fluxes suggest this brine is dominated by gypsum and halite; the decrease in potassium with depth indicates an absence of potassium-bearing salts at this location. The presence of anhydrite in the brines at this site cannot be ruled out because of the low solubility of anhydrite in water.

PHYSICAL PROPERTIES

Introduction

Physical property measurements were made on whole-core sections (MST and thermal conductivity), split cores (sonic velocity), and discrete samples (index properties) for all holes at Site 974. Natural gamma ray was measured at 10-cm intervals only on the cores from Hole 974D. Index properties and thermal conductivity were measured once per section on cores from Holes 974A and 974B. Index properties were measured on one or two samples per core for Hole 974C. Thermal conductivities were measured three times per core for Holes 974C and 974D.

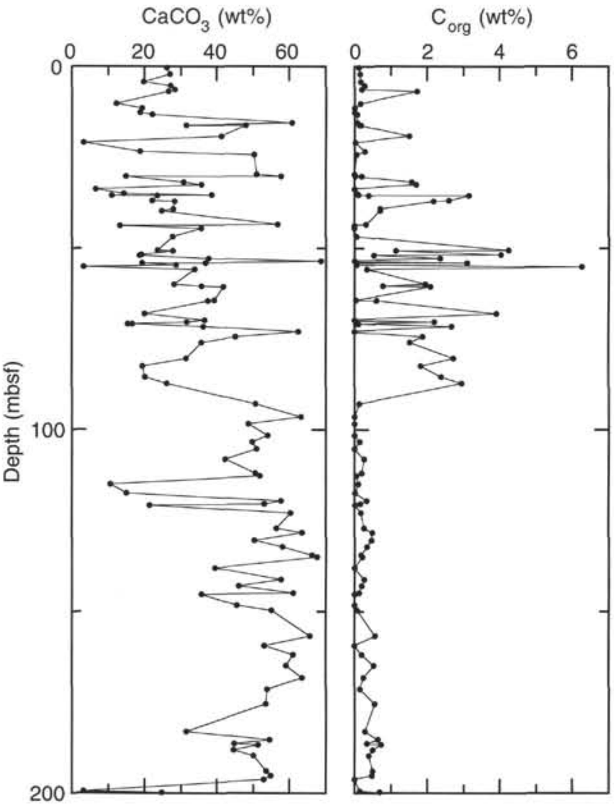

Figure 44. Downcore variations in organic carbon and $CaCO_3$ concentrations in sediment samples from Hole 974B.

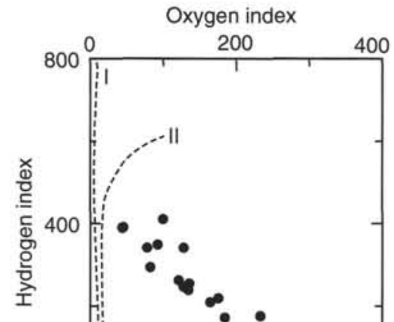

Figure 45. Rock-Eval van Krevelen-type diagram of sapropels from Hole 974B. Organic matter appears to be originally Type II algal material that has been variably oxidized to Type III continental or detrital organic matter. Hydrogen index = mg hydrocarbons/g organic carbon; oxygen index = mg CO_2/g organic carbon.

The various physical property measurements showed good hole-to-hole correlation, with due allowance for variation on short vertical scales and variances in sampling locations.

Multisensor Track (MST)

The MST measurements for Hole 974A are presented in Figure 52. The presentation is done in a format similar to that used for the

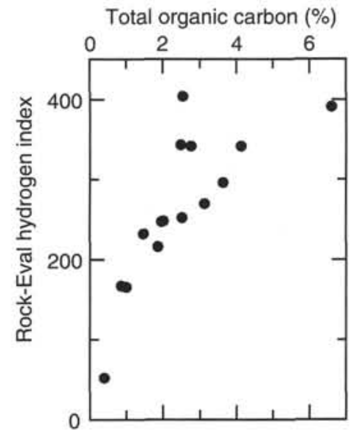

Figure 46. Comparison of Rock-Eval hydrogen index values and total organic carbon concentrations of sapropels from Hole 974B. The correspondence between increases in both parameters indicates that diminished oxidation of algal organic matter is important to enhancing the organic-carbon richness of sapropels in the Tyrrhenian Sea.

downhole logging data (this volume) to facilitate comparison. The MST measurements for Holes 974B, 974C, and 974D are similarly presented in Figures 53–55. The figure is split into 80-m vertical interval segments in order to provide sufficient detail.

The Hole 974C downhole log gamma-ray (CGR) data from the quad combo logging tool string is shown with the Hole 974D MST gamma-ray data in Figure 56. The gamma-ray measurements of the MST and the downhole logs correlate well except at the bottom of the holes. This is probably attributable to the poor hole conditions at those particular depths affecting the well log data, which has not been corrected for the effects of borehole diameter.

Thermal Conductivity

Thermal conductivity results for Holes 974B, 974C, and 974D are shown in Figure 57 and listed in Table 16 (on CD-ROM, back pocket, this volume). There is a general trend towards increasing conductivity with depth in all of the holes, but there is considerable small-scale variability caused by changes in porosity in the cores. Detailed measurements of conductivity and porosity, made on other cruises, have documented the continuous nature of this variability.

P-wave Velocity

P-wave velocity measurements (Fig. 58; Table 17 on CD-ROM, back pocket, this volume) show a downward increasing trend. Velocity increases with depth from 1.5 km/s to 1.6 km/s until about 80–90 mbsf. Below 90 mbsf, the gradient decreases. At 200 mbsf, there is an abrupt increase in velocity to values over 2 km/s, which corresponds to a clastic layer (lithostratigraphic Unit IV). The trend shown by velocity measurements is also visible in the bulk density and porosity measurements.

Index Properties

Index properties were measured with two methods, "B" and "C" (Table 18 on CD-ROM, back pocket, this volume). Bulk density (Fig. 59) increases from 1.4 g/cm³ from the seafloor to about 90–100 mbsf and then remains constant at 1.9 g/cm³. The increase in *P*-wave velocity at 200 mbsf correlates with an increase in bulk density. The sharp increase in bulk density below 200 mbsf corresponds to a clastic layer (Lithostratigraphic Unit IV).

Table 13. Results of Rock-Eval pyrolyses of sapropels selected from Hole 974B.

Core, section, interval (cm)	Depth (mbsf)	TOC (%)	T_{max} (°C)	S_1	S_2	S_3	PI	S_2/S_3	PC	HI	OI
161-974B-											
3H-3, 15–16	19.15	0.86	411.00	0.17	1.44	2.12	0.11	0.67	0.13	167	246
4H-5, 27–28	31.77	1.46	414.00	0.44	3.40	2.62	0.11	1.29	0.32	232	179
4H-5, 112–113	32.61	1.86	418.00	0.47	4.03	3.10	0.10	1.30	0.37	216	166
5H-1, 68–69	35.68	3.13	415.00	0.72	8.45	3.92	0.08	2.15	0.76	269	125
5H-2, 46–47	36.96	2.51	418.00	0.50	6.35	3.28	0.07	1.93	0.57	252	130
6H-5, 5–6	50.55	4.13	420.00	1.18	14.09	3.52	0.08	4.00	1.27	341	85
6H-5, 20–21	50.70	1.00	419.00	0.30	1.65	1.92	0.15	0.85	0.16	165	192
6H-5, 134–135	51.84	3.64	421.00	0.87	10.79	3.38	0.07	3.19	0.97	296	92
6H-6, 84–85	52.84	1.95	418.00	0.38	4.83	2.84	0.07	1.70	0.43	247	145
6H-7, 62–63	54.12	2.48	421.00	0.59	8.52	3.34	0.06	2.55	0.75	343	134
7H-1, 117–118	55.17	6.60	412.00	2.90	25.83	3.63	0.10	7.11	2.39	391	55
7H-5, 25–26	59.96	2.01	425.00	0.35	5.00	2.56	0.07	1.95	0.44	248	127
7H-5, 97–98	60.68	2.53	427.00	0.59	10.23	2.85	0.05	3.58	0.90	404	112
10H-4, 60–61	87.30	2.77	428.00	0.47	9.46	2.74	0.05	3.45	0.82	341	98
16H-4, 123–124	145.23	0.40	433.00	0.03	0.21	1.60	0.12	0.13	0.02	52	400

Notes: Total organic carbon (TOC) concentrations are derived from the Rock-Eval parameters and therefore differ somewhat from the TOC values of the same samples in Table 12. Units of the various Rock-Eval parameters are given in the "Explanatory Notes" chapter (this volume).

Table 14. $U_{37}^{k'}$ values and sea-surface paleotemperature estimates obtained from biomarker extracts of sapropels from Hole 974B.

Core, section, interval (cm)	Depth (mbsf)	TOC (wt%)	$U_{37}^{k'}$	SST (°C)
161-974B-				
1H-CC, 16–17	6.74	1.71	0.466	16.5
3H-3, 15–16	19.16	1.51	0.555	18.7
4H-5, 27–28	31.78	1.58	0.662	21.3
4H-5, 111–112	32.62	1.70	0.501	17.3
5H-1, 68–69	35.69	3.15	0.555	18.7
5H-2, 46–47	36.97	2.59	0.640	20.7
5H-2, 63–64	37.14	2.17	0.678	21.7
6H-5, 5–6	50.56	4.25	0.675	21.6
6H-5, 20–21	50.71	1.13	0.509	17.5
6H-5, 134–135	51.85	4.03	0.665	21.3
6H-6, 84–85	52.85	2.35	0.680	21.7
6H-7, 62–63	54.13	3.09	0.677	21.6
7H-1, 117–118	55.18	6.27	0.568	19.0
7H-5, 25–26	59.96	1.94	0.595	19.6
7H-5, 97–98	60.68	2.09	0.602	19.8
8H-4, 11–12	68.02	3.91	0.617	20.2
8H-5, 85–86	70.26	2.20	0.537	18.2
8H-6, 61–62	71.52	2.67	0.599	19.7
9H-1, 130–131	74.32	1.87	0.717	22.6
9H-3, 4–5	75.95	1.52	0.674	21.6
9H-5, 141–142	80.32	2.72	0.716	22.6
10H-1, 9–10	82.60	1.82	0.666	21.4
10H-3, 26–27	85.47	2.38	0.787	24.3
10H-4, 60–61	87.31	2.95	0.851	25.9

Notes: The calibration curve of Ternois et al. (unpubl. data), which is based on Mediterranean populations of *Emiliania huxleyi,* was used. This calibration yields temperatures ~2.9°C cooler than the more commonly used calibration curve of Prahl and Wakeham (1987).

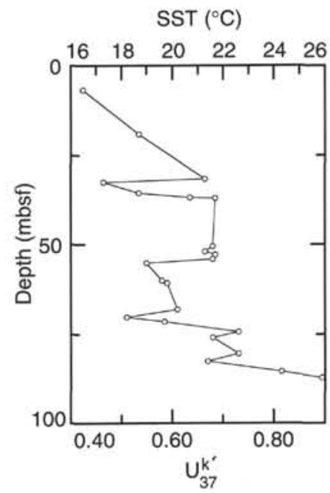

Figure 47. Sea-surface temperatures (SST) calculated from $U_{37}^{k'}$ values obtained from biomarker extracts of sapropels from Hole 974B. The calibration curve of Ternois et al. (unpubl. data), which is based on Mediterranean populations of *Emiliania huxleyi,* was used. This calibration yields temperatures ~2.9°C cooler than the more commonly used calibration curve of Prahl and Wakeham (1987).

Porosity decreases strongly with depth from 0–70 mbsf (Fig. 60). Below 70 mbsf, the porosity remains around 60%.

Grain densities measured with the two methods are compared in Figure 61. Measurements based upon wet volumes and wet and dry weights show considerable scatter. Measurements made with dry volumes and wet and dry weights are much more consistent with values of ~2.7 g/cm^3.

DOWNHOLE LOGGING

Logging operations began in Hole 974C after the hole was conditioned for logging with a short wiper trip. The wiper trip encountered no drag and only 6 m of sediment fill in the bottom of the hole, indicating that conditions were good for logging. The hole was flushed with seawater and no logging mud was used. The bit was positioned at 63.36 mbsf (3527.56 mbrf) at the start of the logging. Near the end of each logging run, shortly before the logging tools reached the drill-pipe, the bit was raised approximately 20 m (to ~43.0 mbsf) to allow more of the upper borehole to be logged. Hole 974C was thus logged from 186.0 mbsf up to 36.0 mbsf. Three strings of logging tools were used: quad combination (quad combo), Formation MicroScanner (FMS), and geochemical tool (GLT; see "Explanatory Notes" chapter, this volume; Fig. 62). A full repeat section of the hole was logged with the FMS log and a short repeat section (3650–3583 mbrf) with the GLT.

No significant operational or hole stability problems occurred. Because the Bottom-Hole Assembly had a Lockable Float Value (LFV), the GHMT logging tool string and the Lamont-Doherty temperature tool were not used at Hole 974C. The clearances for these tools through the LFV were considered too small for safe operation.

Table 19 shows the intervals logged with each tool string. Caliper measurements indicate a variable borehole diameter over most of the

Table 15. Interstitial water data from Site 974, Tyrrhenian Sea.

Core, section, interval (cm)	Depth (mbsf)	pH	Alkalinity (mM)	Salinity (‰)	Cl (mM)	Ca (mM)	Mg (mM)	Mn (μM)	Sr (μM)	SO_4 (mM)	NH_4 (μM)	H_4SiO_4 (μM)	Li (μM)	Na (mM)	K (mM)	PO_4 (μM)
161-974B-																
1H-3, 145–150	4.50	7.48	3.151	38	614	12.6	56.8	9.9	128.9	30.84	115	204.8	46.3	478.0	14.1	<2.5
2H-3, 145–150	11.00	7.44	3.181	38	608	13.7	54.8	8.9	161.4	32.16	129	240.5	50.5	538.1	14.6	<2.5
3H-3, 145–150	20.50	7.45	2.840	38	617	14.3	54.1	6.9	197.3	28.88	162	176.2	55.8	514.8	13.5	<2.5
4H-3, 145–150	30.00	7.30	2.613	38	617	14.4	53.3	6.0	227.7	26.35	213	128.6	62.2	538.7	13.0	<2.5
5H-3, 145–150	39.50	7.35	2.819	38	619	15.3	53.3	6.3	249.4	30.75	235	161.9	68.3	553.0	13.6	<2.5
6H-3, 145–150	49.00	7.29	2.790	38	629	15.5	53.6	5.6	259.4	25.12	270	152.4	71.2	492.8	11.2	<2.5
7H-3, 145–150	58.20	7.32	3.040	38	640	17.2	53.2	5.8	284.1	24.70	209	300.0	76.6	516.4	11.0	<2.5
8H-3, 135–140	67.90	7.14	2.967	40	636	17.9	52.6	8.4	292.3	25.02	289	142.9	82.6	538.4	10.9	<2.5
9H-3, 145–150	77.40	7.16	2.860	39	639	18.9	53.7	6.1	321.9	25.46	246	181.0	93.7	536.3	10.5	<2.5
10H-3, 145–150	86.70	7.10	2.911	40	641	19.5	53.7	7.9	340.2	25.72	340	176.2	102.5	542.3	10.0	<2.5
11H-3, 145–150	96.50	7.22	2.986	40	674	20.5	55.0	6.4	363.2	24.05	324	154.8	114.0	548.6	9.6	<2.5
14H-3, 145–150	125.00	7.22	2.385	40	682	24.5	54.0	4.6	453.9	23.14	376	161.9	140.3	548.2	8.8	<2.5
17H-3, 145–150	153.50	7.04	1.977	43	717	30.6	55.8	5.7	555.0	23.19	504	166.7	164.5	566.9	8.1	<2.5
20X-3, 145–150	179.40	7.17	1.897	45	733	38.4	46.5	6.9	632.6	26.23	507	181.0	187.7	576.6	7.2	<2.5

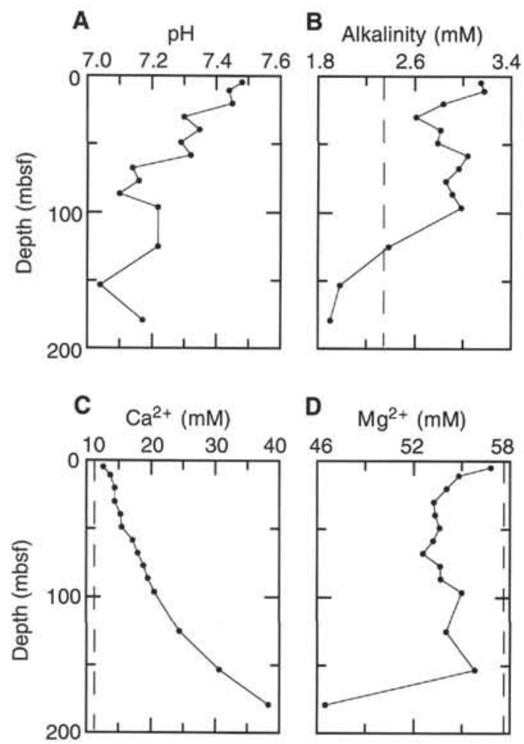

Figure 48. Concentration profiles of (**A**) pH, (**B**) alkalinity, (**C**) calcium, and (**D**) magnesium in Hole 974B. The dashed lines indicate standard seawater (International Association for the Physical Sciences of the Ocean [IAPSO]) composition.

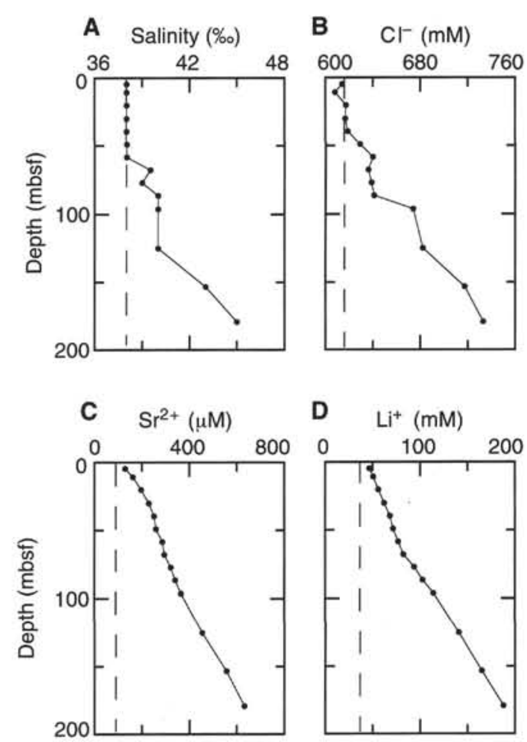

Figure 49. Concentration profiles of (**A**) salinity, (**B**) chloride, (**C**) strontium, and (**D**) lithium in Hole 974B. The dashed lines indicate standard seawater (IAPSO) composition.

logged interval, which affected the quality of some of the measurements sensitive to hole diameter, notably the density log. The sonic log is generally of good quality but requires post-cruise processing.

Two passes of the FMS tool string provided high-resolution resistivity images of the borehole wall, measurements of the three vector components of the local magnetic field, and borehole inclination, deviation, and diameter in two orthogonal directions. The FMS images are of lower quality in the lower part of the logged interval, where the borehole diameter exceeded 15 inches (38 cm), because of the poor contact the FMS pads had with the borehole wall. Bridging problems at the bottom of the hole did not allow the FMS to be run as deep as the quad combo.

Two main log units may be identified on the basis of the log response. These units agree with those identified by the sedimentologists from lithologic criteria on core observations (see "Lithostratigraphy" section, this chapter).

In Logging Unit 1 (36.0–90.0 mbsf; Pleistocene–Pliocene hemipelagic sediments), there is a large variation in log values. This is particularly true for the gamma ray, uranium, and thorium data and suggests a rather heterogeneous lithology, as is observed in the recovered cores. The caliper logs indicate variable hole conditions throughout the section, probably because of the unconsolidated nature and variable lithology.

Detailed examination of the logs indicates that Logging Unit 1 may be subdivided into intervals that are bounded by changes in natural radioactivity. The most prominent factor is the high variability in thorium content, mainly in the upper part of the logged interval. This seems to be related to the presence of volcanic ash layers and mud turbidites. Uranium content variations (for example, between 52.0–

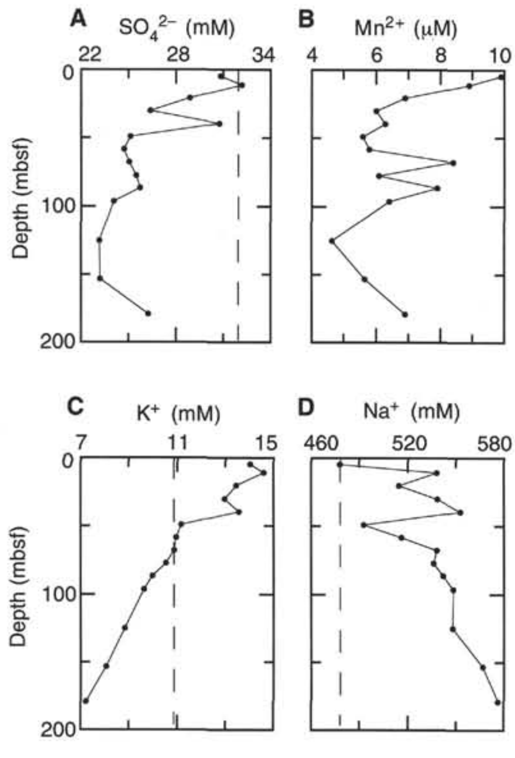

Figure 50. Concentration profiles of (**A**) sulfate, (**B**) manganese, (**C**) potassium, and (**D**) sodium in Hole 974B. The dashed lines indicate standard seawater (IAPSO) composition.

54.0, 57.0–59.0, and 65.0–66.0 mbsf) also may be related to organic-rich layers (sapropels), but the vertical resolution of the sensor is larger than the thin sapropel layers observed in the cores.

At the base of Logging Unit 1, distinct changes in most of the log values (calipers, PEF, SGR, CGR, Th, resistivity, and density) occur at the boundary between Units 1 and 2.

Logging Unit 2 (90.0–186.0 mbsf; Pliocene pelagic to hemipelagic sediments) shows a rather uniform log response. Caliper measurements indicate a variable borehole diameter between 148.0 and 186.0 mbsf.

IN SITU TEMPERATURE MEASUREMENTS

Downhole temperature measurements were made with the ADARA temperature tool at five depths in Hole 974B. The instrument worked well on all runs.

The ADARA temperature data were reduced to in situ values following the procedures outlined in the "Explanatory Notes" chapter, this volume. The results are presented in Table 20. The individual temperature measurement runs are shown in Figure 63A–E. The temperature data were combined with the thermal conductivity measurements (see "Physical Properties" section this chapter) to determine heat flow. The thermal conductivity varies with depth, showing a general increase down the hole, so the temperature data were plotted vs. the integrated thermal resistivity (Fig. 64). Thermal resistivity is the inverse of the thermal conductivity, and a plot of temperature vs. the integrated thermal resistivity will be a straight line if the heat flow is purely conductive and there are no time-dependent temperature disturbances. The best-fitting linear regression to the data is shown in Figure 64 and is an excellent fit. The slope of the line is the heat flow, 157 mW/m^2. This heat-flow value is virtually identical with the 160 mW/m^2 value obtained during ODP Leg 107 at this location at Site 652 (Kastens, Mascle, Auroux, et al., 1987). That measurement was done with several runs of the WSTP probe and a limited number of thermal conductivity measurements. These values are typical for the Tyrrhenian Sea, which has high and variable heat flow associated with its young age (Della Vadova et al., 1984; Hutchison et al., 1985).

REFERENCES

Borsetti, A.M., Curzi, P.V., Landuzzi, V., Mutti, M., Ricci Lucchi, F., Sartori, R., Tomadin, L., and Zuffa, G.G., 1990. Messinian and Pre-Messinian sediments from ODP Leg 107 Sites 652 and 654 in the Tyrrhenian Sea: sedimentologic and petrographic study and possible comparisons with Italian sequences. *In* Kastens, K.A., Mascle, J., et al., *Proc. ODP, Sci. Results*, 107: College Station, TX (Ocean Drilling Program), 169–186.

Bouma, A.H., 1962. *Sedimentology of Some Flysch Deposits: A Graphic Approach to Facies Interpretation:* Amsterdam (Elsevier).

Cande, S.C., and Kent, D.V., 1995. Revised calibration of the geomagnetic polarity timescale for the Late Cretaceous and Cenozoic. *J. Geophys. Res.*, 100:6093–6095.

Champion, D.E., Lanphere, M.A., and Kuntz, M.A., 1988. Evidence for a new geomagnetic reversal from lava flows in Idaho: discussion of short polarity reversals in the Brunhes and Late Matuyama polarity chrons. *J. Geophys. Res.*, 93:11667–11681.

Channell, J.E.T., and Mareschal, J.C., 1989. Delamination and asymmetric lithospheric thickening in the development of the Tyrrhenian Rift. *In* Coward, M.P., Dietrich, D., and Park, R.G. (Eds.), *Conference on Alpine Tectonics:* Geol. Soc. Spec. Publ. London, 45:285–302.

Channell, J.E.T., and Torii, M., 1990. Two "events" recorded in the Brunhes Chron at Hole 650A (ODP Leg 107, Tyrrhenian Sea): geomagnetic phenomena? *In* Kastens, K.A., Mascle, J., et al., *Proc. ODP, Sci. Results*, 107: College Station, TX (Ocean Drilling Program), 347–359.

Channell, J.E.T., Torii, M., and Hawthorne, T., 1990. Magnetostratigraphy of sediments recovered at Sites 650, 651, 652, and 654 (Leg 107, Tyrrhenian Sea). *In* Kastens, K.A., Mascle, J., et al., *Proc. ODP, Sci. Results*, 107: College Station, TX (Ocean Drilling Program), 335–346.

Cheddadi, R., and Rossignol-Strick, M., 1995. Improved preservation of organic matter and pollen in Eastern Mediterranean sapropels. *Paleoceanography*, 10:301–309.

Cita, M., Vismara Schilling, A., and Bossio, A., 1980. Stratigraphy and paleoenvironment of the Cuevas del Almanzora section (Vera Basin): a re-interpretation. *Riv. Ital. Paleontol.*, 86:215–240.

Cita, M.B., Santambrogio, S., Melillo, B., and Rogate, F., 1990. Messinian paleoenvironments: new evidence from the Tyrrhenian Sea (ODP Leg 107). *In* Kastens, K.A., Mascle, J., et al., *Proc. ODP, Sci. Results*, 107: College Station, TX (Ocean Drilling Program), 211–227.

Claypool, G.E., and Kvenvolden, K.A., 1983. Methane and other hydrocarbon gases in marine sediment. *Annu. Rev. Earth Planet. Sci.*, 11:299–327.

Deer, W.A., Howie, R.A., and Zussman, J., 1966. *An Introduction to the Rock-Forming Minerals:* London (Longman Group).

de Kaenel, E., and Villa, G., 1996. Oligocene–Miocene calcareous biostratigraphy and paleoecology from the Iberia Abyssal Plain. *In* Whitmarsh, R.B., Sawyer, D.S., Klaus, A., and Masson, D.G. (Eds.), *Proc. ODP, Sci. Results*, 149: College Station, TX (Ocean Drilling Program), 79–145.

Della Vadova, B., Pellis, G., Fouchet, J.-P., and Rehault, J.-P., 1984. Geothermal structure of the Tyrrhenian Sea. *Mar. Geol.*, 55:271–289.

Doglioni, C., 1991. A proposal of kinematic modelling for W-dipping subductions—possible applications to the Tyrrhenian-Apennines system. *Terra Nova*, 3:423–434.

Emeis, K.-C., Camerlenghi, A., McKenzie, J.A., Rio, D., and Sprovieri, R., 1991. The occurrence and significance of Pleistocene and Upper Pliocene sapropels in the Tyrrhenian Sea. *Mar. Geol.*, 100:155–182.

Emeis, K.-C., Robertson, A.H.F., Richter, C., et al., 1996. *Proc. ODP, Init. Repts.*, 160: College Station TX (Ocean Drilling Program).

Emerson, S., and Hedges, J.I., 1988. Processes controlling the organic carbon content of open ocean sediments. *Paleoceanography*, 3:621–634.

Espitalié, J., Laporte, J.L., Leplat, P., Madec, M., Marquis, F., Paulet, J., and Boutefeu, A., 1977. Méthode rapide de caractérisation des roches mères, de leur potentiel pétrolier et de leur degré d'évolution. *Rev. Inst. Fr. Pet.*, 32:23–42.

Hilgen, F.J., 1991. Extension of the astronomically calibrated (polarity) time scale to the Miocene/Pliocene boundary. *Earth Planet. Sci. Lett.*, 107:349–368.

Hsü, K.J., Montadert, L., Bernoulli, D., Cita, M.B., Erickson, A., Garrison, R.E., Kidd, R.B., Melières, F., Müller, C., and Wright, R., 1978. History of the Mediterranean salinity crisis. *In* Hsü, K.J., Montadert, L., et al., *Init. Repts. DSDP,* 42 (Pt. 1): Washington (U.S. Govt. Printing Office), 1053–1078.

Hutchison, I., Von Herzen, R.P., Louden, K.E., Sclater, J.G., and Jemsek, J., 1985. Heat flow in the Balearic and Tyrrhenian Basins, Western Mediterranean. *J. Geophys. Res.*, 90:685–701.

Jelinek, V., 1978. Statistical processing of magnetic susceptibility measured on groups of specimens. *Stud. Geophys. Geod.*, 22:50–62.

Kastens, K., and Mascle, J., 1990. The geological evolution of the Tyrrhenian Sea: an introduction to the scientific results of ODP Leg 107. *In* Kastens, K.A., Mascle, J., et al., *Proc. ODP, Sci. Results,* 107: College Station, TX (Ocean Drilling Program), 3–26.

Kastens, K.A., Mascle, J., Auroux, C., et al., 1987. *Proc. ODP, Init. Repts.*, 107: College Station, TX (Ocean Drilling Program).

Malinverno, A., and Ryan, B., 1986. Extension in the Tyrrhenian Sea and shortening in the Apennines as a result of arc migration driven by sinking of the lithosphere. *Tectonics,* 5:227–245.

Manheim, F.T., and Sayles, F.L., 1974. Composition and origin of interstitial waters of marine sediments based on deep sea drill cores. *In* Goldberg, E.D. (Ed.), *The Sea* (Vol. 5): New York (Wiley Interscience), 527–568.

McCoy, F.W., and Cornell, W., 1990. Volcaniclastic sediments in the Tyrrhenian Basin. *In* Kastens, K.A., Mascle, J., et al., *Proc. ODP, Sci. Results,* 107: College Station, TX (Ocean Drilling Program), 291–305.

Meyers, P.A., 1994. Preservation of elemental and isotopic source identification of sedimentary organic matter. *Chem. Geol.*, 144:289–302.

Müller, P.J., 1977. C/N ratios in Pacific deep sea sediments: effect of inorganic ammonium and organic nitrogen compounds sorbed by clays. *Geochim. Cosmochim. Acta,* 41:765–776.

Paterne, M., and Guichard, F., 1993. Triggering of volcanic pulses in the Campanian area, South Italy, by periodic deep magma influx. *J. Geophys. Res.*, 98:1861–1873.

Pierre, C., and Rouchy, J.M., 1990. Sedimentary and diagenetic evolution of Messinian evaporites in the Tyrrhenian Sea (ODP Leg 107, Sites 652, 653, and 654): petrographic, mineralogical, and stable isotope records. *In* Kastens, K.A., Mascle, J., et al., *Proc. ODP, Sci. Results,* 107: College Station, TX (Ocean Drilling Program), 187–210.

Prahl, F.G., and Wakeham, S.G., 1987. Calibration of unsaturation patterns in long-chain ketone compositions for paleotemperature assessment. *Nature,* 330:367–369.

Rehault, J.P., Mascle, J., and Boillot, G., 1984. Évolution géodinamique de la Méditerranée depuis l'Oligocene. *Mem. Soc. Geol. It.*, 27:85–96.

Rehault, J.P., Moussat, E., and Fabri, A., 1987. Structural evolution of the Tyrrhenian backarc basin. *Mar. Geol.*, 74:123–150.

Robertson, A., Hieke, W., Mascle, G., McCoy, F., McKenzie, J., Rehault, J., and Sartori, R., 1990. Summary and synthesis of late Miocene to Recent sedimentary and paleoceanographic evolution of the Tyrrhenian Sea, western Mediterranean: Leg 107 of the Ocean Drilling Program. *In* Kastens, K.A., Mascle, J., et al., *Proc. ODP, Sci. Results,* 107: College Station, TX (Ocean Drilling Program), 639–668.

Royden, L., Patacca, E., and Scandone, P., 1987. Segmentation and configuration of subducted lithosphere in Italy: an important control on thrust belt and foredeep-basin evolution. *Geology,* 15:714–717.

Savelli, C., 1988. Late Oligocene to Recent episodes of magmatism in and around the Tyrrhenian Sea: implications for the processes of opening in a young inter-arc basin of intra-orogenic (Mediterranean) type. *Tectonophysics,* 146:163–181.

Scandone, P., 1980. Origin of the Tyrrhenian Sea. *Mem. Soc. Geol. It.*, 98:27–34.

Shipboard Scientific Party, 1987. Site 652: lower Sardinian margin. *In* Kastens, K.A., Mascle, J., Auroux, C., et al., *Proc. ODP, Init. Repts.*, 107: College Station, TX (Ocean Drilling Program), 403–597.

————, 1992. Explanatory notes. *In* Collot, J.-Y., Greene, H.G., Stokking, L.B., et al., *Proc. ODP, Init. Repts.*, 134: College Station, TX (Ocean Drilling Program), 65–91.

————, 1995a. Site 914. *In* Larsen, H.C., Saunders, A.D., Clift, P.D., et al., *Proc. ODP, Init. Repts.*, 152: College Station, TX (Ocean Drilling Program), 53–71.

————, 1995b. Site 926. *In* Curry, W.B., Shackleton, N.J., Richter, C., et al., *Proc. ODP, Init. Repts.*, 154: College Station, TX (Ocean Drilling Program), 153–232.

————, 1996. Site 960. *In* Mascle, J., Lohmann, G.P., Clift, P.D., et al., *Proc. ODP, Init. Repts.*, 159: College Station, TX (Ocean Drilling Program), 151–215.

Sissingh, W., 1976. Aspects of Late Cenozoic evolution of the South Aegean ostracode fauna. *Palaeogeogr., Palaeoclimatol., Palaeoecol.,* 20:131–214.

Ms 161IR-104

NOTE: For all sites drilled, core-description forms ("barrel sheets") and core photographs can be found in Section 3, beginning on page 429. Smear-slide data can be found in Section 4, beginning on page 949. See Table of Contents for material contained on CD-ROM.

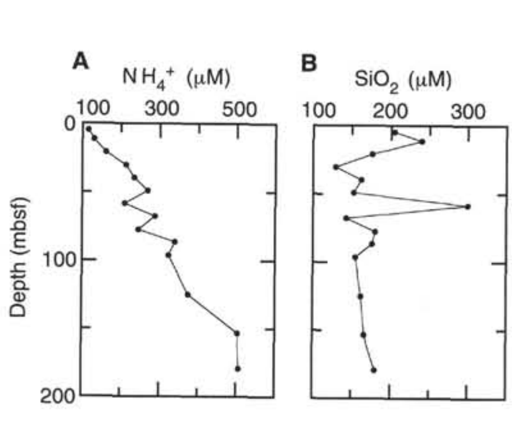

Figure 51. Concentration profiles of (**A**) ammonium and (**B**) silica in Hole 974B.

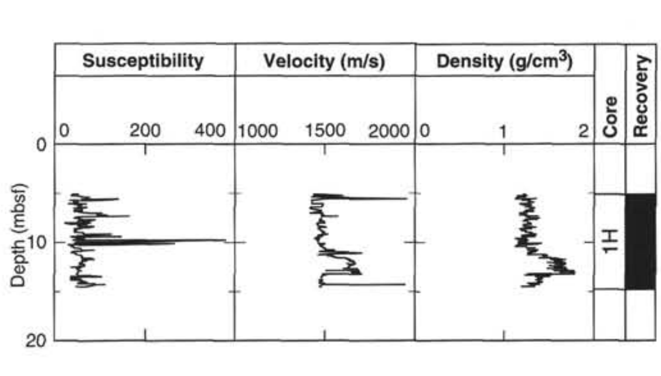

Figure 52. MST data (susceptibility, velocity, and density) for Hole 974A. Cored intervals and recovery amounts are shown on the right.

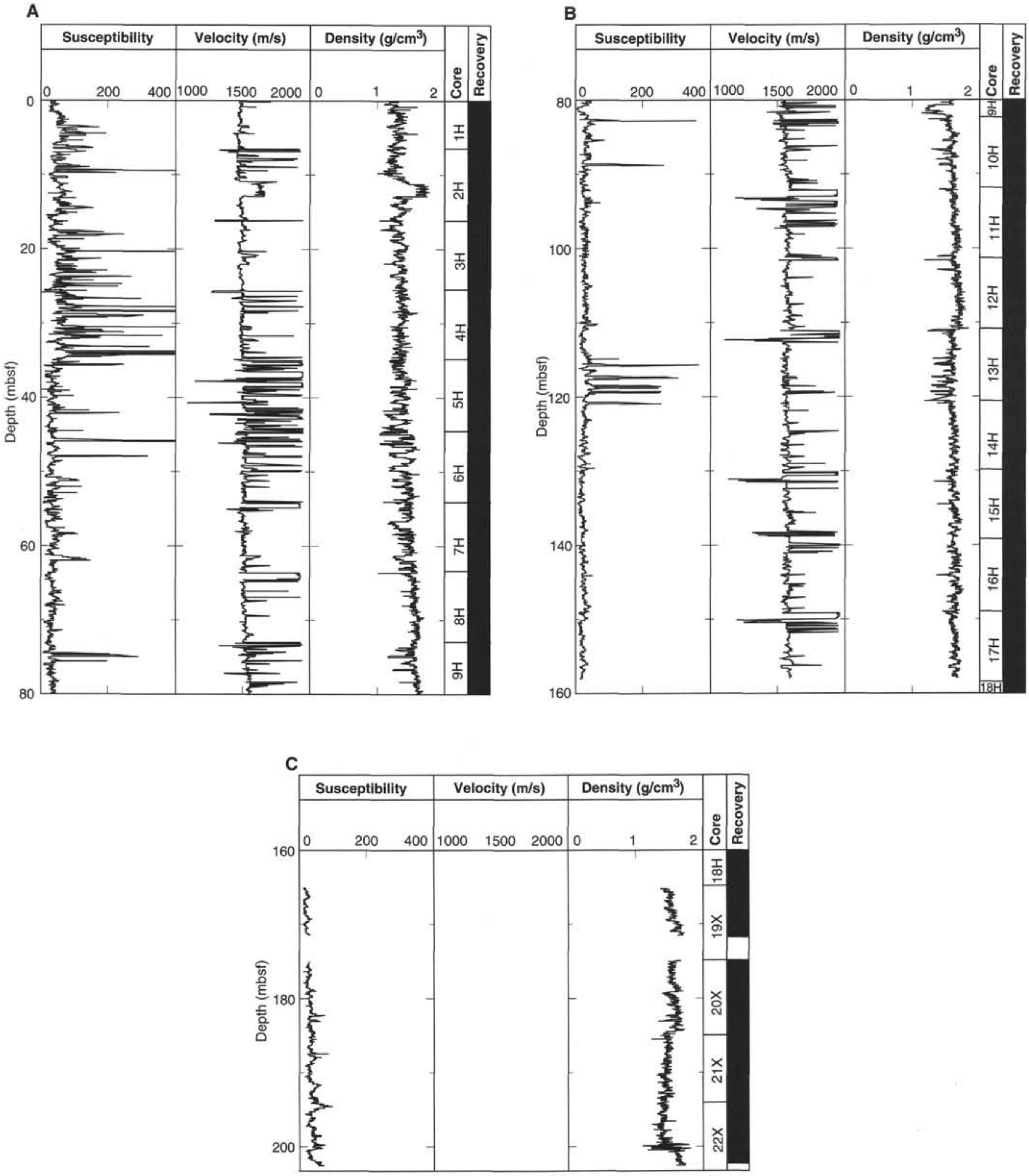

Figure 53. MST data (susceptibility, velocity, and density) for Hole 974B: (**A**) 0–80 mbsf, (**B**) 80–160 mbsf, (**C**) 160–205 mbsf. Cored intervals and recovery amounts are shown on the right.

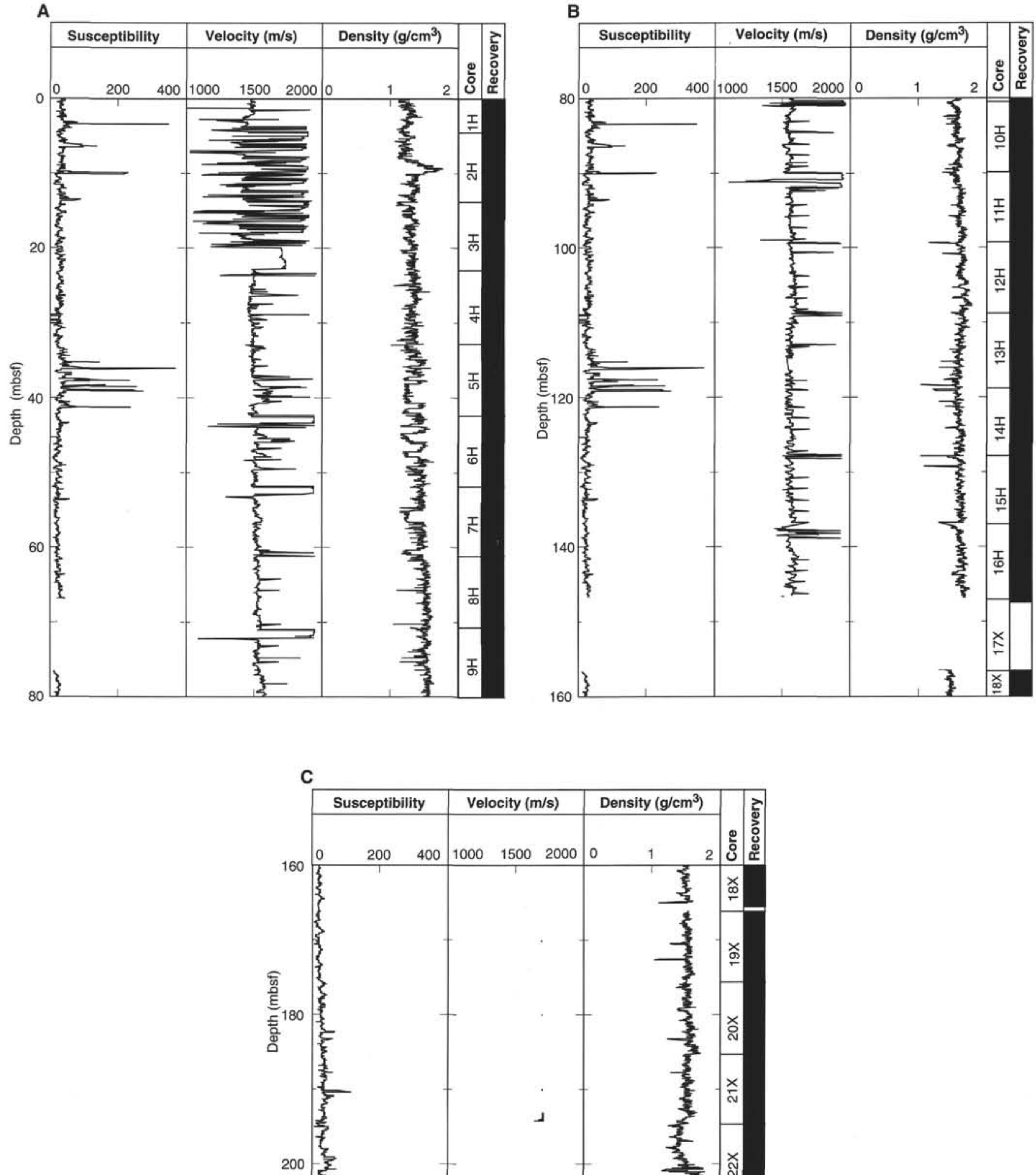

Figure 54. MST data (susceptibility, velocity, and density) for Hole 974C: (**A**) 0–80 mbsf, (**B**) 80–160 mbsf, (**C**) 160–205 mbsf. Cored intervals and recovery amounts are shown on the right.

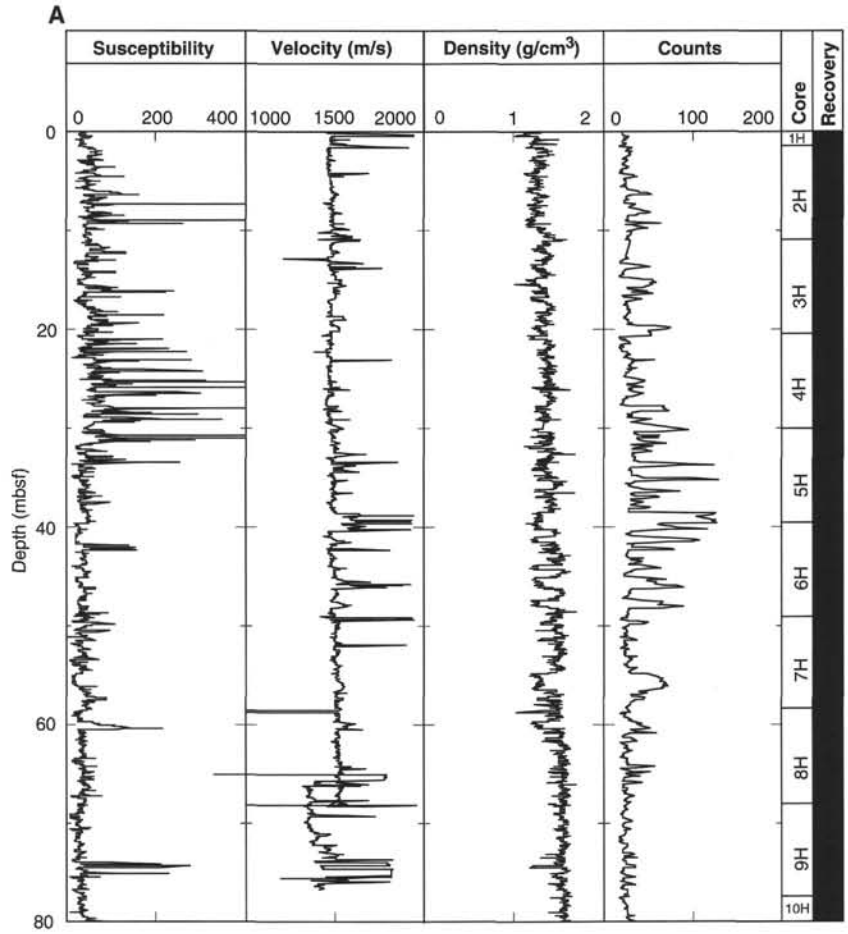

Figure 55. MST data (susceptibility, velocity, and density) for Hole 974D: (**A**) 0–80 mbsf, (**B**) 80–160 mbsf, (**C**) 160–165 mbsf. Cored intervals and recovery amounts are shown on the right.

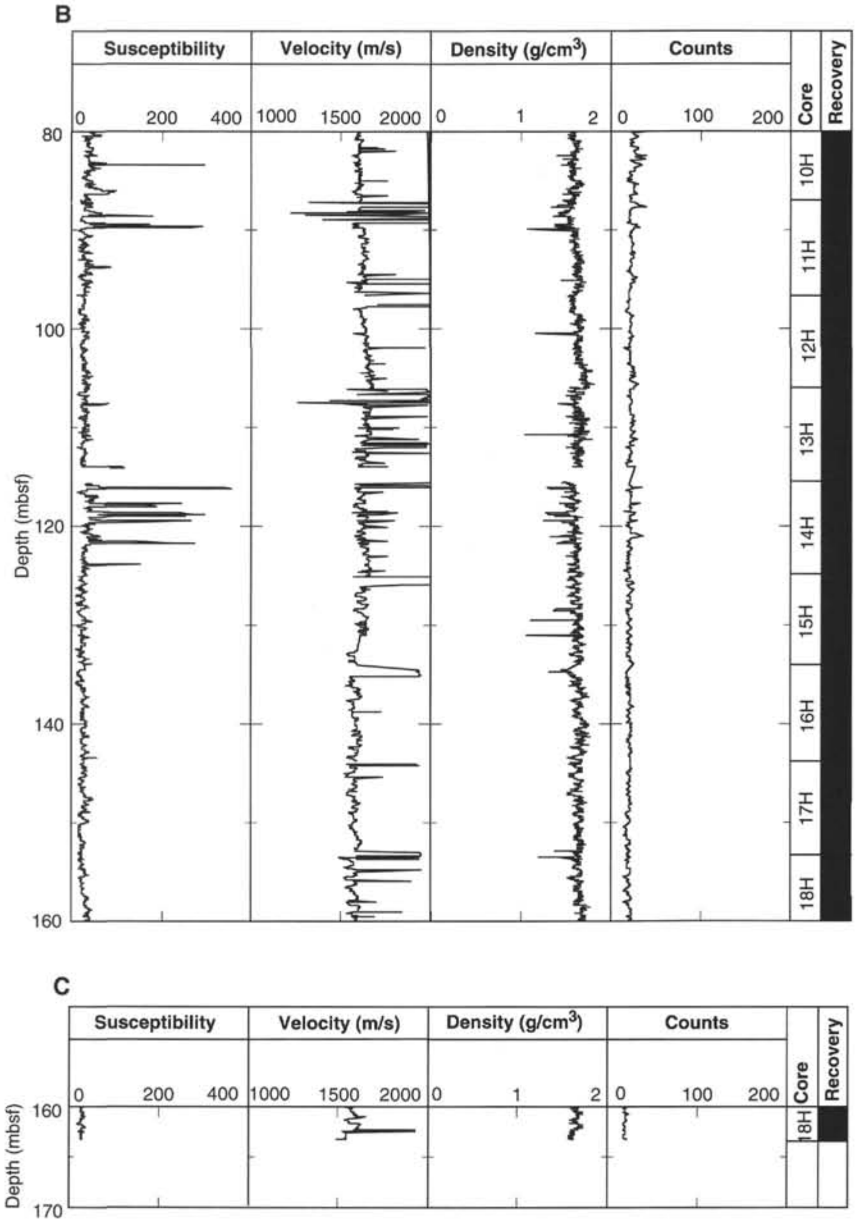

Figure 55 (continued).

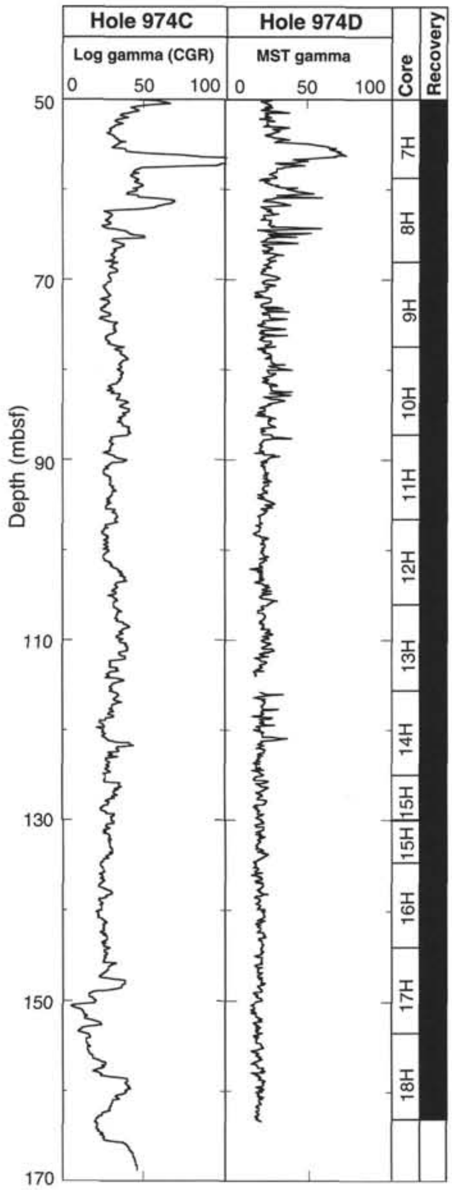

Figure 56. Comparison of Hole 974C downhole log CGR gamma-ray data with Hole 974D MST gamma-ray data.

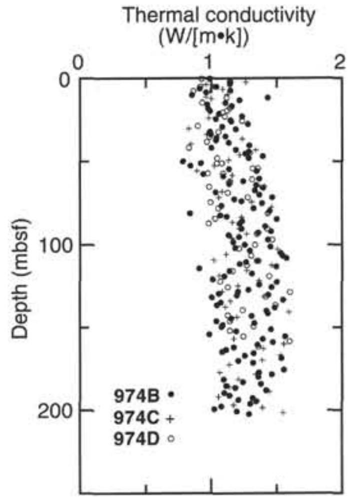

Figure 57. Thermal conductivity vs. depth for Holes 974B, 974C, and 974D. Solid circles = 974B, + = 974C, open circles = 974D.

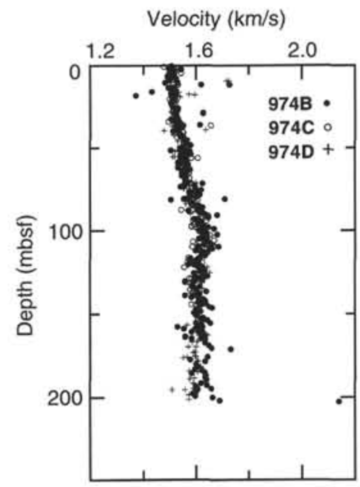

Figure 58. Seismic velocity vs. depth for Holes 974B, 974C, and 974D. Solid circles = 974B, open circles = 974C, + = 974D.

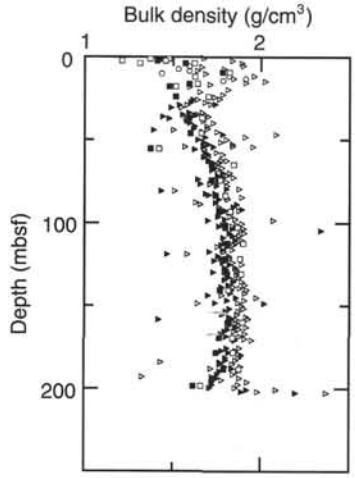

Figure 59. Bulk density (using both methods; see "Explanatory Notes" chapter, this volume) vs. depth for Holes 974A, 974B, and 974C. Open circles = 974A, method B; open triangles = 974B, method B; solid triangles = 974B, method C; open squares = 974C, method B; solid squares = 974C, method C.

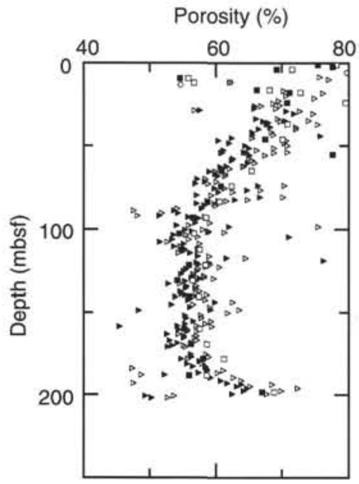

Figure 60. Porosity (using both methods; see "Explanatory Notes" chapter, this volume) vs. depth for Holes 974A, 974B, and 974C. Open circles = 974A, method B; open triangles = 974B, method B; solid triangles = 974B, method C; open squares = 974C, method B; solid squares = 974C, method C.

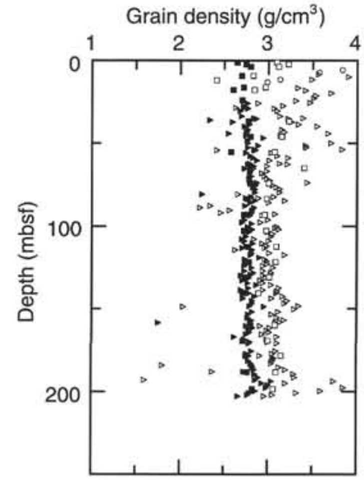

Figure 61. Grain density (using both methods; see "Explanatory Notes" chapter, this volume) vs. depth for Holes 974A, 974B, and 974C. Open circles = 974A, method B; open triangles = 974B, method B; solid triangles = 974B, method C; open squares = 974C, method B; solid squares = 974C, method C.

Table 20. Depths and equilibrium temperatures for the ADARA temperature tool runs at Hole 974B.

Depth (mbsf)	Temperature (°C)
23.3	15.969
51.8	20.091
80.3	23.917
108.8	27.790
137.3	30.704

Table 19. Logged depth intervals in Hole 974C for the three tool strings.

String	Run	Depth (mbsf)	Depth (mbrf)	Tools
Quad combo	Up	186.0–36.0	3662.6–3500.0	NGT/SDT/CNT-G/HLDT/DIT-E
FMS	Up 1	161.0–39.0	3625.0–3503.0	NGT/FMS/GPIT
	Up 2	160.0–39.0	3624.0–3503.0	NGT/FMS/GPIT
GLT	Up 1	186.0–36.0	3650.0–3500.0	GSTA/ACTC/CNTG/NGTC/TCCB
	Up 2	186.0–119.0	3650.0–3583.0	GSTA/ACTC/CNTG/NGTC/TCCB

Note: mbsf = meters below seafloor, mbsf = meters below rig floor.

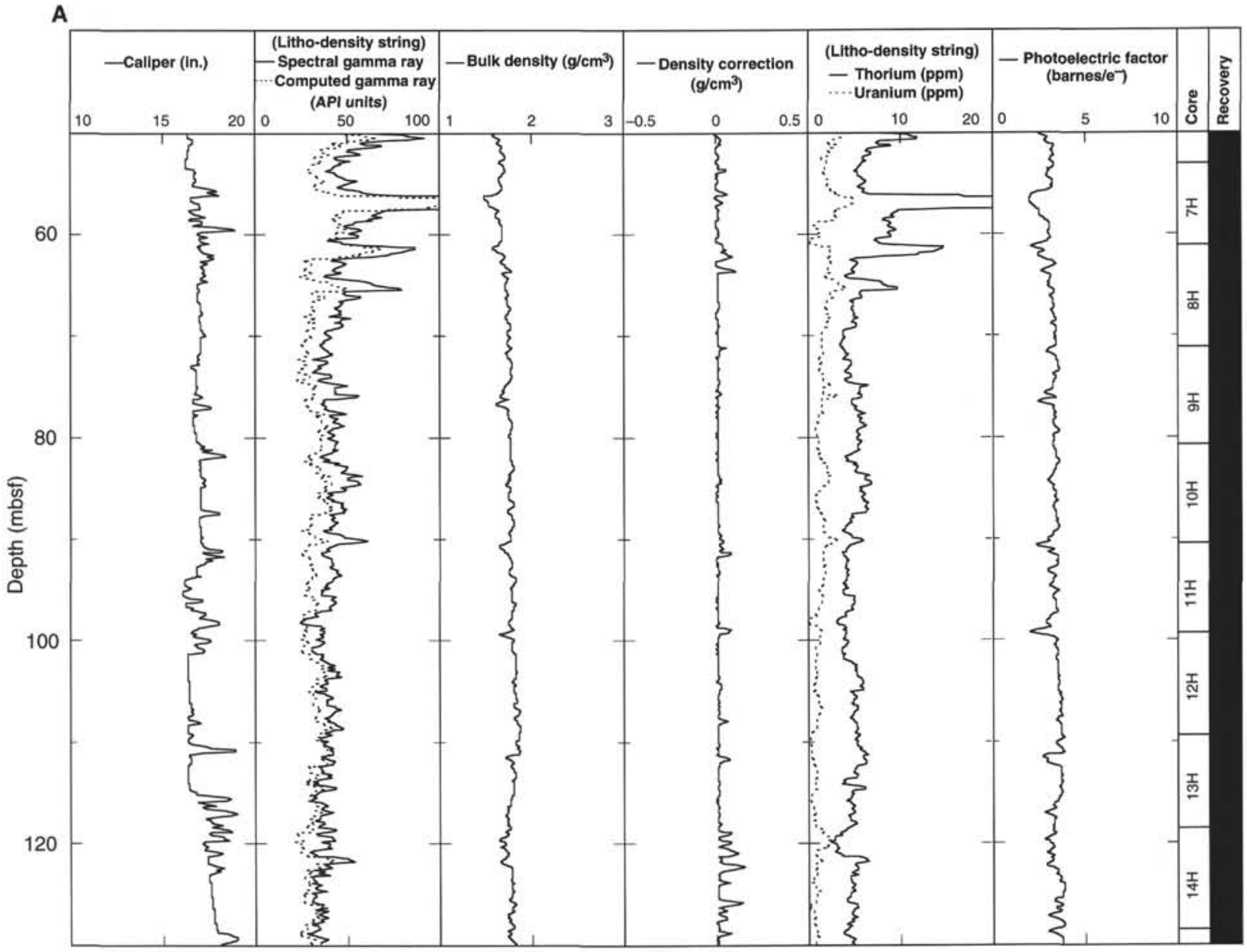

Figure 62. Quad combo tool results (**A**: 50–130 mbsf; **B**: 130–200 mbsf) and FMS (main log) calipers (**C**: 50–130 mbsf; **D**: 130–200 mbsf) for Hole 974C.

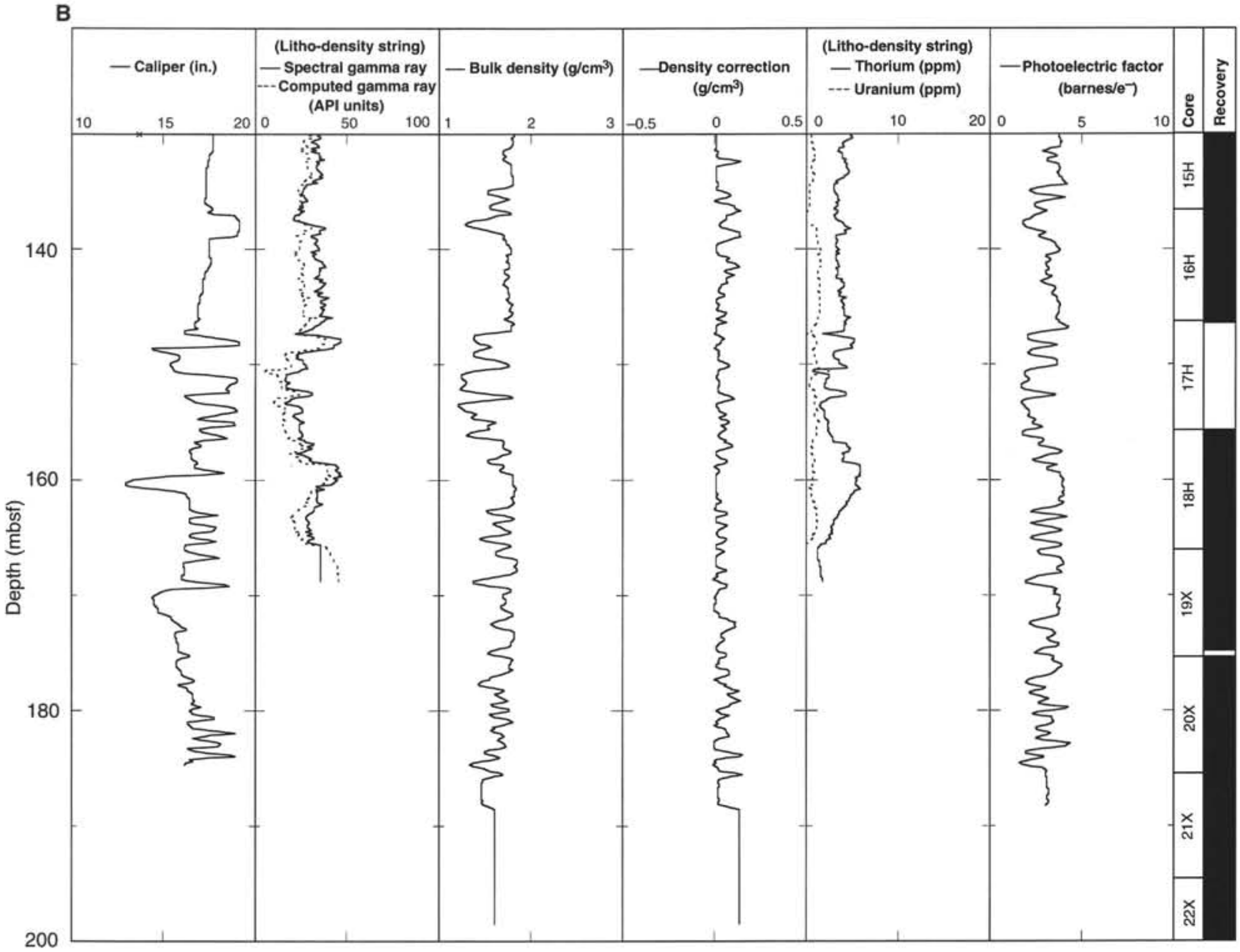

Figure 62 (continued).

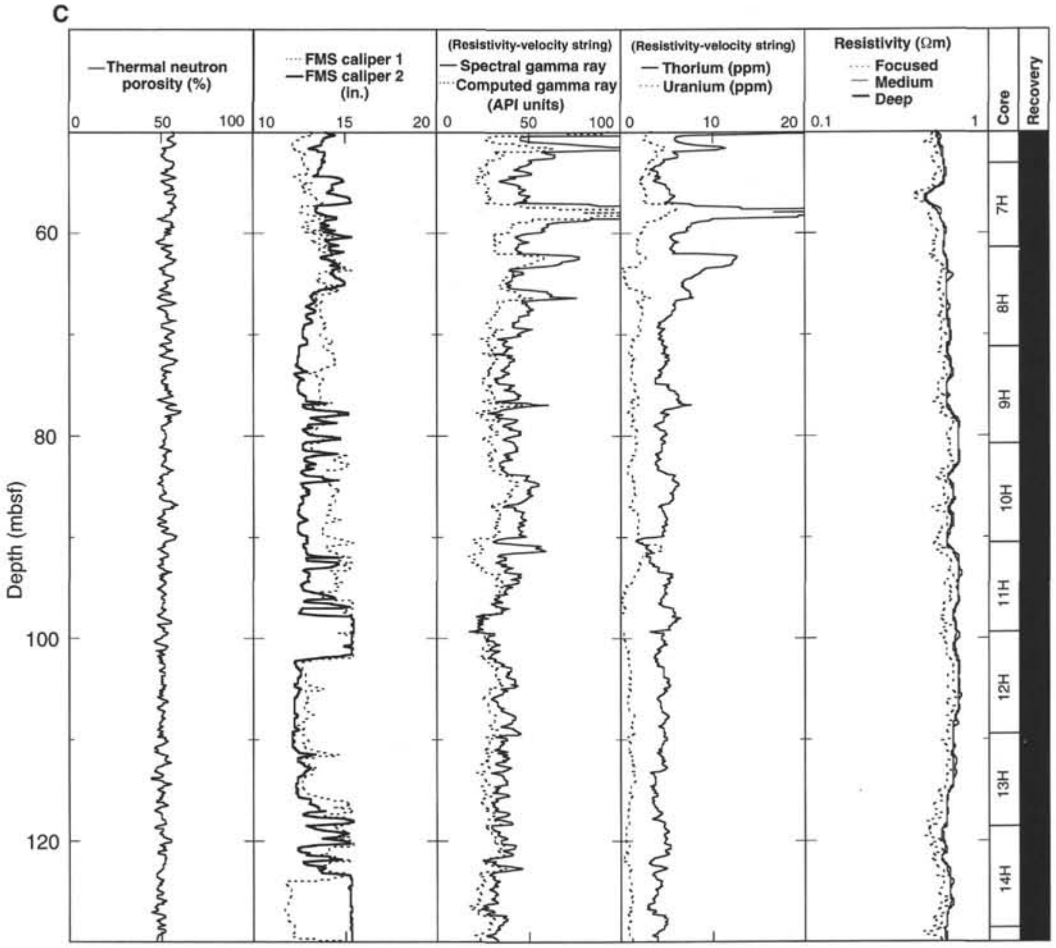

Figure 62 (continued).

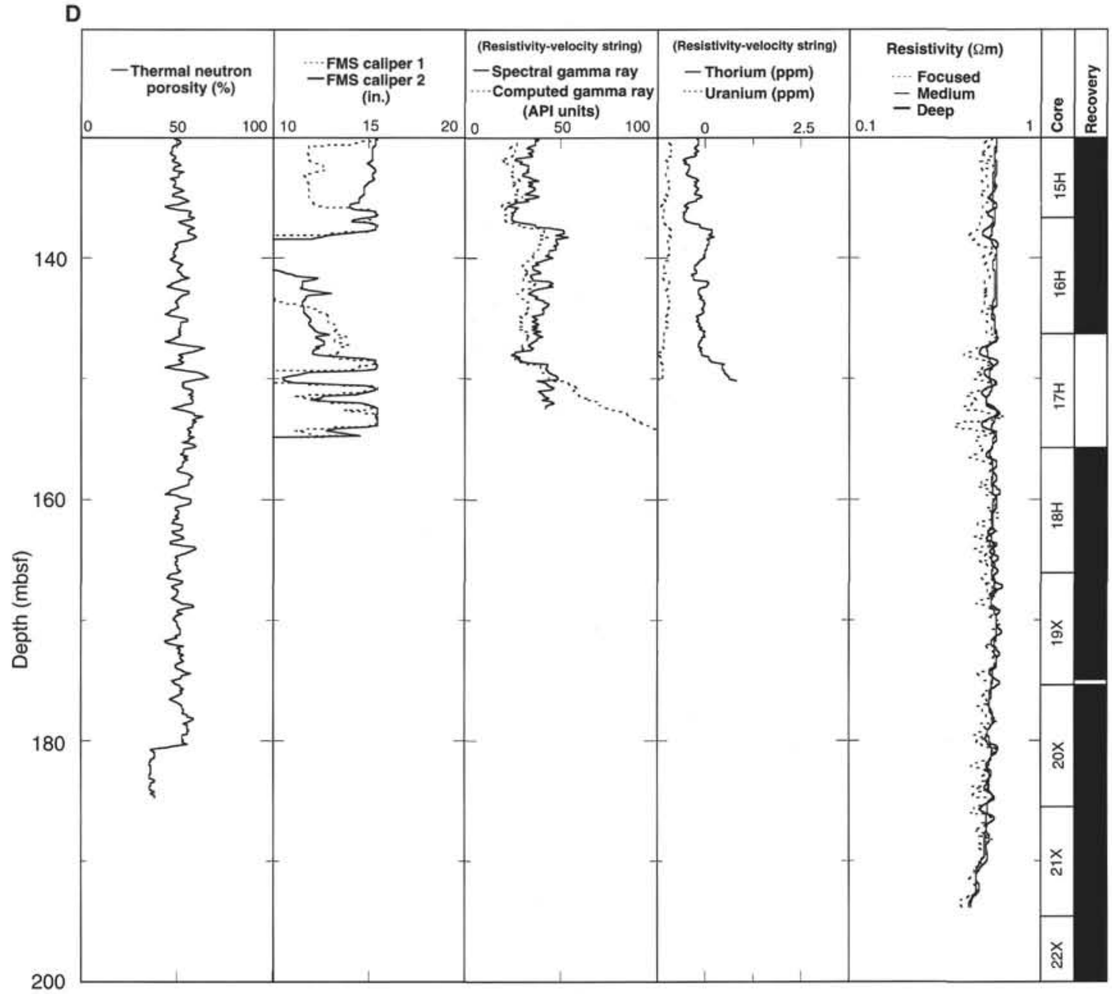

Figure 62 (continued).

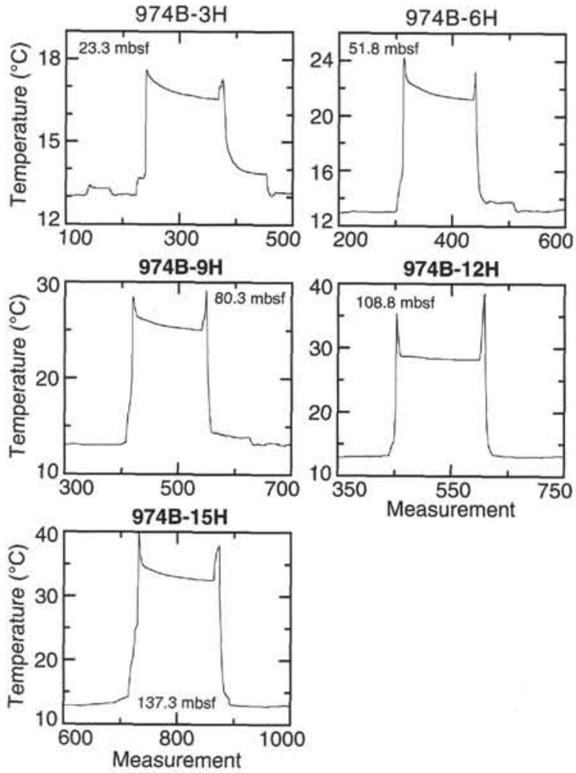

Figure 63. Temperature vs. time for the individual ADARA temperature tool runs at Hole 974B.

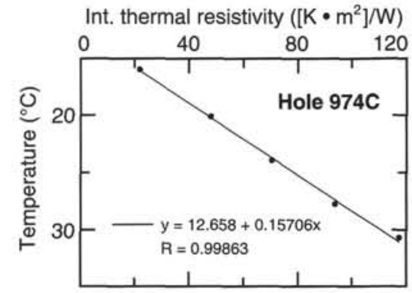

Figure 64. Temperature vs. integrated thermal resistivity for Hole 974B. The best-fitting linear regression to the data is shown by the straight line.

SHORE-BASED LOG PROCESSING

Hole 974C

Bottom felt: 3464.1 mbrf (used for depth shift to seafloor)
Total penetration: 204.5 mbsf
Total core recovered: 199.8 m (97.7%)

Logging Runs

Logging String 1: DIT/SDT/HLDT/CNTG/NGT
Logging String 2: FMS/GPIT/NGT (2 passes)
Logging String 3: ACT/GST/NGT
Wireline heave compensator was used to counter ship heave.

Bottom-Hole Assembly

The following bottom-hole assembly depths are as they appear on the logs after differential depth shift (see "Depth shift" section) and depth shift to the seafloor. As such, there might be a discrepancy with the original depths given by the drillers onboard. Possible reasons for depth discrepancies are ship heave, use of wireline heave compensator, and drill string and/or wireline stretch.

DIT/SDT/HLDT/CNTG/NGT: Bottom-hole assembly at ~35.5 mbsf.

ACT/GST/NGT: Bottom-hole assembly at ~35.5 mbsf.

FMS/GPIT/NGT: Bottom-hole assembly at ~35.5 mbsf.

Processing

Depth shift: Reference run for depth shift: DIT/SDT/HLDT/CNTG/NGT main pass. All original logs have been interactively depth shifted with reference to NGT from DIT/SDT/HLDT/CNTG/NGT main pass and to the sea floor (–3464.1 m).

Gamma-ray processing: NGT data have been processed to correct for borehole size and type of drilling fluid.

Acoustic data processing: The array sonic tool was operated in two modes: linear array mode, with the 8-receivers providing full waveform analysis (compressional and shear) and standard depth-derived borehole compensated mode, including long-spacing (8-10-10-12 ft) and short-spacing (3-5-5-7 ft) logs. The long-spacing sonic logs have been processed to eliminate some of the noise and cycle skipping experienced during the recording.

Geochemical processing: For detailed explanation of the processing, please refer to the "Explanatory Notes," this volume, or to the geochem.doc file on the CD-ROM found in the back pocket, this volume. The elemental yields recorded by the GST tool represent the relative contribution of only some of the rock-forming elements (iron, calcium, chlorine, silica, sulfur, hydrogen, gadolinium, and titanium—the last two elements computed during geochemical processing) to the total spectrum. Because other rock-forming elements are present in the formation (such as aluminum, potassium, etc.), caution is recommended in using the yields to infer lithologic changes. Instead, ratios (see acronyms.doc on the CD-ROM, back pocket, this volume) are more appropriate to determine changes in the macroscopic properties of the formation. A list of oxide factors used in geochemical processing includes the following:

SiO_2 = 2.139
$CaCO_3$ = 2.497
FeO* = 1.358
TiO_2 = 1.668
K_2O = 1.205
Al_2O_3 = 1.889

FeO* = computed using an oxide factor that assumes a 50:50 combination of Fe_2O_3 and FeO factors. The results of the processing are presented along with the calcium carbonate measurements performed on board.

Quality Control

Data recorded through bottom-hole assembly, such as the gamma ray and neutron data above 35.5 mbsf, should be used qualitatively only because of the attenuation on the incoming signal. Invalid gamma ray spikes were recorded at 24–28 mbsf by the DIT/SDT/HLDT/CNTG/NGT string.

Hole diameter was recorded by the hydraulic caliper on the HLDT tool (CALI) and on the FMS string (C1 and C2).

FACT = quality-control curve in geochemical processing. Accuracy of the estimates is inversely proportional to the magnitude of the curve.

Note: Details of standard shore-based processing procedures are found in the "Explanatory Notes" chapter, this volume. For further information about the logs, please contact:

Cristina Broglia
Phone: 914-365-8343
Fax: 914-365-3182
E-mail: chris@ldeo.columbia.edu

Elizabeth Pratson
Phone: 914-365-8313
Fax: 914-365-3182
E-mail: beth@ldeo.columbia.edu

Hole 974C: Natural Gamma Ray-Resistivity-Sonic Logging Data

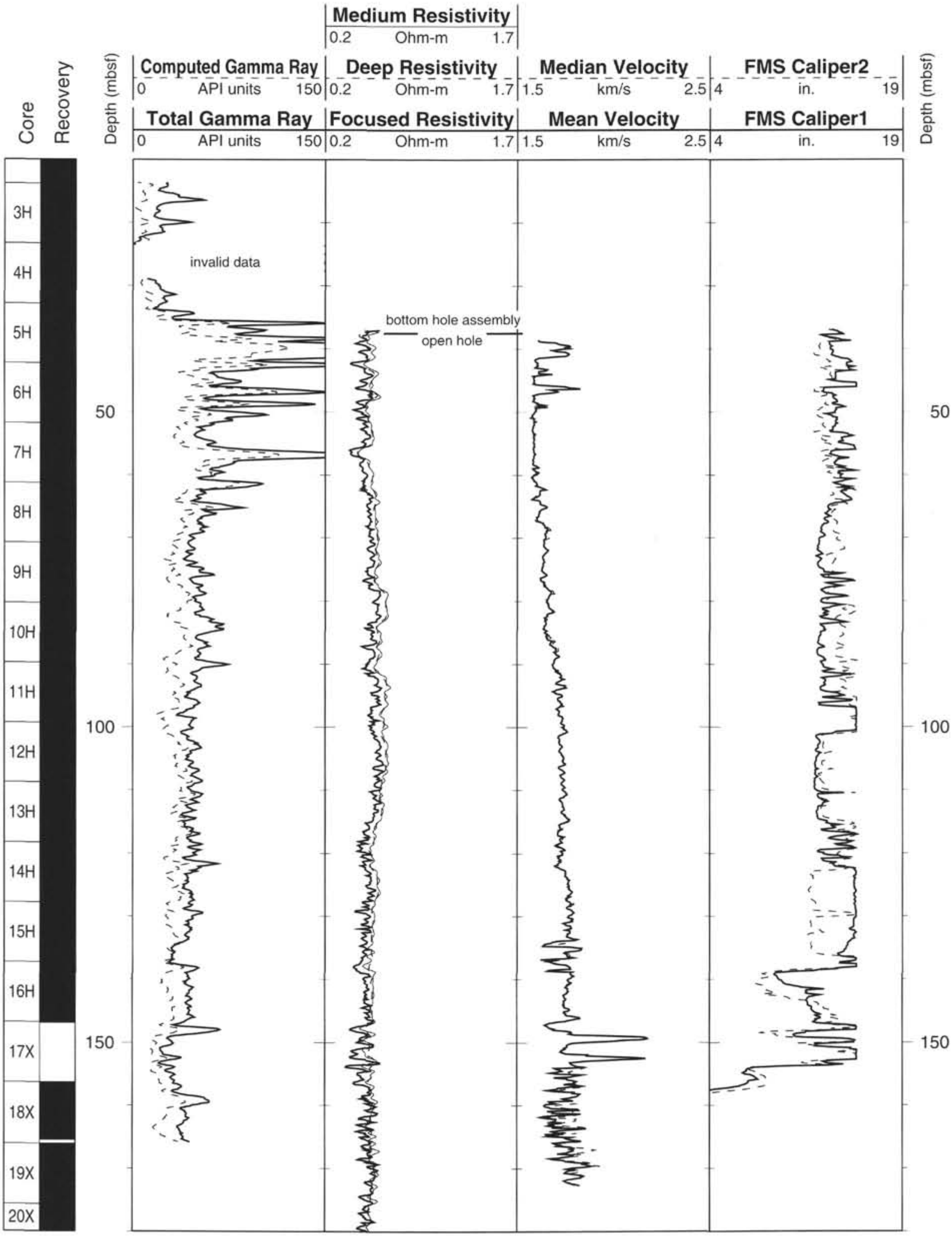

Hole 974C: Natural Gamma Ray-Resistivity-Sonic Logging Data (cont.)

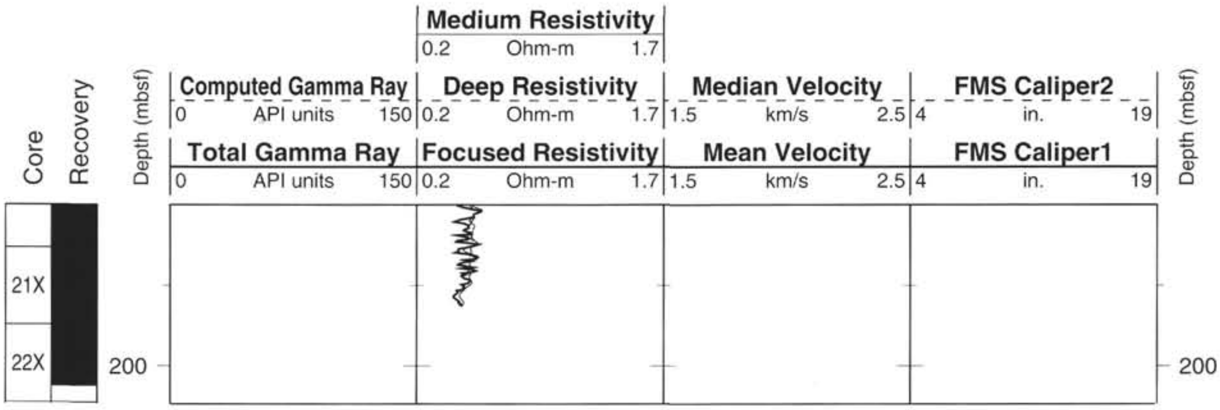

Hole 974C: Natural Gamma Ray-Density-Porosity Logging Data

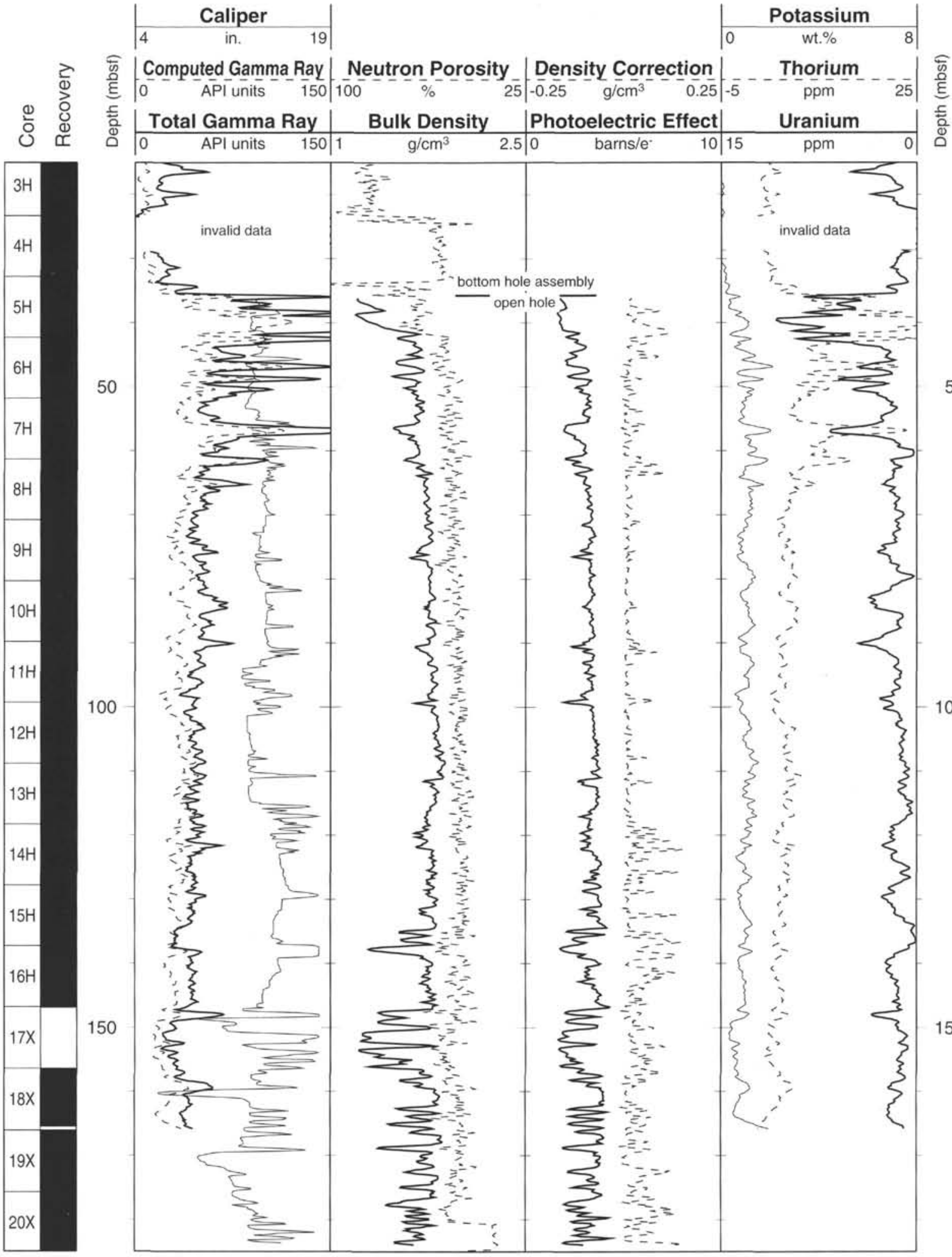

Hole 974C: Natural Gamma Ray Logging Data

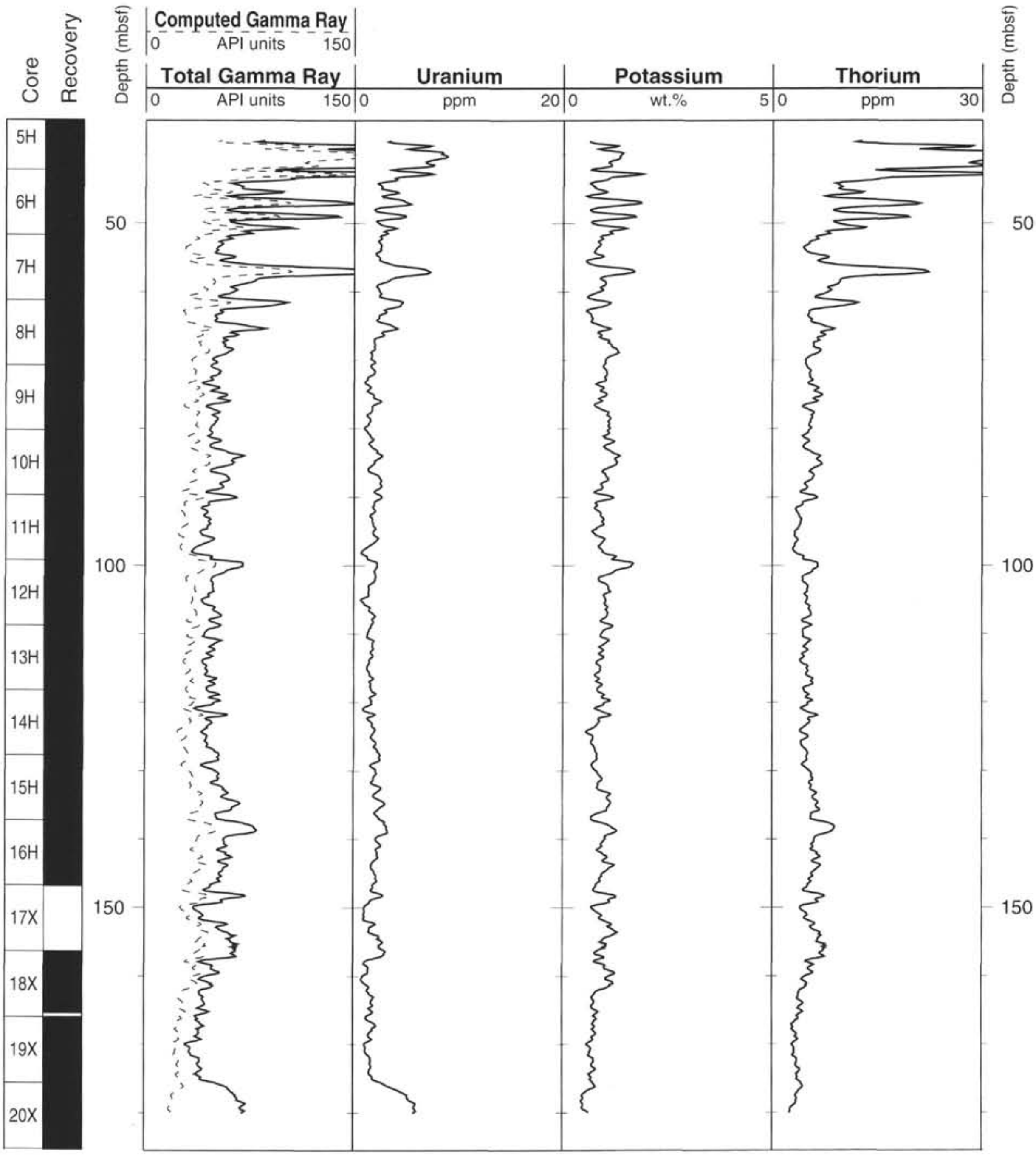

Hole 974C: Geochemical Logging Data